

# **Integration of a Self-Powered Sensor and Electronics to Produce a Battery-Free, Wireless, Water Leak Detection Device**

by

Levi Nathaniel Johnston

A thesis

presented to the University of Waterloo

in fulfillment of the

thesis requirement for the degree of

Master of Applied Science

in

Mechanical and Mechatronics Engineering

Waterloo, Ontario, Canada, 2022

© Levi Nathaniel Johnston 2022

## **Author's Declaration**

This thesis consists of material all of which I authored or co-authored: see Statement of Contributions included in the thesis. This is a true copy of the thesis, including any required final revisions, as accepted by my examiners.

I understand that my thesis may be made electronically available to the public.

## **Statement of Contributions**

Levi Johnston is the sole author of all Chapters, under the supervision of Dr. Norman Zhou, with the exception of Figures 19 and 22 (Chapter 4), which were prepared by Ming Xiao.

### **Research presented in Chapters 3, 4 and 5**

Testing done in Chapters 3, 4 and 5 was done by Levi Johnston along with input and assistance from fellow students including Ming Xiao, Jiayun Feng, Jarren Teo, Xiaoye Zhao, Martins Akhouhale, Kamalpreet Kaur, Mohammad Rouhi, and Simran Chathanat. Test selection and design, data processing and analysis, and preparation of charts and figures are the work of Levi Johnston.

### **Designs in Appendix B**

The PCBs in Appendix B were designed and assembled by Nimesh Kotak and Martins Akhouhale. Levi Johnston prepared the figures and explanations for reference in this thesis with input from Nimesh Kotak.

## **Abstract**

Water damage accounts for 73% by dollars lost in commercial real estate claims [1]. Water leak detectors are a key solution to the problem but suffer from numerous drawbacks, namely high costs, lack of scalability, and over-reliance on batteries. This severely limits their usability in large-scale multi-residential and commercial applications. Small, self-powered sensing devices that operate from water exist in research, but examples of market ready technology that relies on alternative standalone power-sources are scarce. Here, the objective is to create a battery-free water leak detector using a recently published water-powered sensor.

The sensor consists of two electrode layers, which, when exposed to water, produces usable power output. This power can be collected and used to operate a Bluetooth device for wireless data transmission. The work here involves integrating the sensor materials into a custom enclosure design so that they can be used as a typical water leak sensor would. Multiple design iterations were tested to produce the first prototype design. This involved developing the contact methods from a wire to the electrodes of the sensor, designing methods for the water to reach the electrodes, features to keep the packaging closed, and overall device layout and wire routing. The sensor prototype performance at this stage was significantly worse than previously reported sensor performance without any mechanical enclosure. Improvements suggested included better mating force between the sensor enclosure lid and base, easier assembly, and manufacturing quality checks to name a few.

The identified design flaws were improved upon, and a second major design iteration was produced, this time by injection molding. The sensor performance was comparable to the unpackaged measurements. Notable performance achievements include a yield rate of 100% for a sample size of 24, and furthermore, all devices activating in less than 1 minute. The results of testing with the final design iteration are promising enough to conclude that the sensor materials employed in the water leak sensor design are feasible to use for water leak detection applications.

## **Acknowledgements**

I would like to thank my supervisor Prof. Norman Zhou for support and guidance through all aspects of this project, and for the opportunity to join their research team.

The water leak detector project as whole has received contributions from many colleagues along the way, for which I am incredibly grateful.

First, I would like to Prof. George Shaker and fellow student Nimesh Kotak for their electrical engineering expertise, contributing the PCBs designs to the sensor, as well as guidance on electrical and wireless testing procedures. Without their design contributions, this device would not be possible.

I would also like to thank fellow students Ming Xiao, Jarren Teo, and Jiayun Feng who offered their expertise in materials engineering to guide my own design process. I would like to thank them again, as well as fellow students Martins Akhoukhale, Xiaoye Zhao, Kamalpreet Kaur, Mohammad Rouhi and Simran Chathanat for help with testing and materials preparation.

Special thanks to John Hanna for help with device manufacturing, and all additional students who helped develop the mechanical and electrical aspects of the water leak detection system.

I would like to thank Kushant Patel, Oliver Witham, along with all other fellow students who contributed to the leak detector system's software and firmware components.

# Table of Contents

<b>List of Figures</b> .....	<b>x</b>
<b>List of Tables</b> .....	<b>xiv</b>
<b>List of Abbreviations</b> .....	<b>xv</b>
<b>Chapter 1. Introduction</b> .....	<b>1</b>
1.1. Background.....	1
1.2. Objective.....	3
1.3. Thesis Outline .....	3
<b>Chapter 2. Literature Review</b> .....	<b>4</b>
2.1. Introduction to Chapter 2.....	4
2.2. Water Leak Detection Technology .....	4
2.2.1. Types of Water Leak Detection Technology .....	4
2.2.2. Water Leak Detectors for Residences and Commercial Spaces .....	5
2.2.3. Issues with Current Water Leak Detection Systems.....	5
2.2.4. IoT for Water Leak Detection.....	7
2.3. Battery-Free Sensor Technologies.....	7
2.3.1. Energy Harvesting Devices.....	7
2.3.2. Radio Frequency ID and Near-Field Communication Tags .....	9
2.3.3. Moisture-Based and Water-Based Generators and Sources .....	10
2.4. Background on Prior Sensor Materials and Electronics Work.....	12
2.4.1. Sensor Materials.....	12
2.4.1.1. Carbon Electrode .....	12
2.4.1.2. Magnesium Electrode .....	12
2.4.2. Electronics.....	13
2.5. Summary of Chapter 2.....	13
<b>Chapter 3. Methods and Design Considerations</b> .....	<b>14</b>
3.1. Introduction to Chapter 3.....	14
3.1.1. Comments on Selection of Test Duration.....	14
3.2. Electrical Performance Testing.....	14
3.2.1. Electrical Performance Testing Equipment .....	15

3.2.2.	Open-Circuit Voltage (OCV) Test Procedure.....	16
3.2.3.	Short-Circuit Current (SCC) Test Procedure.....	16
3.2.4.	Load Test Procedure.....	17
3.3.	Water Leak Detector Performance Metrics.....	18
3.3.1.	Beacon Activation Time.....	18
3.3.2.	Yield Rate Testing.....	19
3.3.3.	Multiple Use Testing.....	20
3.3.4.	Drop Testing.....	20
3.4.	Unpackaged Sensor Electrical Performance.....	20
3.4.1.	Unpackaged Sensor Electrical Test Setup.....	21
3.4.2.	OCV Performance Baseline.....	21
3.4.3.	SCC Performance Baseline.....	22
3.4.4.	Constant Current Load Test Performance Baseline.....	23
3.4.5.	Comments on Evaporation.....	24
3.5.	Packaging Design Considerations.....	25
3.5.1.	Pressure Sensitivity.....	25
3.5.2.	Carbon Electrode Expansion.....	25
3.5.3.	Probe Insertion Depth Versus Electrical Performance.....	25
3.5.4.	Pre-Cracking of the Carbon Electrode.....	26
3.6.	Summary of Chapter 3.....	27
<b>Chapter 4.</b>	<b>Water Leak Sensor Prototype Design.....</b>	<b>28</b>
4.1.	Introduction to Chapter 4.....	28
4.1.1.	Considerations for 3D Printing.....	28
4.2.	Electrical Contact Prototyping.....	29
4.2.1.	Probe Tip Imitation Design with CNFs.....	29
4.2.2.	Copper Tape Contact with Mg.....	30
4.2.3.	Spring Contact with Magnesium.....	32
4.2.4.	Change to Graphite and Enclosure Resizing.....	34
4.2.5.	Conductive Washer Contact.....	35
4.2.6.	Solder Terminal Lug Contact.....	37
4.2.7.	Summary of Contact Performance Improvements.....	39
4.3.	Water Absorption Methods.....	39

4.3.1.	Water Channels.....	39
4.3.2.	Wicking Tails.....	40
4.4.	Complete Sensor Unit Design .....	43
4.4.1.	Sensor Enclosure.....	43
4.4.2.	Electronics Enclosure.....	44
4.4.3.	Complete Leak Detector .....	45
4.5.	3D Printed Version Evaluation.....	47
4.5.1.	First Complete System Test .....	47
4.5.2.	Yield Rate and Multiple Use Testing.....	47
4.5.3.	Filter Paper Barrier Modification.....	49
4.5.4.	Drop Testing .....	50
4.5.5.	Assembly Steps Evaluation.....	53
4.5.6.	3D Printing Quality.....	54
4.6.	Discussion of Design and Manufacturing Flaws .....	56
4.6.1.	Magnesium Spring Contact Deflection vs Package Closing Force .....	56
4.6.2.	Graphite Electrical Conductivity and Water Saturation Level .....	56
4.6.3.	Packaging Form and Assembly Ease.....	57
4.6.4.	Variable Beacon Activation Time and Low Yield Rates.....	58
4.7.	Summary of Chapter 4.....	58
<b>Chapter 5.</b>	<b>Water Leak Sensor Production Design.....</b>	<b>59</b>
5.1.	Introduction to Chapter 5.....	59
5.2.	Design and Manufacturing Changes from 3D Printed Version.....	59
5.2.1.	Sensor Packaging Screws .....	59
5.2.2.	Design for Injection Molding.....	60
5.2.3.	Filter Paper Shape Modification .....	60
5.2.4.	Graphite and Magnesium Chamber Diameter .....	61
5.2.5.	Magnesium Disc Thickness Check.....	61
5.2.6.	Resistance Check .....	61
5.3.	Leak Sensor Packing Evaluation .....	62
5.3.1.	Visual and Dimensional Inspection .....	62
5.3.2.	Electrical Testing .....	63
5.3.3.	Beacon Activation Time and Yield Rate Testing .....	65



5.4. Summary of Chapter 5.....	67
<b>Chapter 6. Conclusions.....</b>	<b>68</b>
6.1. Conclusions.....	68
6.2. Recommendations and Future Work .....	69
<b>References.....</b>	<b>72</b>
<b>Appendices.....</b>	<b>79</b>
<b>Appendix A. Sensor Material Preparation .....</b>	<b>79</b>
A.1. Carbon Electrode .....	79
A.1.1. CNF and Graphite Electrode Pressing Mould .....	79
A.1.2. Mirco Tester as Compression Machine .....	80
A.2. Magnesium Electrode .....	80
A.2.1. Magnesium Plate Preparation .....	80
A.2.2. Magnesium Disc Preparation.....	81
A.2.3. Sensor Assembly and Usage.....	82
<b>Appendix B. Electrical Details .....</b>	<b>83</b>
B.1. System Overview.....	83
B.2. Sensor Materials: Basic Electrical Model.....	84
B.3. EH Board .....	87
B.4. BLE Board .....	87
<b>Appendix C. Injection Moulding Design Changes .....</b>	<b>89</b>
C.1. Overview of Design Guidelines and Requirements.....	89
C.2. List of Injection Molding Changes .....	89
<b>Appendix D. Wireless Leak Detection System Architecture .....</b>	<b>91</b>
D.1. Overview of System Architecture .....	91

## List of Figures

Figure 1: A) Components of a commercially available water leak detector, B) simplified design for the proposed “self-powered” water leak detector. The packaging (shaded) is the focus of this thesis. ....	1
Figure 2: Sensor materials in electrical test setup, graphite design shown.....	12
Figure 3: Electrodes produced for sensor use. A) Graphite electrode, B) magnesium electrode. ....	13
Figure 4: A) DMM used in electrical performance testing, image taken while measuring DC current, B) SMU used in electrical performance testing, C) sensor packaging from Chapter 5 connected to test leads, D) schematic of testing setup for collecting and logging DMM and SMU data.....	15
Figure 5: OCV test setup, sensor in packaging, electrical schematic shown left .....	16
Figure 6: SCC test setup, sensor in packaging, electrical schematic shown left .....	17
Figure 7: Load testing test setup, sensor in packaging, electrical schematic shown left for constant current and constant voltage test.....	18
Figure 8: Beacon activation time test setup including BLE scanning application on a mobile phone. A) Example schematic, B) actual test with sensor output voltage measured, stopwatch timer not shown .....	19
Figure 9: Unpackaged sensor materials test setup .....	21
Figure 10: Unpackaged sensor materials performance in OCV test condition. Window for computing average OCV shown in red. Data is time-shifted such that the sensor response occurs at $t = 0$ s, where the sensor response event is the first point that $V_{OC}$ exceeds 0.5 V .....	22
Figure 11: Unpackaged sensor materials performance in SCC test condition. Window for computing average SCC shown in red. Data is time-shifted such that the sensor response occurs at $t = 0$ s, where the sensor response event is the first point that SCC exceeds 1 mA.....	23
Figure 12: Unpackaged sensor materials performance in CC Load test condition. Window for computing average $V_{CC}$ and $P_{CC}$ shown in red. Data is time-shifted such that the application of the load occurs at $t = 0$ s. ....	24
Figure 13: Pressure on carbon electrode may decrease performance .....	25
Figure 14: Probe tip insertion depth sensitivity .....	26
Figure 15: Cracked graphite electrodes A) due to test probe, B) due to handling before assembly into packaging, C) larger surface area probe may aggravate cracking issue in packaging design. ....	27
Figure 16: FDM printer producing a part, image from [65] .....	28
Figure 17: Probe-tip imitation design. A) CAD model left with components labeled right, B) cross section with dimensions in millimetres, C) lid raised to show CNF electrode, D) Experimental setup to test electrical performance.....	30
Figure 18: Copper tape contact design. A) CAD model with labeled components, B) 3D printed, C) cross section with dimensions.....	31

Figure 19: Unstable OCV performance for copper tape contact .....	31
Figure 20: Spring contact for magnesium, dimensions in millimetres .....	32
Figure 21: Spring clip design. A) Components of sensor packaging labeled, B) cross section with spring contact distance to magnesium disc and annular snap, C) 3D Printed version showing disassembled lid and packaging with spring contact, D) assembled packaging, with CNF side upwards showing water-intake features.....	33
Figure 22: Testing packaging design, probe contact for CNFs, spring contact for Mg. A) OCV test results, B) SCC test results.....	34
Figure 23: SCC current test for graphite replacement. Average peak current was 6.53 mA and average across 5 mins was 3.54 mA. ....	35
Figure 24: Copper nickel-plated washer contact in modified enclosure design. A) Complete enclosure, B) enclosure with some components hidden to show washer contact location, C) washer dimensions, washer manufactured by Switchcraft [66], D) cross section view with washer contact and sensor materials, E) detail view of solder joint location below graphite electrode, F) graphite electrode cracking above solder joint. ....	36
Figure 25: SCC test for washer contact design. Peak current was 12.1 mA, and the 5-minute average was 4.0 mA.....	36
Figure 26: Solder terminal lug contact design. A) Enclosure with some components hidden to show solder terminal lug contact location, B) Solder terminal lug contact dimensions, C) detail view of solder joint location, which is no longer below the graphite electrode, D) cross section view with washer contact and sensor materials. ....	38
Figure 27: SCC test for solder terminal lug contact design compared with other graphite contact methods. Peak current was 5.16 mA and average was 4.58 mA. PT = Probe tip design, RC = Ring contact design, STLC = Solder terminal lug contact design. The STLC design had the lowest peak but highest average current. ....	38
Figure 28: Water channels for sensor materials packaging. A) Design variations, B) Drawing with dimensions in millimetres, C) CAD model with cut-out section view .....	40
Figure 29: Paper wicking tail test, paper tail extends 10 mm beyond edge of graphite electrode. A) test setup, graphite electrode on paper, B) pipette in frame, C) application of water with pipette at end of tail, water rapidly moves towards graphite electrode along paper tail, D) majority of water absorbed by graphite electrode. ....	41
Figure 30: Wicking tails first design for packaging, A) Wicking tails laser cut from printer paper to test fit, B) Folding pattern for assembly, C) Wicking tails assembled into packaging, top view D) bottom view .....	42
Figure 31: Filter paper tails redesign. A) paper pieces used in second design, B) image of packaging with second design in place .....	43
Figure 32: Drawing of sensor materials enclosure design .....	44
Figure 33: Electronics enclosure design. A) exploded view of electronics packaging, B) assembled with lid raised.....	45

Figure 34: Design alternatives for the complete water leak detector design. A) PCBs stacked, sensor to the side, B) everything stacked, C) PCB's side by side, sensor below. .... 45

Figure 35: Complete water leak packaging design for 3D printing. A) Top isometric view, showing pins on sensor packaging, B) Bottom isometric view, showing holes on electronics packaging, C) section view showing assembled leak detector unit interior. D) 3D printed assembly, E) lid removed to show electronics, and sensor enclosure opened to show graphite, Mg disc not shown ..... 46

Figure 36: Simulated water leak in petri dish with first complete water leak detector prototype 47

Figure 37: Additional filter paper barrier component addition to sensor enclosure, part number 6. .... 50

Figure 38: Drop testing setup (A-D). A) Packaging layout. The water leak sensors (Qty 15) are assembled into a shipping box along with wireless gateway box placeholders to represent a typical sensor system shipment. Foam is used to separate each sensor device, shown in B). Corrugated paper packaging is shown in red in A) and is clearly visible in C). D) Drop test steps reference image, showing target corner (1), edges (2-4) and faces (5-10). Post-drop inspection (E-G): E) Damage to corner of box, F) 3D printed electronics packaging with broken base, G) Some graphite material escaped from enclosure and is visible on foam layers..... 51

Figure 39: Relationship between OCV and activation time after the drop test. Voltage measured after activation time test with load removed. A) All test data, excluding sensor without Mg piece. B) All activation times below 1 minute, sample with snap fit issue removed. Linear fit and correlation coefficient,  $r = -0.48$ ..... 53

Figure 40: 3D printed version of sensor packaging, outsourced. A) Full leak detector, B) sensor enclosure, closed, C) sensor enclosure, opened. D, E) Close-up of location where annular snap feature would be located if the print detail was high enough. .... 55

Figure 41: A) Inspection dimensions for graphite cavity on 3D printed sensor enclosure, B) measuring graphite cavity diameter with digital calipers ..... 56

Figure 42: A) Self-discharging from water to magnesium via dry graphite B) No self-discharging since graphite is fully saturated (no dry areas) C) No self-discharging due to insulating barrier 57

Figure 43: Modified design, screws replace annular snap. A) Cross section view B) enclosure assembled, C) & D) cross section, before and after pressing insert into place with soldering iron tip ..... 59

Figure 44: New filter paper patterning. A) Pattern cut from 24 cm diameter filter paper sheets. B) Close-up of pattern, pieces with tails shaded..... 60

Figure 45: Post-assembly resistance check across sensor terminals. A handheld DMM can be used to quickly measure the resistance. .... 62

Figure 46: Injection moulded sensor packaging design. A) Opened sensor enclosure showing wiring partway through assembly. Magnesium, graphite, and filter paper not present, and the header pins are not yet mounted into the holes through the lid of the sensor enclosure. B) Completed sensor enclosure, and C) electronics enclosure. .... 62

Figure 47: Sensor electrical test results for injection moulded enclosure. A) OCV test condition, B) SCC test condition, C) Load test condition output power when $I_{\text{source}} = 50 \mu\text{A}$ , D) Load test condition output power when $V_{\text{source}} = 400 \text{ mV}$ .....	64
Figure 48: Beacon activation test for injection moulded packaging, with sensor output voltage and storage capacitor voltage measured. ....	66
Figure 49: Results of beacon activation testing, $n = 24$ samples, bin width = 2.5 s. ....	66
Figure 50: A) Mould CAD model. B) cross section showing compressed carbon electrode, C) moulds to produce electrodes with different diameters. ....	79
Figure 51: A) Instron Micro Tester 5548 sample holding grips, B) desktop controls with pressing mould in background, 3 samples in parallel .....	80
Figure 52: A) Magnesium plate, not sanded B) drawing with dimensions in millimetres. Thickness is 1.6 mm.....	81
Figure 53: Magnesium disc preparation. A) Punch and die set, B) Mg discs punching, trial and error, C) 3D printed part, holds Mg disc for sanding, D) sanding process, before and after.....	82
Figure 54: Overview of electrical system components. A) Block diagram schematic, B, C) CAD model of the two PCBs: B) EH and C), BLE, each with a 27 mm square footprint.....	83
Figure 55: A) Sensor equivalent electrical model with voltage source and series resistance, B) simplified electrical model of sensor supplying power to a pure resistance load.....	84
Figure 56: Relationship between $V_{\text{out}}$ , $P_{\text{out}}$ and $I_{\text{out}}$ for the sensor component, assuming constant $R_i = 400 \Omega$ . The approximate operating points when used in the water leak detector are shown. Maximum theoretical power output is 2.5 mW. ....	86
Figure 57: EH board block diagram.....	87
Figure 58: System architecture, showing data transmission starting at the water leak sensor, on to a gateway device, to the cloud, and then to a user.....	91

## List of Tables

Table 1: Comparison of commercially available spot water leak detection sensors .....	6
Table 2: Summary of water-based sensors with potential for self-powered devices.....	11
Table 3: OCV performance baseline for unpackaged sensor materials .....	22
Table 4: SCC performance baseline for unpackaged sensor materials.....	23
Table 5: CC load test performance baseline for unpackaged sensor materials.....	24
Table 6: Probe tip conditions and the effect on voltage, current, and power .....	26
Table 7: Comparison of graphite electrical contact methods by electrical performance testing ..	39
Table 8: Design considerations for water channel layout. A design hybrid between side and bottom channels is optimal. See Figure 28 for concept images of designs.....	40
Table 9: Yield rate and multiple use testing for first sensor prototype. After failure, test was not repeated, and is left blank intentionally. Yield rates are given relative to the first trial (18 samples) and relative to the number of samples that passed the previous trial.....	48
Table 10: Drop testing results for 10 samples from 1 m height in a shipping box.....	52
Table 11: Assembly steps for 3D printed design .....	54
Table 12: Actual 3D printed dimensions of graphite cavity versus specified dimension.....	56
Table 13: Actual injection moulded dimensions of graphite cavity versus specified dimension.	63
Table 14: OCV test results for injection moulded design of sensor enclosure.....	64
Table 15: SCC test results for injection moulded design of sensor enclosure.....	64
Table 16: Load test results for injection moulded design of sensor enclosure .....	65
Table 17: Summary of activation time results .....	67
Table 18: List of changes for injection moulding manufacturability .....	90

## List of Abbreviations

Abbreviation	Definition
BLE	Bluetooth Low Energy
CAD	Computer-aided design
CC	Constant Current
CNF	Carbon Nanofiber
CV	Constant Voltage
DC	Direct Current
DMM	Digital Multimeter
EH	Energy Harvesting
FDM	Fused Deposition Modelling
IoT	Internet of Things
MCU	Microcontroller Unit
NFC	Near-Field Communication
OCV	Open-Circuit Voltage
RF	Radio Frequency
SCC	Short-Circuit Current
SMU	Source Measurement Unit

# Chapter 1. Introduction

## 1.1. Background

Water damage is one of the costliest problems for homeowners. A report by Zurich Insurance Group claims water damage accounts for 57% of commercial real estate claims by number, and 73% by dollars lost [1]. Water leaks can result in the loss of hundreds or thousands of litres of water per day [2]. Leaks gone unnoticed can cause considerable damage, Zurich provides several examples of property damage with losses of half a million and more due to water pipe, tank, and hose failures [1]. There are many sources of water leaks, and the damage they cause is extensive, but preventative measures and early detection can help mitigate the issue. In the case of water leak detection, many solutions exist in the form of water leak detectors. Most commercially available water leak detectors can be broken down into several key components, such as in Figure 1.

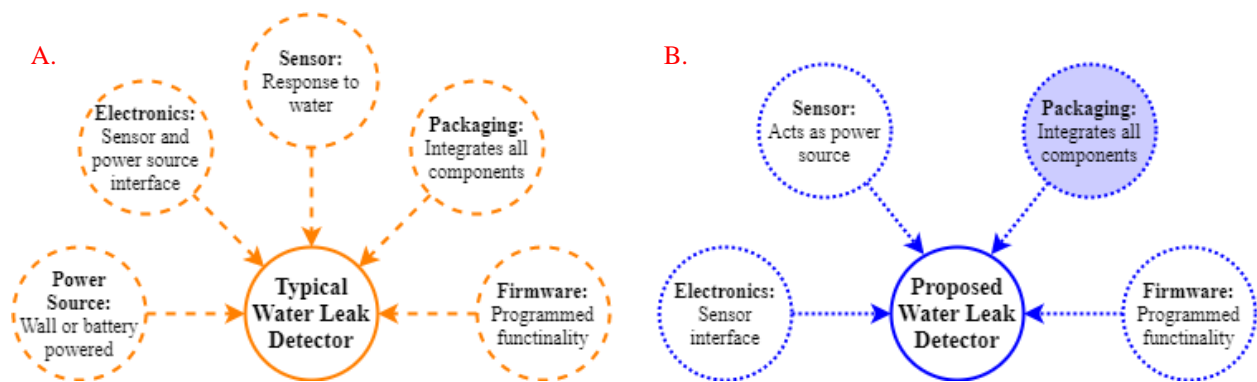


Figure 1: A) Components of a commercially available water leak detector, B) simplified design for the proposed “self-powered” water leak detector. The packaging (shaded) is the focus of this thesis.

The components are described in more details in the list below:

1. **Sensor:** First, the sensor component is the portion that undergoes some change in the presence of water. One common design is metal contacts separated by an air gap. When water fills this air gap, the resistance between the contacts decreases significantly, which is measured by the electronics.
2. **Electronics:** Interfaces to the sensor, for example, general-purpose input/outputs (GPIOs), are used to measure the changing sensor properties. A basic computer such as a microcontroller unit (MCU) is the decision-making center of the water leak detector and collects data from GPIOs. A wireless radio can send and receive data on the MCU.



3. **Firmware:** The microcontroller will typically be programmed with some custom firmware, specific to the water leak detector's application. This would include a set of logical actions to take if a water leak is occurring.
4. **Power Source:** A source of power, either a battery or an adapter to mains AC (alternating current) is needed to operate the MCU and radio. Typically, this also requires a battery management circuit to regulate battery consumption and extend life.
5. **Packaging:** Last, the entirety of the system is assembled into a housing, meant to expose the sensor to water in a specific way, while protecting the more delicate electronics components on the inside.

The design in Figure 1A is not too complex, but it does suffer from some notable drawbacks. First, the water leak detector's power supply can be problematic. The locations in which water leak detectors are needed are not necessarily close to electrical outlets for using the mains AC power. For this reason, many water leak detectors opt for the battery as a power source. However, the obvious drawback to a battery is that it will eventually require replacement. Consider a large residential building with water leak detectors installed in every bathroom, kitchen, and laundry unit. The task of replacing these batteries can become quite significant. Furthermore, the sensors can only be installed in locations where the device is easily accessible in the future, otherwise the battery replacement will not even be logistically feasible.

For this reason, it is of interest to find a solution for water leak detection that does not suffer from the power supply drawbacks of commercially available water leak detectors. The proposed water leak design in Figure 1B is a "self-powered" water leak detection device, which does not need a battery or a connection to external power. Instead, the device operates by utilizing the power output of a unique sensor design, essentially combining the power source and sensor component into a single part. This is possible by leveraging recent advances in self-powered moisture sensor research by colleagues [3, 4]. The operation is simplified as well, since the device will only be powered in the presence of water, the unit can assume a leak has occurred the instant it becomes active. Therefore, there are no electronics required to interface between the MCU and a sensor component.

## **1.2. Objective**

The efforts described in this thesis are on designing and developing a first-of-its-kind battery-free water leak detection device. Specifically, a mechanical enclosure needs to be designed that integrates the sensor materials, PCBs, and establishes electrical connection between the two of them. This housing should not decrease the electrical performance of the sensor significantly when compared with performance in an experimental setup. Otherwise, the sensor would not be able to supply sufficient power to the electronics of the water leak detector.

## **1.3. Thesis Outline**

The chapters of the thesis are explained here. Chapter 2 examines the literature for self-powered sensor devices as well as summarizes current water leak detector options. Chapter 3 discusses the test procedures used in later design chapters, establishes baseline performance metrics, and gives some background on design considerations when working with the selected materials. Chapter 4 involves the first prototype design, showing how each individual part of the design was added, followed by a performance assessment. Chapter 5 presents the second major design iteration, which improves upon many of the flaws from the previous. Chapter 6 is conclusions, recommendations for improvements, and future directions of work.

# **Chapter 2. Literature Review**

## **2.1. Introduction to Chapter 2**

There is a significant amount of research into self-powered water and moisture-based self-powered devices for the Internet of Things (IoT). Commercially, many companies sell water leak detectors powered from batteries or wall outlets. Up until now, however, none have bridged this gap between research in the field of self-powered devices and application-ready water leak detectors. Here, a look into the types of commercially available water leak detectors is done, with a focus on spot water leak detectors for buildings. Energy harvesting research is examined in a broad sense, followed by a targeted summary of potential energy sources that are water specific. Last, a summary of the prior work on a water-activated power source used for this detector is given.

## **2.2. Water Leak Detection Technology**

### **2.2.1. Types of Water Leak Detection Technology**

Water leaks can occur at the points of water consumption, for example, residential buildings, as well as along the distribution pipelines. Water leak detection for the two cases has some similarities but also key differences. A non-exhaustive list of currently employed leak detection methods for pipelines include acoustic emission sensors, accelerometers, hydrophones, fiber-optic sensors, gas injection, and inline inspection, as well as more traditional methods, such as a manual listening stick [5, 6]. Many of these technologies are deployed temporarily by on-site personnel in an area being scanned for leaks, and then removed when work is complete.

In the case of water leak detection in buildings, there are several approaches. One method of finding water leaks is by inspections, where skilled technicians, possibly with the help of equipment search for suspected water leaks. This can involve non-destructive approaches, such as thermal imaging [7], or destructive approaches, where wall or ceiling material is removed. Regardless of the technology used, an experienced technician is required to judge the building's signs of water damage [2].

A more permanent method of water leak detection in buildings involves water leak detectors. Here, the commercially available options are grouped into two main categories, flow measurement units and spot detectors. The principle of flow measurement devices is to measure your water consumption at the main water line entering the house. Some examples include Flowie, by Alert

Labs [8] and Flo by Moen [9]. When abnormal water consumption occurs, these devices can flag this as a potential water leak, prompting a user response. This makes it possible to detect water leaks in your home's water distribution system, in addition to gaining other features such as water consumption usage. On the other hand, spot detectors respond to the physical presence of water. Many devices available today use the same design. A set of two or more exposed metal contacts near the floor are joined by water pooling below the sensor, which changes the resistance measured across the contacts. Another approach uses a water leak detection cable, which comprises non-conductive and conductive materials twisted together axially, which can detect water anywhere along the cable's length by again measuring resistance changes [10]. Leak detection range extensions are typically offered by attaching these twisted cables to a spot detector [11, 12], or making another custom cable with metal contacts at the endpoint [13]. Other unique solutions exist, such as a spot detector from Honeywell which uses an expanding sponge material to close an alarm circuit [14], but the metal contact design and the detection cable are by far the most widely used.

### **2.2.2. Water Leak Detectors for Residences and Commercial Spaces**

There are a variety of solutions for spot water leak detection in residential and commercial settings. Table 1 is meant to give examples for some of the more common types of sensors available, along with their features and pricing, but does not represent the distribution of types of solutions.

On one hand, there are inexpensive solutions, which typically use older technology and lack features such as remote monitoring, or IoT compatibility, instead using audible alarms [14, 15]. The other option is the newer, pricier wireless devices such as spot detectors and flow measurement devices [8,9,11-13,16-20]. Many use cellular or Wi-Fi signals paired with mobile apps to alert a homeowner of water leaks regardless of location. The price difference is noticeable between the types, with the least expensive options costing CAN\$5 to CAN\$10, while the advanced flow measurement units can exceed CAN\$1000 in some cases.

### **2.2.3. Issues with Current Water Leak Detection Systems**

The types of water leak detection solutions presented in sections 2.2.1 and 2.2.2 are fully capable of detecting water leaks in residential or commercial building, however they do suffer from drawbacks. Some systems rely on the flow of water in pipes and are therefore not suited to detect

**Table 1: Comparison of commercially available spot water leak detection sensors**

Company	Product Name	Price (CAN\$)	Description	Sensor Type	Power Source	Ref
Honeywell	RWD14	5	Audible alarm, one time use	Sponge + Metal contacts	Battery	[14]
The Basement Watchdog	Watchdog Water Alarm	12	Audible alarm	Metal contacts	Battery	[15]
Govee	Wi-Fi Water Sensors Alarm	14	Smartphone alerts + audible alarm	Metal contacts	Battery	[16]
Wasserstein	AC Powered Smart Wi-Fi Water Sensor	27	Smartphone alerts + audible alarm	Metal contacts	AC Outlet	[17]
Wasserstein	Wi-Fi Water Leak Sensor	29	Smartphone alerts + audible alarm	Metal contacts	Battery	[18]
Phyn	Smart Water Sensor	50	Smartphone alerts + audible alarm + visual alarm	Metal contacts	Battery	[19]
Moen	Smart Water Detector	70	Smartphone alerts + audible alarm + visual alarm	Metal contacts	Battery	[13]
Nowa	Flood / Freeze Sensor	79	Smartphone alerts	Metal contacts	Battery	[12]
Alert Labs	Floodie	125	Smartphone alerts + audible alarm	Metal contacts	Battery	[11]
Alert Labs	Flowie	595	Smartphone alerts, measurement features	Flow measure	AC Outlet	[8]
Phyn	Phyn Plus Smart Water Assistant + Shutoff (2 <sup>nd</sup> Gen)	629	Smartphone alerts, measurement features, automatic shutoff	Flow measure	AC Outlet	[20]
Moen	Flo Smart	750 to 1200	Smartphone alerts, measurement features, automatic shutoff	Flow measure	Outlet	[9]

other sources of water leaks, such as water ingress from a leaking roof. Others are outdated, such as audible and visual alarms, which do not readily scale for large applications, and are of no use without someone present to hear the alarm. Some devices are limited to a certain number of sensors per installation hub, and others rely on non-scalable Wi-Fi-based installation. One of the largest drawbacks is the placement of spot detectors is limited, since water leak detectors almost all rely on batteries. Like smoke alarms, replacement of batteries is inevitable, and so placing water leak detectors in hard-to-reach areas such as behind large appliances, or even within walls and ceilings does not make sense. Some systems do not quote a battery lifetime in their datasheets [15], since the sensor will deplete the battery rapidly upon activation. Other sensors have short battery lives, as low as 6 months in some cases [18], while others give optimistic lifetimes, such as “up to 2-year battery life” [19], with no guarantees. Some wall-powered units exist [17], however these will

require the need for additional wiring, which incurs additional costs, or might not even be possible for all areas at risk of water leaks. Aside from the spot detectors, the remaining options for detection such as manual inspections and pipeline-oriented sensors are not appropriate for a typical building case. Inspections are not a realistic solution to detect water damage, as a single water leak can cause hundreds of thousands in damage in a matter of days [1]. Other advanced water detection technologies are designed for large, single pipes as one would find in distribution systems [5].

#### **2.2.4. IoT for Water Leak Detection**

In 2021, the number of connected IoT devices exceeded 12 billion [21]. IoT technologies are very commonplace in many industries and applications [22], and furthermore, many different applications and industries can be disrupted by the IoT [23] if they have not been already. While there are many water leak detection solutions that exist, there are few that match the goals of IoT devices. For a real IoT water leak detection or management system, a scalable, low-cost deployment of sensor nodes throughout a building's infrastructure are needed. This is not commonplace, with spot detectors exceeding CAN\$100 in some cases. The most common issue, however, is the dependence on batteries for sensor operation. For large IoT deployments, we cannot keep relying on batteries as they are “expensive, bulky, and hazardous” [24]. and as Miorandi states “the need to replace batteries from time to time represents a huge barrier to the widespread development of such technology” regarding IoT deployments [25]. While some sources disagree, pointing to the increasing lifespans of batteries [26], the fact remains that battery replacements, however infrequent, are a significant limitation on the potential use cases for water leak detectors.

### **2.3. Battery-Free Sensor Technologies**

In this project, a design is developed for a self-powered water leak detector, To the best of our knowledge, this device is the first of its kind for water leak detection. However, other battery-free technologies exist for other applications, in various stages of development, from research to commercial product.

#### **2.3.1. Energy Harvesting Devices**

Kiziroglou defines energy harvesting (EH) as “the collection of small amounts of ambient energy to power wireless devices” [27], while Kansal et al. define “an energy-harvesting node as any system which draws part or all of its energy from the environment” [28]. In the context of battery-

free sensor devices, EH is one obvious solution that comes to mind. One way to categorize the components of an EH system is presented in [28], where the three parts are the source, harvester, and load. In the case of the proposed water leak detector, the source would be the sensor materials, the harvester would be an electrical circuit designed for the application, and the load would be a wireless communication device.

There are many mechanisms for EH, such as mechanical, piezoelectric, electrostatic, thermoelectric, and electromagnetic [27], as well as radio frequency (RF) [29]. Some of these mechanisms have been used to develop proof-of-concept designs where the EH source is integrated into an application. One interesting harvesting method uses mechanical energy to vary a coiled yarn's capacitance [30]. In the realm of piezoelectric materials, researchers in [31] used a "vertical nanowire array integrated nanogenerator" to drive additional UV sensor and pH sensors in a single device. In [32], a piezoelectric material integrated into the straps of a backpack generates 45 mW of power, which would be sufficient to power a wireless radio available on the market today. In another report, motion in a variable capacitor powered a custom radio transmitter design, demonstrating a device with potential biosensor applications [33]. Thermoelectric generators (TEGs) have been used to harvest body heat, and in one example, this power was used to drive an electrocardiogram system in a wearable device [34]. In a similar application, a system-on-chip was designed to gather electrocardiogram and other medical patient data by using a TEG power source for steady-state operation, as well as RF energy harvesting to "kick-start" the device [35]. Another type of energy harvesting method is from triboelectric sources, in which layers of material slide along one another, producing electrical power. One triboelectric nanogenerator was used to detect pressures, such as applied water droplet [36], whereas another, larger triboelectric generator would harvest energy from a wind or water movement via a turbine [37].

Beyond research findings, energy harvesting devices have been deployed in commercial applications, although their use is less common. One very interesting example is ONiO.zero, designed by ONiO [38]. The product is an energy harvesting microcontroller, which integrates several energy harvesting mechanisms into the same package as the computing device, including radio frequency, piezoelectric, thermoelectric, and solar harvesters. This product would be integrated into larger systems, such as sensors or other small electronic devices for endless, battery-free operation. Another example, in this case, an end-product for direct use, is the steam trap sensors produced by everactive, called Eversensors [39]. These devices rely on heat and light

sources in industrial environments to monitor steam traps. The company, everactive, has also developed an accompanying wireless protocol suited for their sensor design, allowing low power communication among their sensor nodes.

While there are many promising examples of energy harvesting devices, there is a large discrepancy between the quantity of research and number of market-ready systems. This can likely be attributed to some of the typical challenges with EH; devices often have issues with timely execution, and limited resources [24, 28] due to intermittent and unreliable power sources. For water leak detection, these problems would be catastrophic, if, say for example, the power source was not available until several hours or days after the time a water leak occurred. Water leaks instead must be detected in a timely manner, regardless of the availability of power to harvest. Many of the other devices proposed rely on thermal, light, radio frequency, and mechanical sources of energy, and while these are reliable in some cases, water leak detection may be required in spots where thermal gradients do not exist, light does not reach, or wireless transmissions are infrequent.

### **2.3.2. Radio Frequency ID and Near-Field Communication Tags**

Another method of avoiding the use of batteries is using Radio Frequency ID (RFID) tags. Near-field communication (NFC) tags are a specific category of these that are commonly employed. These tags may be used on devices with a power source, such as a battery, but the focus here is on sensors where the tag itself, when coupled with a harvester, is the source of power. While these devices operate in a similar principal to RF-based EH devices, they are typically expected to be used over short periods of time. A transmitter, such as a smartphone, is brought in proximity of the sensor device's RFID or NFC tag, and the sensor can power on by making use of energy gathered from the wireless transmission [40]. Some examples include a soil moisture sensor with an NFC tag [41], gas detection with a modified NFC tag [42], and an RFID tags integrated into a smart diaper for wetness sensing [43].

The main drawbacks in the context of water leak detection would be the requirement of readers to constantly scan devices. To maintain an updated status on water leak events, frequent scanning would be required. This problem is made worse by limited range. Depending on tag design, the range is limited to 1 m [40, 43]. While the NFC and RFID based approaches are very low cost in many cases, they are not well-suited to water leak detection in large buildings.



### **2.3.3. Moisture-Based and Water-Based Generators and Sources**

Research has also been done into various types of energy generating devices that interact with water in a variety of ways to produce usable output power. These are ideal for water leak detection as in the event of a water leak, the power source will always be present, rather than if the power source was unrelated, such as solar or mechanical vibrations. Some sources of energy include the evaporation of water, flow of water, and the adsorption or desorption of water. Other studies rely on chemical reactions with water. Multiple studies also combine more than one mechanism together to produce a power generating device. This section reviews some of these designs, which are listed in Table 2, with a focus on papers showing the electrical energy or power outputs that are successfully harvested from the device.

There are a wide range of devices that rely on liquid water or water vapor to produce usable electrical power. Most however, do not produce sufficient power to supply a wireless device without either scaling the generator size, or having a very slow response time due to the time needed to charge a storage capacitor. The chemical reaction-based sensors described in [3, 44, 45] do not offer a theoretical indefinite use, however, the output power is at least a magnitude greater than alternatives, and power availability is guaranteed in the event of a water leak. This makes them ideal candidates for a self-powered water leak detector design.

**Table 2: Summary of water-based sensors with potential for self-powered devices**

Mechanism(s)	Description	Size	Electrical Output	Ref
Chemical reaction	CNF-Mg sensor reacts with liquid water and water vapour	Diam 1.5 cm = 1.77 cm <sup>2</sup>	200 $\mu\text{W}/\text{cm}^2$ (peak)	[3]
Chemical reaction	Oxygen plasma-treated CNT yarns interact with water	24 mm long	77 $\mu\text{W}/\text{cm}^2$ (peak)	[44]
Chemical reaction	Mg and PANI foam with water application in coin cell design	Diam 2.0 cm = 3.14 cm <sup>2</sup>	1140 $\mu\text{W}/\text{cm}^2$ (average)	[45]
Evaporation	Evaporation changes membrane curvature to drive a generator and a small car device	9.6 cm x 7.6 cm = 73.0 cm <sup>2</sup>	0.025 $\mu\text{W}/\text{cm}^2$ (average)	[46]
Evaporation	Titanium oxide nanowires, response to human breath	1.2 cm x 1.2 cm = 1.44 cm <sup>2</sup>	4 $\mu\text{W}/\text{cm}^2$ (peak)	[47]
Evaporation	Hybrid generator and storage from thermal and mechanical energy	5.0 cm x 5.0 cm = 25.0 cm <sup>2</sup>	0.0099 $\mu\text{W}/\text{cm}^2$ (average)	[48]
Evaporation, streaming potential	Water movement produces voltage in a carbon black-glass fiber hybrid film	5.0 cm x 5.0 cm = 25.0 cm <sup>2</sup>	0.038 $\mu\text{W}/\text{cm}^2$ (peak)	[49]
Evaporation, streaming potential	Carbon-black sheets in water generate electrical power	1.0 cm x 2.5 cm = 2.5 cm <sup>2</sup>	0.021 $\mu\text{W}/\text{cm}^2$ (average)	[50]
Evaporation, streaming potential	Water channels in wood block produce voltage during water evaporation	5.0 cm x 5.0 cm = 25.0 cm <sup>2</sup>	0.018 $\mu\text{W}/\text{cm}^2$ (average)	[51]
Evaporation, streaming potential	Electricity from water movement in silicon nanowire array channels	2.0 cm x 2.0 cm = 4.0 cm <sup>2</sup>	6 $\mu\text{W}/\text{cm}^2$ (average)	[52]
Streaming potential	Capacitor structure from CNTs for energy harvesting and storage	3 cm <sup>2</sup>	90.8 $\mu\text{W}/\text{cm}^2$ (peak)	[53]
Streaming potential	Carbon paper-Al <sub>2</sub> O <sub>3</sub> nanoparticle layer-carbon paper structure	2.0 cm x 2.0 cm = 4.0 cm <sup>2</sup>	3.7 $\mu\text{W}/\text{cm}^2$ (peak)	[54]
Streaming potential	Ion transport through graphene hydrogel membrane under applied pressure	Diam 3.5 cm = 9.6 cm <sup>2</sup>	0.63 nA/cm <sup>2</sup> , function of pressure, concentration	[55]
Adsorption and desorption	Graphene-oxide film produces power under human breath	0.5 cm x 0.5 cm = 0.25 cm <sup>2</sup>	0.42 $\mu\text{W}/\text{cm}^2$ (peak)	[56]
Absorption and desorption	Coiled graphene fibers produce rotation under humidity change	20 cm fiber length	1 mV open circuit 40 $\mu\text{A}$ short circuit	[57]
Sorption and desorption	Water gradient causes film actuation, can drive a generator	2.0 cm x 4.0 cm = 8.0 cm <sup>2</sup>	0.0007 $\mu\text{W}/\text{cm}^2$ (average)	[58]
Drawing potential	Graphene monolayer interaction with sliding water droplet	Not given	0.019 $\mu\text{W}$ (peak)	[59]

## 2.4. Background on Prior Sensor Materials and Electronics Work

### 2.4.1. Sensor Materials

Before proceeding with the more detailed mechanical design process, it is important to understand the materials around which the sensor device is built, and for which the packaging is designed. The water sensor at its core is composed of a layer of carbon and a layer of magnesium, seen in Figure 2. The mechanisms of the reaction that produce the voltage and current when water is applied are detailed in prior work by colleagues [3, 4].

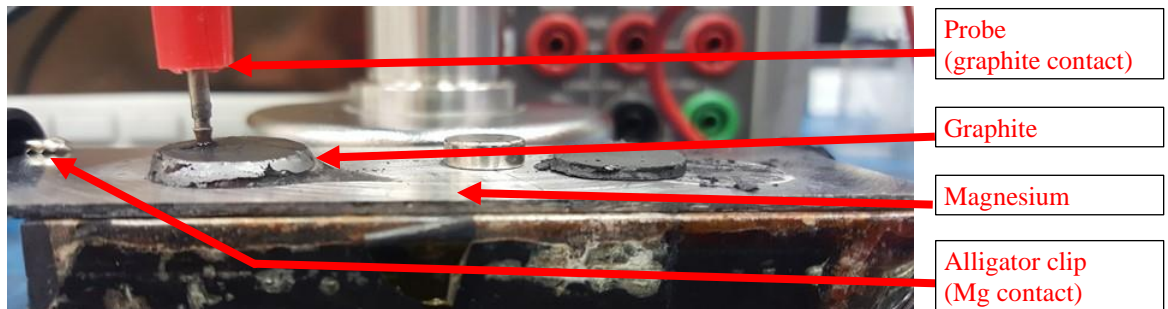


**Figure 2: Sensor materials in electrical test setup, graphite design shown**

The following subsections outline the prepared carbon and magnesium electrodes used in all water leak sensor tests in subsequent chapters.

#### 2.4.1.1. Carbon Electrode

The carbon layer can be composed of carbon nanofibers (CNF), as in [3], or graphite, as was done in [4]. While some early sensor packaging designs were done with the carbon nanofiber design, the graphite-based sensor was preferable for two reasons. First, the current output was consistently much higher than the carbon nanofiber design and second, the carbon layer made from graphite could be manufactured more easily, using a compression method with a mould. A graphite electrode is shown in Figure 3A. One filtering-based fabrication process for CNF electrodes is detailed in [3], while the descriptions of the pressing method for electrode manufacturing are provided in Appendix A.1. The press method is used for this work.

#### 2.4.1.2. Magnesium Electrode

The magnesium electrode is blanked from magnesium alloy AZ31 sheet stock, 1.6 mm thick, and blanked to a diameter of 18.65 mm, shown in Figure 3B. More details are provided in Appendix A.2.

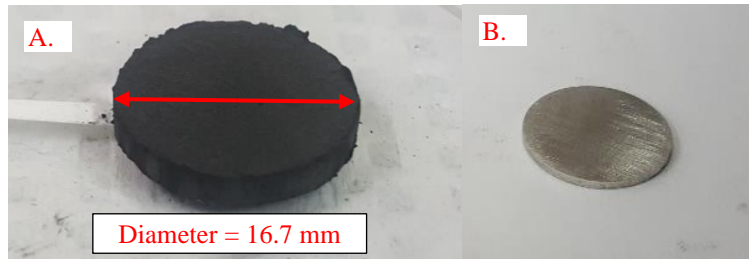


**Figure 3: Electrodes produced for sensor use. A) Graphite electrode, B) magnesium electrode.**

### **2.4.2. Electronics**

The electrical designs used in the sensor are developed by colleagues. The two PCB's serve distinct functions in the water leak sensor. The sensor outputs DC (direct current) power, but at a voltage too low for the BLE device. First, the energy harvesting (EH) board serves three functions: (1) it boosts the sensor's output voltage with a DC/DC converter, (2) it regulates power usage by storing energy in a large capacitor, and (3) it provides a stable input voltage for the second PCB, the Bluetooth Low-Energy (BLE) board. Without the EH board, the sensor cannot meet the voltage requirements and the transient power requirements of the BLE board. The BLE board is responsible for wireless transmissions, which, when detected by a BLE receiver, indicate a water leak has occurred. More details on the two boards are given in Appendix B. These PCBs must be integrated into the same enclosure as the magnesium and graphite sensor, and an electrical connection from the EH board to the sensor materials must be made. This integrated device will become a water leak detector.

## **2.5. Summary of Chapter 2**

In this chapter, a review of the current methods for water leak detection is presented. There are several techniques and devices used today for water distribution and end-use leak detection, however there is clearly room for improvement, notably with issues in scalability, cost, and battery-dependence. A summary of some types of energy harvesting, self-powered and battery-free sensor technologies is also given, however there are no current battery-free water leak detectors on the market today. The potential exists to develop such a device, as the electronics for energy harvesting can be paired with a water-based power generator.

# **Chapter 3. Methods and Design Considerations**

## **3.1. Introduction to Chapter 3**

Chapter 3 details the test methods used in later chapters to assess the performance of the sensor device when packaged into a designed enclosure. These include electrical tests to determine power output of the sensor materials themselves, and application-focused tests that characterize the entire water leak detector device in response to a simulated water leak event. In addition, a baseline or control level of performance is measured for reference, and some design considerations from previous observation of the sensor materials are explained.

### **3.1.1. Comments on Selection of Test Duration**

One difficult question to answer for designing tests for the water leak detector project is how long should the test last? In this Chapter, different test types are presented, including electrical tests and response time tests, which involve measuring sensor behaviour versus time. The moisture-based generator can produce usable output power for durations on the order of hours, depending on the current requirements and the volume of water applied [3, 4]. For a water leak detector however, users should be alerted promptly to mitigate water damage. There is a lack of usable standards against which spot detectors are qualified. Most commercial solutions offer alerts to water leaks in under 10 seconds; here, we aim to keep the device response below 1 minute. A response time within the first minute would keep performance within one order of magnitude of alternatives. Additional data is collected beyond the 1-minute interval so that the performance of failed devices can be measured in more detail, so a 5-minute time interval is chosen. Running the test for longer is possible, however the critical performance window is on device start-up at the application of water. Beyond 5 minutes the response is of less interest, as a sensor that has not notified a user of a water leak in this window would be of no value. This 5-minute window is used to qualify all sensor devices performance throughout the project.

## **3.2. Electrical Performance Testing**

With an understanding of the materials used in the device, we can investigate the experimental methods used to quantify the functionality of the sensor. These metrics do not directly assess the quality of the complete water leak sensor, but rather are used to quantify the sensor materials performance when assembled in the sensor packaging. These electrical tests can be used compare

design iterations of the sensor packaging, or to compare the performance of a packaging design to the unpackaged sensor materials. In addition, the following tests can be used to quantify the impact of an environmental condition applied to the sensor, such as a drop test.

The reason the electrical performance is so critical to the device, is because the power output from the sensor must be sufficient for the BLE functionality. By ensuring the electrical performance of the sensor device is adequate and repeatable, we can also ensure that the BLE device will be activated reliably and in a timely fashion when a water leak does occur. As previously explained, the device performance is measured across the first 5 minutes for all tests.

### 3.2.1. Electrical Performance Testing Equipment

The 34411A Digital Multimeter (DMM), 6 ½ Digit by Agilent (now Keysight) [60] shown in Figure 4A is used to measure DC voltage and current of the sensor or accompanying electronics. The B2911A Precision Source/Measure Unit (SMU) by Keysight [61], shown in Figure 4B, can source or sink a fixed voltage or current while simultaneously measuring the other. Configuration of the DMM and SMU, as well as data collection from each is done with Keysight BenchVue Software [62] on a desktop computer through USB connections. The complete test setup for a given device under test, or DUT, is shown in Figure 4D. The DUT could be just the sensor electrodes tested in open air by applying water, or it could be the sensor materials assembled into an iteration of the packaging design, as shown in Figure 4C.

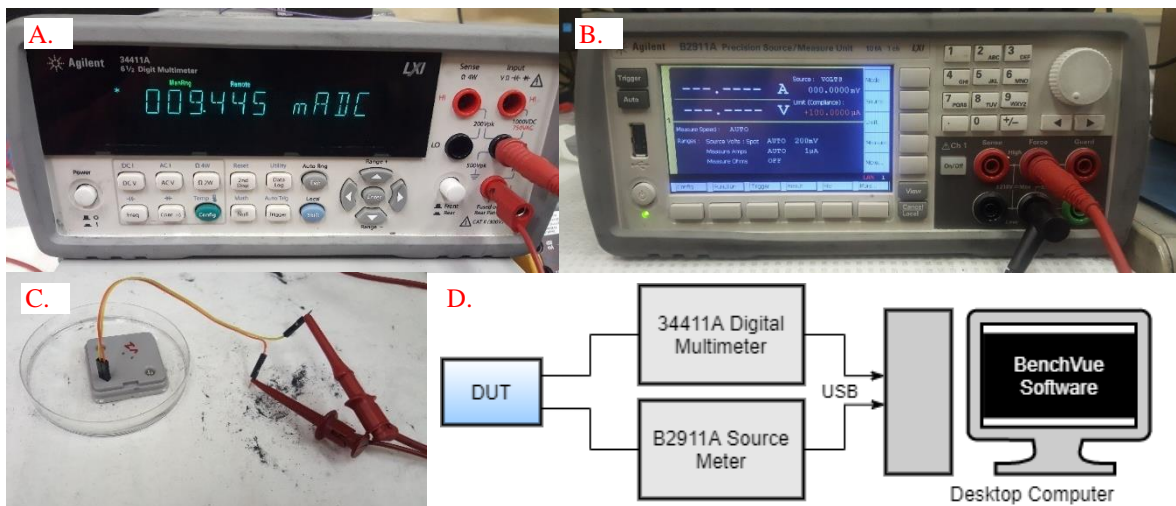


**Figure 4: A) DMM used in electrical performance testing, image taken while measuring DC current, B) SMU used in electrical performance testing, C) sensor packaging from Chapter 5 connected to test leads, D) schematic of testing setup for collecting and logging DMM and SMU data**

### 3.2.2. Open-Circuit Voltage (OCV) Test Procedure

The OCV of the sensor measures the output voltage with no load attached, meaning no current flows from the device. As seen in Figure 5, the test leads from the DMM are simply attached to the positive and negative terminals of the sensor packaging, which are internally connected to the magnesium and carbon portions of the sensor. The DMM is configured as a voltmeter, then the sensor packaging is placed in a petri dish with 2 mm of water. The voltage output is logged versus time in BenchVue. Two key metrics from the test are the maximum OCV,  $V_{OC,MAX}$ , and the average OCV over 5 minutes,  $\overline{V_{OC}}$ .

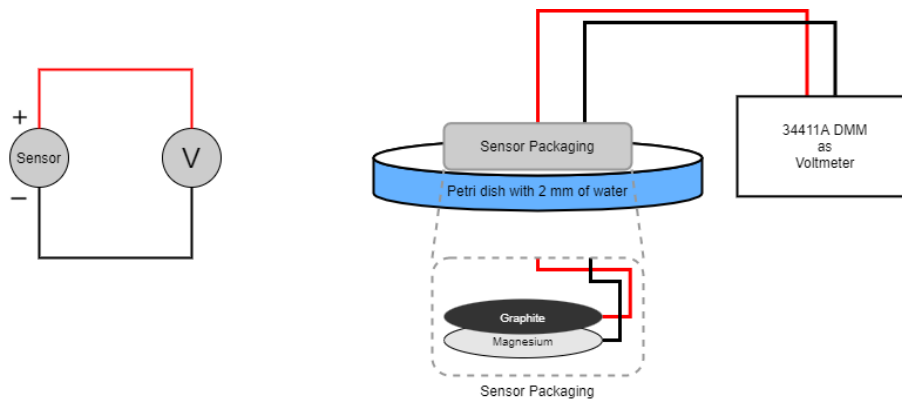


Figure 5: OCV test setup, sensor in packaging, electrical schematic shown left

### 3.2.3. Short-Circuit Current (SCC) Test Procedure

The SCC test measures the output current when the electrodes are connected with a zero-resistance load, meaning the current reaches its maximum value and the voltage is zero. As seen in Figure 6, the test leads from the DMM are attached the same way as in the OCV test. The DMM is configured as an ammeter, then the sensor packaging is placed in a petri dish with 2 mm of water. The current output is logged versus time in BenchVue. Two key metrics from the test are the maximum SCC,  $I_{SC,MAX}$ , and the average SCC over the first 5 minutes,  $\overline{I_{SC}}$ .

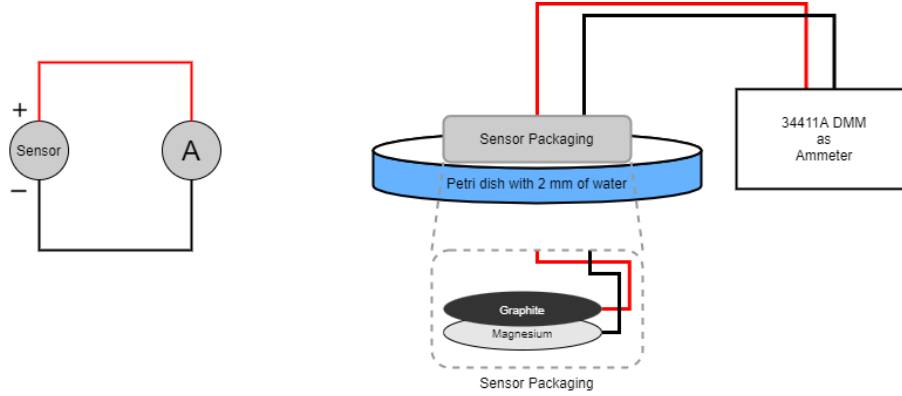


Figure 6: SCC test setup, sensor in packaging, electrical schematic shown left

### 3.2.4. Load Test Procedure

Load testing involves testing the sensor’s voltage and current output simultaneously, by forcing one while measuring the other. The SMU acts as a load in this test, but continuously adjusts its impedance to keep either the voltage or current constant. This is useful since the power output of the sensor can be determined, whereas in open-circuit and short-circuit conditions, the power output across the load is 0. Furthermore, by carefully selecting the fixed current or voltage, the power can be determined at a specific operating point relevant to the sensor application. In Figure 7, the B2911A used to perform the load test.

Two possible setups are shown, for either the constant-current (CC) or constant voltage (CV) load test. Test lead configuration and water application remain the same. The voltage and current outputs are both recorded versus time, allowing power to be calculated by multiplying the two together at every instant in time. The constant current or voltage for each test is selected from the predicted operating points of the sensor device when used in the water leak detector. For the constant current load test,  $I_{CC} = 50 \mu\text{A}$  is used to represent the steady-state operation in BLE transmission mode. For the constant voltage test,  $V_{CV} = 400 \text{ mV}$  is selected to represent the input voltage used by the EH board when charging the on-board capacitor. More details on the selection of operating points and the relationship between sensor voltage, current and power output are given in Appendix B, section B.2. For the CC load test, the average voltage,  $\overline{V_{CC}}$ , and the average power,  $\overline{P_{CC}}$ , are calculated over the first 5 minutes, whereas for the CV load test, the average current,  $\overline{I_{CV}}$ , and average power,  $\overline{P_{CV}}$ , are calculated.



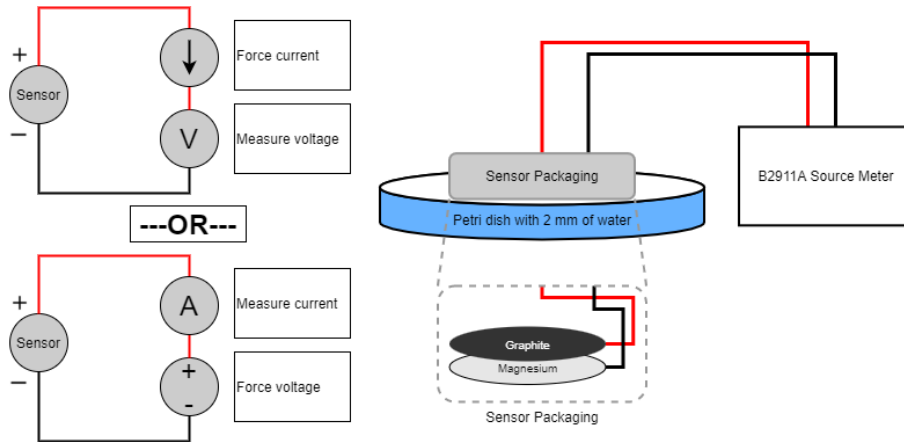


**Figure 7: Load testing test setup, sensor in packaging, electrical schematic shown left for constant current and constant voltage test**

It is important to note that the test is carefully controlled such that the SMU always sinks current, and the sensor output voltage is always positive. If, for example, the load current was set higher than the sensor’s SCC value (maximum current), the SMU would still force this specified current value, and the sensor voltage would go negative. This means the sensor would instead draw power from the SMU, instead of being tested as a power source. A similar condition occurs if the voltage specified is too high. To avoid these scenarios, the SMU is only enabled once the sensor’s voltage has risen, indicating the sensor is activated.

### **3.3. Water Leak Detector Performance Metrics**

The following metrics and conditions are used to evaluate the complete sensor device performance. Some tests produce metrics that are directly related to sensor performance in the field, for example, beacon activation time, whereas others must be further evaluated with electrical testing after the condition, for example, drop testing.

#### **3.3.1. Beacon Activation Time**

The beacon activation time measures the time from application of water until a user is made aware of the water being applied. In the case of the proposed water leak detector, the electronics transmit water leak detection information using a BLE Beacon, which is later transmitted over cellular networks, through cloud services and to an end user. This project concerns the design of the sensor device only however, and so the beacon activation time can be measured as the time from application of water until the Bluetooth signal is transmitted, since the remainder of the data

transmission is not affected by the packaging design. Figure 8 shows the test setup to measure the activation time.

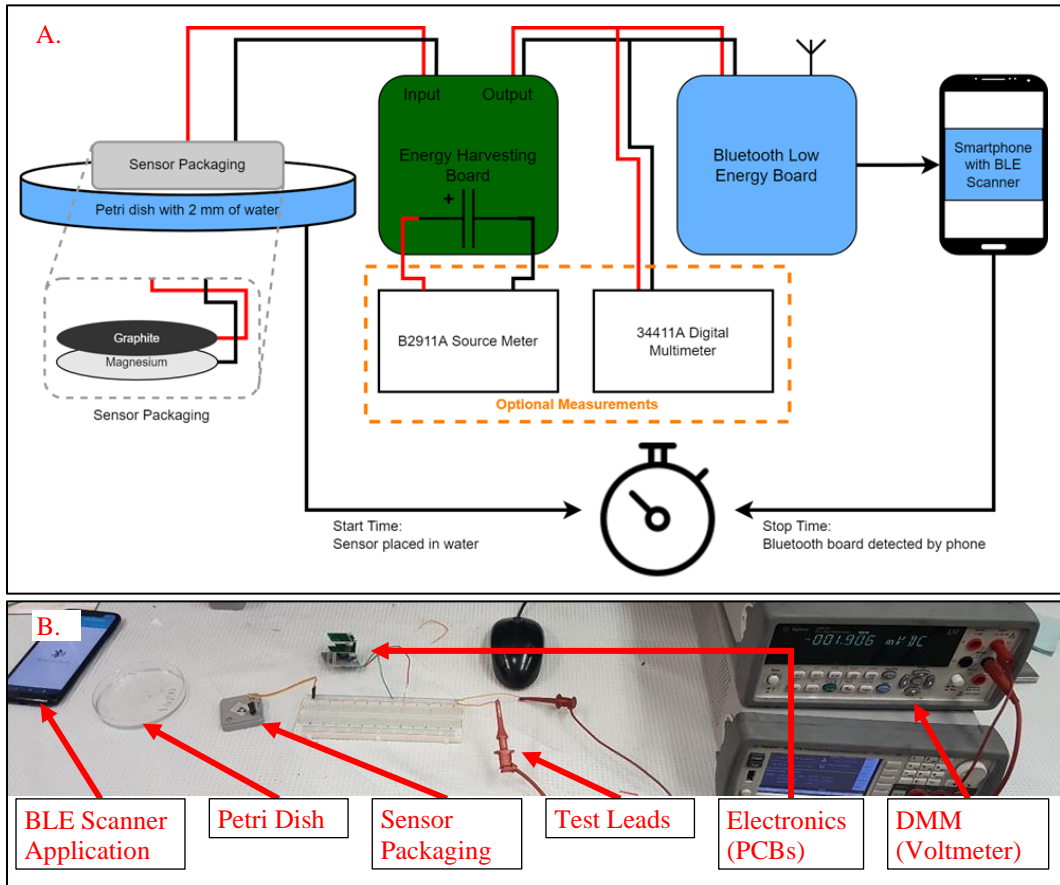


**Figure 8: Beacon activation time test setup including BLE scanning application on a mobile phone. A) Example schematic, B) actual test with sensor output voltage measured, stopwatch timer not shown**

In addition to the sensor packaging, the sensor electronics must be present to generate a BLE signal. Since a failure to activate the BLE board would result in no data for that test run, additional voltages can be measured to assess the source of test failures should one occur. This can help drive design changes to the packaging, but more importantly the electronics. However, measuring these voltages means the test must be conducted with the electronics packaging in a disassembled state, seen in Figure 8B. If the BLE board is not activated within 5 minutes, the activation time test is stopped, and the sample is simply marked as a failure.

### 3.3.2. Yield Rate Testing

Yield rate testing uses a very similar test setup to activation time testing, as shown in Figure 8. However, for yield rate testing the purpose is not to measure response time, but instead measure

only the percentage of water leak detectors that activate the BLE beacon. For yield rate testing, the time is not recorded for each sensor, and instead, a pass or fail is assigned if the sensor activates the BLE electronics within a pre-selected time window, typically 5 minutes. Since the stopwatch timer is still required for yield rate testing, then performing the activation time test requires very little additional effort. The two performance metrics, average activation time and yield rate, can be derived from just running the activation time test, rather than running two independent studies.

### **3.3.3. Multiple Use Testing**

The sensor's power output will decrease over time, and so the water leak detector has a limited lifespan upon activation. One point of interest is whether the water leak detector can be used for multiple water leak events, or whether the sensor materials should be considered single use. Eventually, the sensor will no longer output sufficient power to operate our electronics, however the time at which this occurs could be affected by the packaging design. This lifetime could be consumed through a single, prolonged water leak event, or multiple, shorter water leak events. Multiple use testing involves applying multiple shorter water leak events, by quickly exposing a sample group of sensors to water and checking metrics such as beacon activation time, yield rate, or power output via a load test. The sensor performance can be compared from trial to trial.

### **3.3.4. Drop Testing**

Water leak sensors can be subjected to impact during transport or during installation processes. While drop testing should be done to check the packaging materials and electronics under a drop condition, the key interest here is how the sensor materials respond to the drop test condition when packaged into the designed enclosure. Post-drop, a combination of visual inspections and electrical tests can be done to determine the effect of the drop test on the sensor device's performance. As explained later, some drop testing was done by dropping the packaging design directly onto a floor, however the device was not able to withstand these impacts. A more relaxed drop test was later done with the sensor devices packaged into a shipping box, to evaluate the tolerance to impact during transport.

## **3.4. Unpackaged Sensor Electrical Performance**

The sensor performance is evaluated with no packaging to provide a set of metrics when evaluating the packaged sensor performance. The three tests of interest are the open-circuit voltage, short-circuit current, and load testing under constant current. The tests included here are conducted with

graphite-based carbon electrodes, since this is the material eventually used in all packaging designs.

### 3.4.1. Unpackaged Sensor Electrical Test Setup

The previous electrical test schematics in Section 3.2 included schematics for testing with a packaged sensor device. However, these initial baseline tests are conducted with just the sensor materials, as shown in Figure 9. A close-up image of the test setup was previously shown in Figure 2. The electrical connections from materials to the DMM or SMU, however the hardware used to connect the two is slightly different. Rather than header wires, a probe connects to the carbon electrode, and an alligator clip connects to the magnesium plate. A pipette is used to apply a specific volume of water to the carbon electrode directly. Typically, 0.5 mL is used for these tests. The choice of DMM or SMU as well as the wiring is identical to the schematics in Section 3.2.

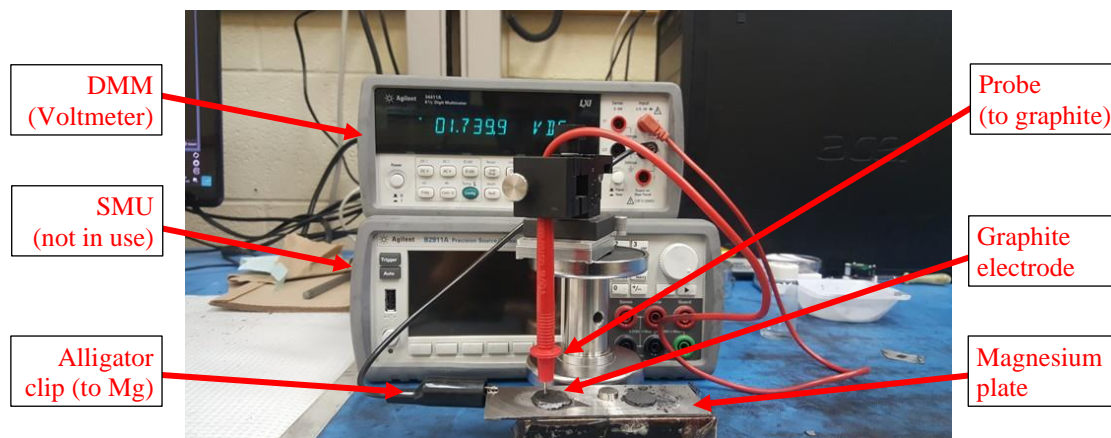
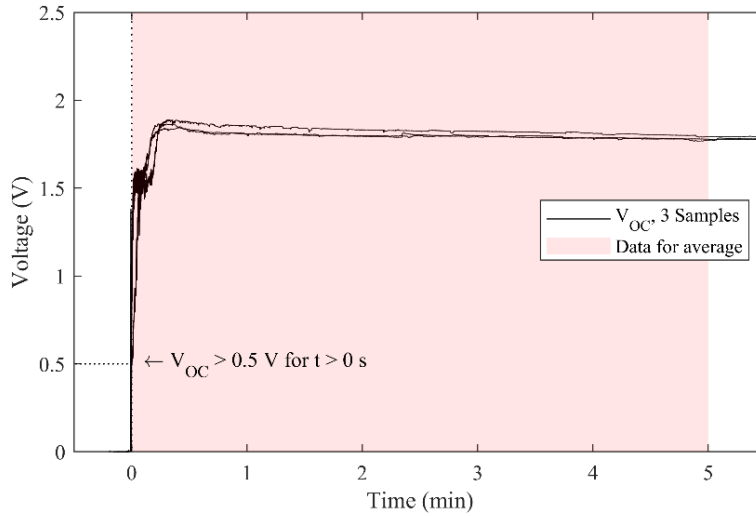


Figure 9: Unpackaged sensor materials test setup

### 3.4.2. OCV Performance Baseline

Typical sensor performance, unpackaged, with 0.5 mL of water applied via a pipette, is evaluated for 3 samples over the first 5 minutes of the OCV test. Voltage measurements are presented in Figure 10.



**Figure 10: Unpackaged sensor materials performance in OCV test condition. Window for computing average OCV shown in red. Data is time-shifted such that the sensor response occurs at  $t = 0$  s, where the sensor response event is the first point that  $V_{OC}$  exceeds 0.5 V**

The maximum and average OCV are calculated for each sample, as well as an average across the samples, shown in Table 3.

**Table 3: OCV performance baseline for unpackaged sensor materials**

Measurement	Sample 1	Sample 2	Sample 3	Average
$\overline{V_{OC}} / (V)$	1.79	1.79	1.81	1.80
$V_{OC,MAX} / (V)$	1.85	1.87	1.89	1.87

### 3.4.3. SCC Performance Baseline

Typical sensor performance, unpackaged, with 0.5 mL of water applied via a pipette, is evaluated for 3 samples over the first 5 minutes of the SCC test. Current measurements are presented in Figure 11.

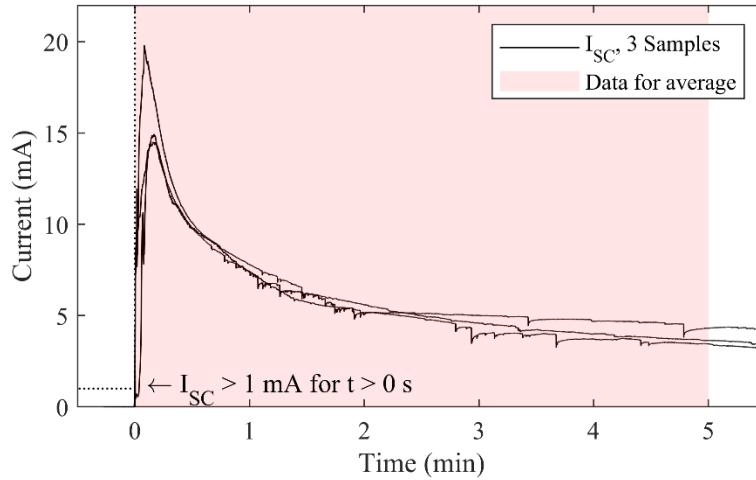


**Figure 11: Unpackaged sensor materials performance in SCC test condition. Window for computing average SCC shown in red. Data is time-shifted such that the sensor response occurs at  $t = 0$  s, where the sensor response event is the first point that SCC exceeds 1 mA**

The maximum and average SCC are calculated for each sample, as well as an average across the samples, shown in Table 4.

**Table 4: SCC performance baseline for unpackaged sensor materials**

Measurement	Sample 1	Sample 2	Sample 3	Average
$\bar{I}_{SC} / (\text{mA})$	5.7	6.2	6.0	6.0
$I_{SC,MAX} / (\text{mA})$	14.5	19.8	14.9	16.4

#### 3.4.4. Constant Current Load Test Performance Baseline

Typical sensor performance, unpackaged, with 0.5 mL of water applied via a pipette, is evaluated for 5 samples over the first 5 minutes of the CC load test with  $I_{CC} = 50 \mu\text{A}$ . Voltage measurements are presented in Figure 12.

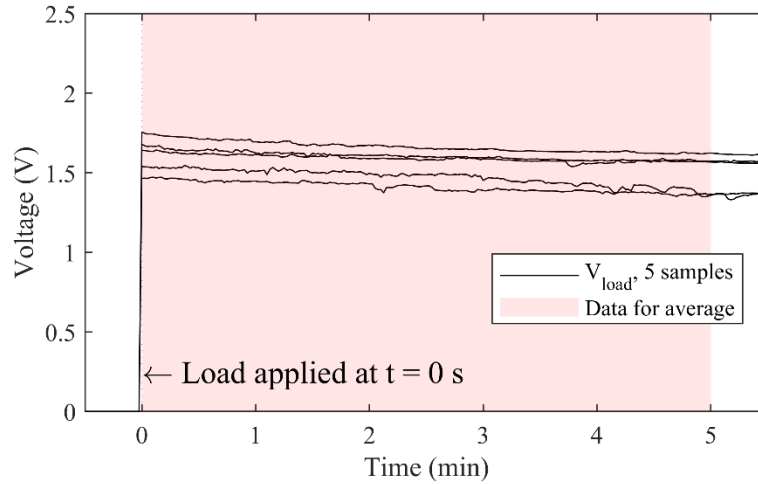


**Figure 12: Unpackaged sensor materials performance in CC Load test condition. Window for computing average  $V_{CC}$  and  $P_{CC}$  shown in red. Data is time-shifted such that the application of the load occurs at  $t = 0$  s.**

The average voltage and power are calculated for each sample, as well as an average across the samples, shown in Table 5.

**Table 5: CC load test performance baseline for unpackaged sensor materials**

Measurement	Sample 1	Sample 2	Sample 3	Sample 4	Sample 5	Average
$\overline{V_{CC}} / (V)$	1.41	1.59	1.66	1.60	1.47	1.55
$\overline{P_{CC}} / (\mu W)$	70.5	79.5	83.2	80.2	73.6	77.4

### 3.4.5. Comments on Evaporation

One factor unaccounted for in the performance of the unpackaged sensor materials versus the packaged sensor materials is the rate of evaporation of the applied water. When water is applied to the unpackaged materials, it evaporates much quicker, since the carbon electrode is exposed to open air. In the packaged materials case, the water is surrounded by plastic on all sides, and the decay of the current output is noticeably slower. For this reason, it is not advisable to compare unpackaged vs packaged sensor performance beyond a short, initial time interval, which is another reason why the 5-minute window used is acceptable for these comparisons.

### 3.5. Packaging Design Considerations

Some observations from the testing of unpackaged sensor materials can help with the design of the sensor packaging.

#### 3.5.1. Pressure Sensitivity

Applying compressive force to the upper surface of the carbon electrode, for example, with a heavy electrical contact seen in Figure 13, will decrease the voltage output of the sensor. This was observed in some cases when preparing experiments with stacked sensor configurations, as was done in [4]. The packaging design was carefully prepared to avoid applying any unnecessary force onto the carbon electrode.

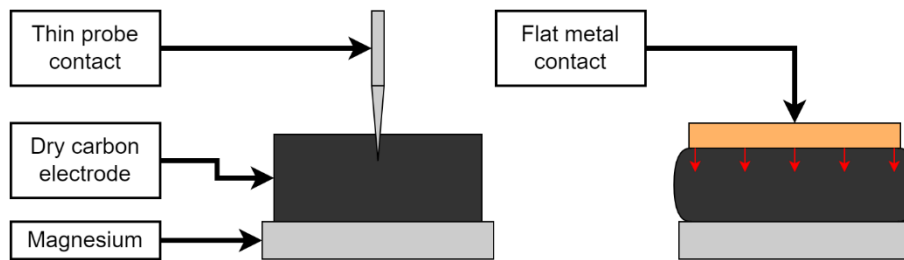


Figure 13: Pressure on carbon electrode may decrease performance

#### 3.5.2. Carbon Electrode Expansion

The dry carbon electrode will expand in volume as well when water is absorbed. Due to this swelling, the space occupied by the electrode increases. One hypothesis was that if the electrode is packaged into an enclosure that restricts this expansion, it could result in a compressive force on the graphite, similar to stress induced by restricted thermal expansion. The result is a lower output voltage when activated by water. The sensor packaging designs are sized larger than the dry electrode to account for this effect.

#### 3.5.3. Probe Insertion Depth Versus Electrical Performance

Another important variable affecting the power output of the sensor is the depth at which the probes were inserted into the carbon electrode during testing. Figure 14 shows the possible variation in the tip depth,  $x$ . The effect of the probe depth is summarized in Table 6. It should be noted however that the observed increase in current with increase in probe depth is likely not due to the depth of the probe itself, but rather the surface area of the probe that is in contact with the carbon electrode. Likewise, if current is affected, then the output power, which is a product of voltage and current, will also be affected. The key takeaway from these observations about the probe insertion depth



are that for a high voltage, the contact should be near the top, and for a high current the contact should have a large surface area.

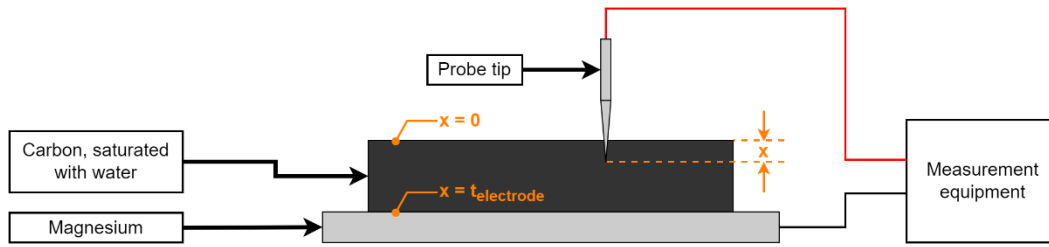


Figure 14: Probe tip insertion depth sensitivity

Table 6: Probe tip conditions and the effect on voltage, current, and power

Probe Depth	Condition	Voltage	Current	Power
$x < 0$	No contact	0	0	0
$x = 0$	Smallest contact area	Maximum	Very small	Small
$0 < x < t_{\text{electrode}}$	Increasing surface area, middle of electrode	Decreasing	Increasing	Maximum
$x \rightarrow t_{\text{electrode}}$	Almost touching magnesium	Very small	Maximum	Small
$x = t_{\text{electrode}}$	Touching magnesium	0	0	0

### 3.5.4. Pre-Cracking of the Carbon Electrode

When dry, the carbon electrodes are very fragile and prone to cracking. Figure 15A shows a crack forming in the graphite electrode when the test probe was being inserted prior to a SCC test. Figure 15B shows a graphite electrode completely broken in half due when handling prior to being assembled into a sensor packaging design. In section 3.5.3, the effect of probe depth and surface area are discussed, and one possible design for the packaged sensor would be a higher surface area probe versus the unpackaged experimental setup. However, the larger probe might not be possible, since the carbon electrode would be more likely to crack if the diameter was increased to improve the surface area in contact with the electrode, as illustrated in Figure 15C.

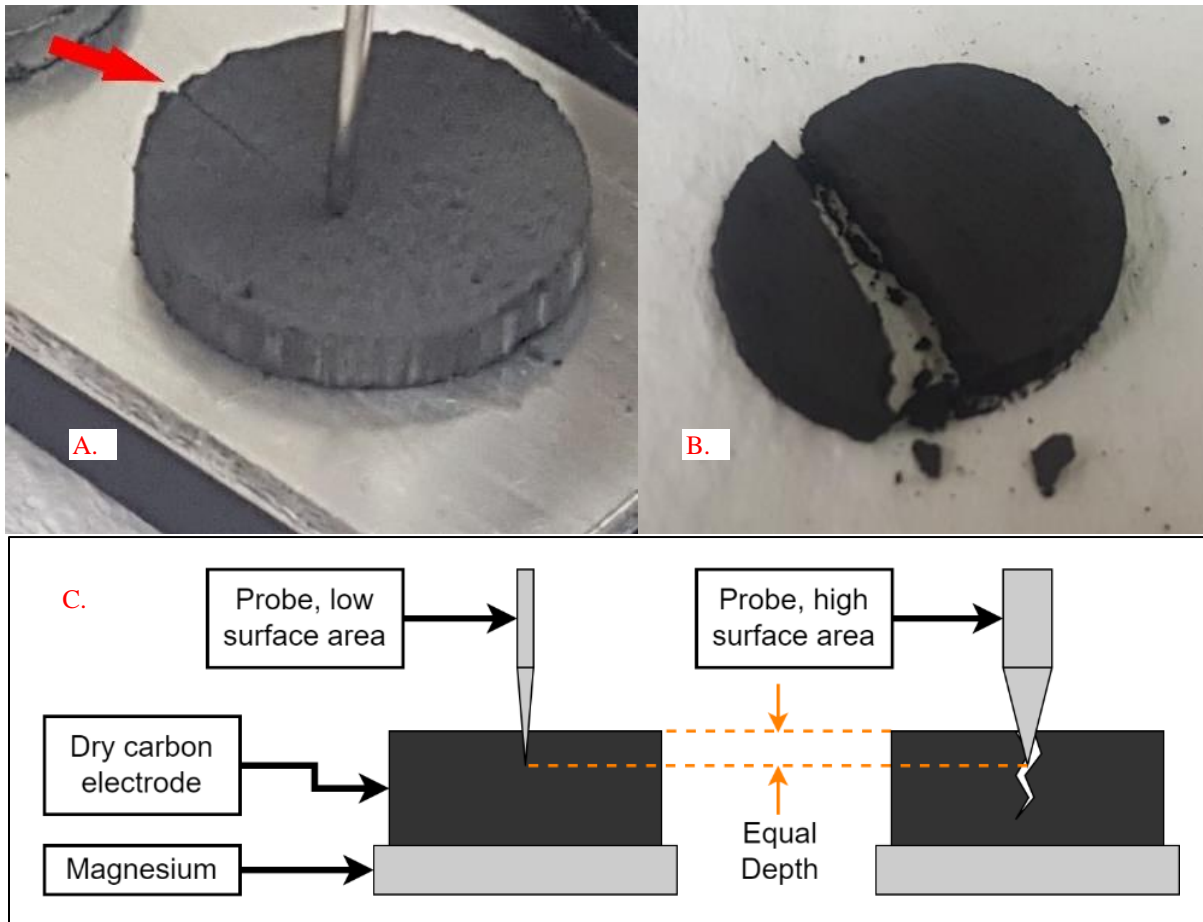


Figure 15: Cracked graphite electrodes A) due to test probe, B) due to handling before assembly into packaging, C) larger surface area probe may aggravate cracking issue in packaging design.

### 3.6. Summary of Chapter 3

The electrical test methods have been presented, and the baseline expected sensor performance is set as a benchmark against which to measure all future sensor performance. Tests to further assess the device as a water leak detector will be used, such as the response time from application of water to wireless transmission. Last, with the packaging design considerations from the previous section, prototyping of a sensor enclosure can begin.

# Chapter 4. Water Leak Sensor Prototype Design

## 4.1. Introduction to Chapter 4

This chapter focuses on the first phase of the water leak detector development, building a prototype model. Prior to this, the sensor materials had only been tested in an exposed form, with the graphite electrode placed on a magnesium sheet. Multiple components of the sensor packaging are developed individually, and then integrated into the first prototype design.

### 4.1.1. Considerations for 3D Printing

The prototyping done in this chapter involves a significant amount of 3D printing, specifically fused deposition modelling (FDM), as shown in Figure 16. FDM is where a model is fabricated layer-by-layer from melted filament., and for this we used the LulzBot TAZ 6 Desktop 3D Printer [63] with nGen filament as the material [64]. The material is selected for ease of use, making it ideal for prototyping. It does not deform as much as ABS but still holds similar mechanical properties, giving easy, high-quality prints. Higher volumes of printing (50 sensors) were outsourced to a manufacturer, for which ABS was selected as the material as printability is not an issue for commercial grade printing shops.

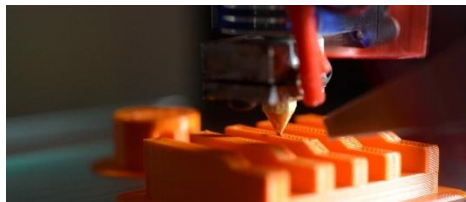


**Figure 16: FDM printer producing a part, image from [65]**

When using FDM some features cannot be easily printed, such as overhangs, thin walls and small holes or boss features. While overhangs are possible with support material (material that can be cut away afterwards), the print quality on the supported face is generally worse. The sensor enclosure is the most critical region of the design, so for these reasons, the enclosure was designed so that none of the faces housing the sensor materials would be supported, which ensures a smoother surface finish. Small holes can easily fill in when printing, changing the diameter significantly, and small walls or bosses will be low quality or extremely fragile. Therefore, the water channel openings, seen in Section 4.3.1, were widened in the computer-aided design (CAD) model to compensate for the size reduction due to printing. The electronics enclosure does not require any support material if the print orientation is selected properly.

## **4.2. Electrical Contact Prototyping**

In the experimental setup (refer to Figure 9, p. 21), a long metal probe contacts the carbon electrode, and the magnesium is connected to an alligator clip. The metal probe is mounted into an adjustable bracket, but the experimental setup is significantly larger than the sensor device itself. The alligator clip on the other hand uses mechanical force to create a low-resistance connection from the magnesium plate to a wire, which is possible since the unpackaged materials magnesium blanks are much larger than the graphite sensors, providing ample space to attach the alligator clips. To develop a water leak sensor, the magnesium piece used is round and only slightly larger than the graphite electrode to save space. Both contact methods used for bare sensor materials are not readily added to an enclosure design, and this is the first problem addressed.

Therefore, electrical contacts for the CNF/graphite electrode and magnesium disc must be developed that are compact and can be assembled into the sensor enclosure. These components were not developed completely independently, although an attempt was made to isolate the effects of each design decision on the sensor enclosure while moving forward. The design of each electrical contact was iterative, and incremental improvements to both were made before reaching a final design for the prototype. The initial designs used CNF, but from section 4.2.4, the electrode is graphite due to the higher current output observed in packaged sensor designs.

### **4.2.1. Probe Tip Imitation Design with CNFs**

In prior work with unpackaged sensor materials, a metal probe, either tungsten or steel, is inserted into the carbon electrode (see Figure 14). A wire is connected to the other end of the metal probe, which is then connected to the DMM or SMU. In the water leak device, an electrical connection between the carbon electrode and the PCB's must be established, similar to the connection between the carbon electrode and the benchtop test equipment. The following sections discuss different designs that were explored to achieve this electrical connection.

The first design tested was meant to replicate the experimental setup used previously. A thin, copper wire was bent 90 degrees, then mounted into a round, 3D printed plastic housing, labeled as the lid in Figure 17. Epoxy is used to secure the wire in place, and the wire is then cut such that it is inserted 0.5 mm into the CNF electrode. Another 3D printed plastic component, the ring, is used to house the CNF electrode. The magnesium is not packaged in the housing, as the goal of this design and these tests is to isolate and evaluate the effectiveness of the CNF contact.

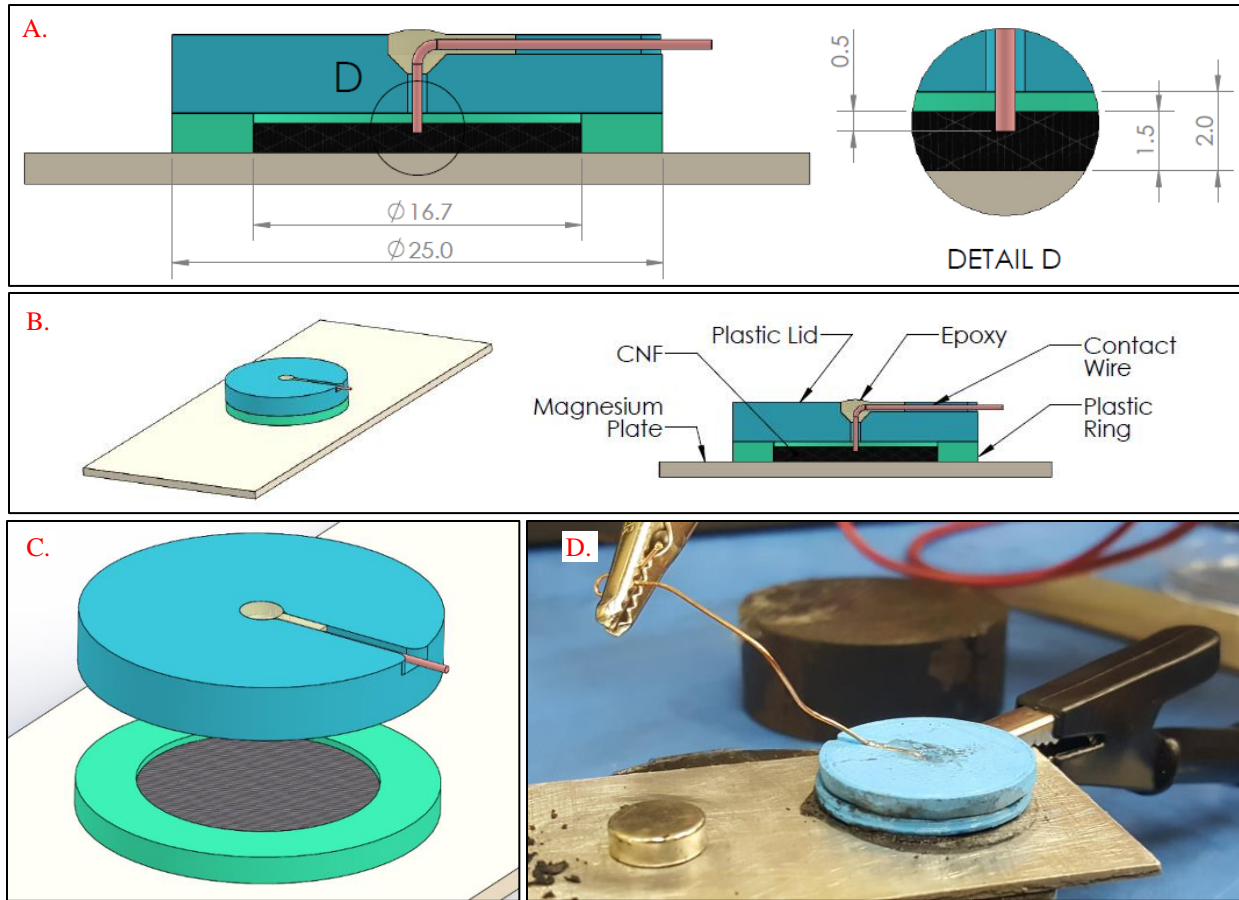


**Figure 17: Probe-tip imitation design. A) CAD model left with components labeled right, B) cross section with dimensions in millimetres, C) lid raised to show CNF electrode, D) Experimental setup to test electrical performance.**

The OCV test and load test were used to assess the probe tip imitation design. The results were comparable to unpackaged sensors, reaching 2 V and remaining stable. Results of the testing are summarized with other contact methods in Table 7. The next step, now that a stable OCV was obtained, was to develop a contact method for the magnesium.

#### **4.2.2. Copper Tape Contact with Mg**

The first method tested is to use a copper tape contact with the back side of the magnesium piece. The copper tape has one adhesive side, and one non-adhesive side. The adhesive is what bonds the tape to the magnesium. A wire is soldered to this copper tape to make connection with the DMM for electrical testing. The copper wire contact for the CNF electrode is used as well in this design, since it had stable voltage performance, but the current performance had not yet been tested.

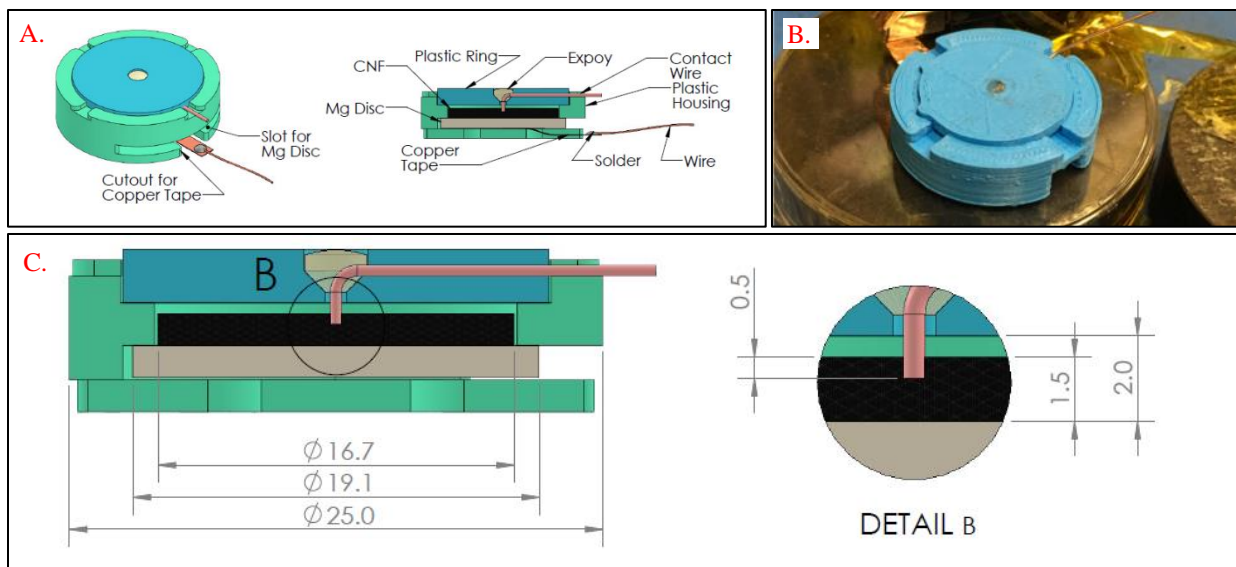


**Figure 18: Copper tape contact design. A) CAD model with labeled components, B) 3D printed, C) cross section with dimensions.**

When tested with water application, the copper tape contact showed mixed results from trial to trial. In some tests, the OCV would fluctuate from expected levels (around 2 V) to low values (0 – 1 V), as seen in Figure 19. The assumption is that the copper tape does not provide a reliable electrical contact, and that the contact resistance between the magnesium disc and tape changes with slight mechanical perturbations. For this reason, a more reliable method of magnesium contact is developed immediately.

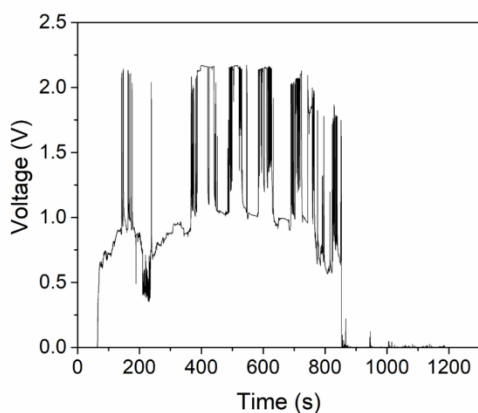


**Figure 19: Unstable OCV performance for copper tape contact<sup>1</sup>**

<sup>1</sup> The testing to obtain this data was a collaborative effort between the author (Levi Johnston) and Ming Xiao. This figure is prepared by Ming Xiao.

### 4.2.3. Spring Contact with Magnesium

The spring contact method of making electrical contact with the magnesium involves an off-the-shelf metal contact that is typically used for mounting AAA batteries, seen in Figure 20. This metal contact is made of stainless steel for the spring functionality, with a tin-nickel plating for electrical conductivity. When the AAA battery is mounted between these spring contacts, the mechanical force of the deflected spring contact creates a low-resistance electrical connection between the spring contact and the battery terminals. In this case, the spring contact is mounted in the sensor packaging at a calculated distance of 2.65 mm from the magnesium plate, to create the same deflection as in the AAA battery case.

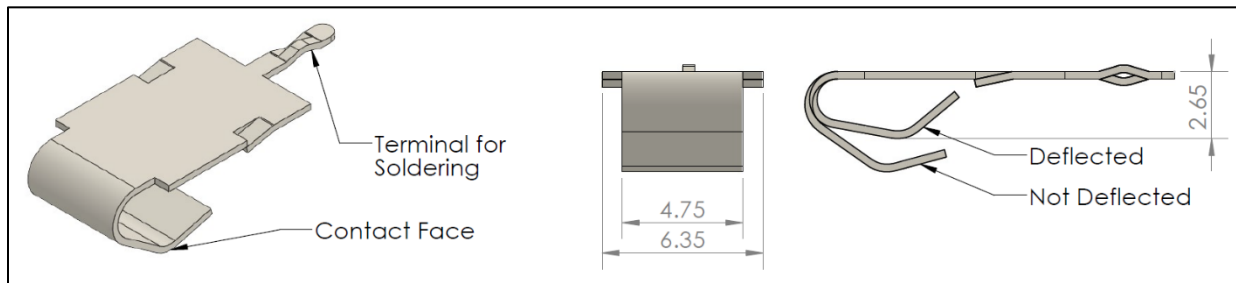


**Figure 20: Spring contact for magnesium, dimensions in millimetres**

To hold the spring contact in place, a cavity slightly larger than the contact is designed into the lid on the magnesium side of the packaging, detailed in Figure 21. The contact is held in this cavity by two small snap features on the sides. The lid is held down to the packaging around the CNF using an annular snap, which prevents the spring clip from pushing the two halves of the plastic packaging apart.

The contact resistance between the battery contact and magnesium disc were tested before any electrical testing was done. With the CNF electrode, wire contact and epoxy removed, the first probe of a handheld multimeter was inserted towards the magnesium, while the other was held to the wire soldered to the spring contact. This measured the contact resistance in series with the resistance of the magnesium disc, the wire, and the solder. The resistance of the series of components was  $< 1 \Omega$ . The plate resistance and soldered wire resistance were measured separately and are negligible ( $R < 0.1 \Omega$ ), meaning the contact resistance between the spring and magnesium plate was acceptable. The resistance also did not fluctuate with any shaking or movement of the packaging, whereas with the copper tape and silver paste attempts, this was not the case. To put this  $1 \Omega$  measurement into context, the internal resistance of the CNF-Mg sensor design was

measured at 2.7 k $\Omega$ , so this series resistance would only increase the total by  $\Delta = 0.04\%$ , where

$$\Delta = (R_{\text{internal},2} - R_{\text{internal},1})/R_{\text{internal},1}$$

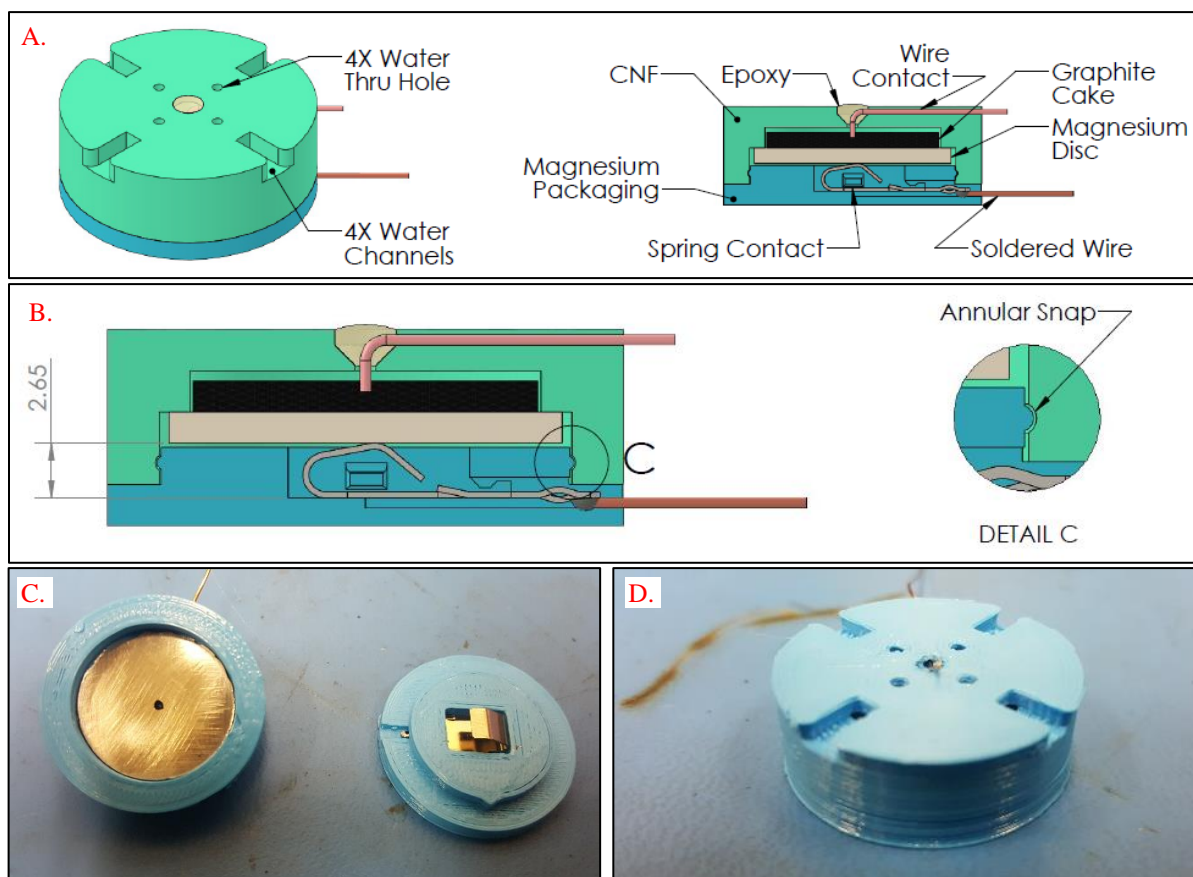


**Figure 21: Spring clip design. A) Components of sensor packaging labeled, B) cross section with spring contact distance to magnesium disc and annular snap, C) 3D Printed version showing disassembled lid and packaging with spring contact, D) assembled packaging, with CNF side upwards showing water-intake features.**

After confirming the contact resistance was acceptable, the OCV and SCC tests were done, shown in Figure 22. First, the OCV test gave good results, with the OCV measured staying in the range of (1.7 to 2.1) V. Compared with the unstable measurement seen in 4.2.2, this is a significant improvement. Next, the SCC was tested, however the output dropped to around 200  $\mu\text{A}$  after reaching a maximum of only 450  $\mu\text{A}$ . This is significantly lower than expected for the CNF-based sensor design, where SCC in the unpackaged test stabilize in the range of (1 to 2) mA [3]. This is the first time SCC was tested for the packaging prototypes, so it is possible the low current could be due to the carbon electrode's probe contact, the magnesium disc's spring contact, or the packaging around the CNF electrode. The depth of the copper wire used in this contact method was very difficult to control, and this played a role in the surface area exposed to the CNF



electrode. Slight variations in amount of water, probe depth, assembly force between the packaging halves, and CNF thickness would significantly change the power output.

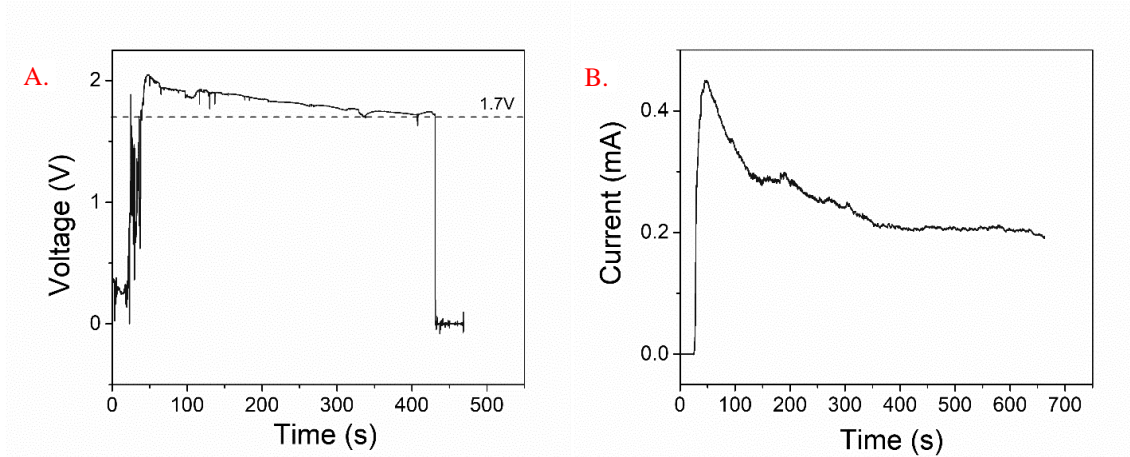


**Figure 22: Testing packaging design, probe contact for CNFs, spring contact for Mg. A) OCV test results, B) SCC test results<sup>2</sup>**

The suspected reason for poor SCC performance is that the CNF electrode probe contact area was a lot smaller in the packaged design than in the unpackaged materials design. In addition, there is a discrepancy not accounted for in how the contact is applied in the unpackaged materials design versus the packaged materials. In the unpackaged materials setup, the water is first applied to the CNF electrode, and then the probe is lowered into the CNF to make electrical contact. For the packaged sensor, the wire contact is inserted into the CNF electrode when the packaging is assembled, meaning the CNF electrode is still dry. In fact, this means the CNF electrode is still quite brittle, and in unpackaged sensor materials tests, a common occurrence is the CNF electrode cracking when the probe is applied before the water. This was not initially considered in the wire contact design for the sensor packaging. Although the OCV of the sensor was acceptable, the cracking in the CNF electrode could have caused the significant reduction in current output.

#### **4.2.4. Change to Graphite and Enclosure Resizing**

The current output when using CNF electrodes in enclosure designs was quite poor, which was assumed to be due to the probe tip design. However, a graphite electrode, when used in place of the CNF electrode, with the same packaging as in section 4.2.3 produced considerably higher current output after correcting the graphite electrode thickness to match the enclosure size. While

---

<sup>2</sup> The testing to obtain this data (plots A and B) was a collaborative effort between the author (Levi Johnston) and Ming Xiao. This figure is prepared by Ming Xiao.

the SCC with CNF peaked at  $\sim 450 \mu\text{A}$  and averaged  $200 \mu\text{A}$  to  $250 \mu\text{A}$ , the graphite design reached an average peak value of  $6.53 \text{ mA}$ , and averaged  $3.5 \text{ mA}$  across two samples, which is more than 10 times larger. The design iterations going forward use the graphite electrodes.

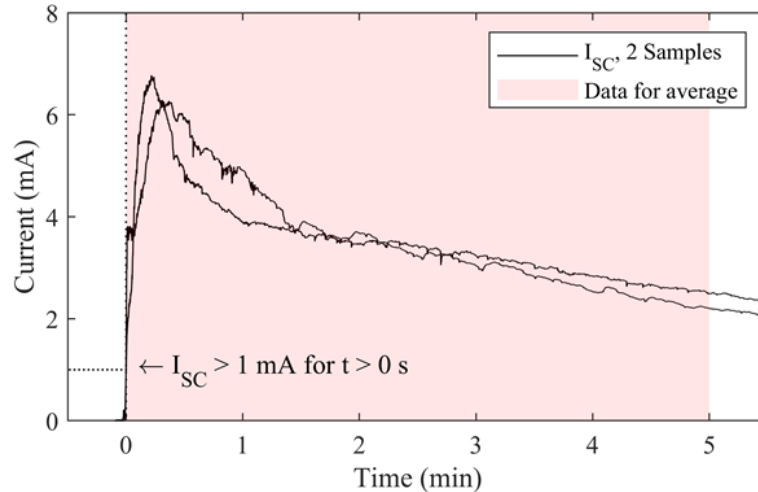


**Figure 23: SCC current test for graphite replacement. Average peak current was  $6.53 \text{ mA}$  and average across 5 mins was  $3.54 \text{ mA}$ .**

#### 4.2.5. Conductive Washer Contact

To increase the contact surface area, a thin, conductive, off-the-shelf washer was selected as the contact element, made from copper with a nickel plating was used to replace the probe imitation design. This washer was selected since the nickel plating can be more easily soldered to than a standard steel washer. In addition, the high ratio of washer outer diameter to washer thickness is difficult to find in standard mechanical off-the-shelf washers, which is partially what makes this a specialized component. The reason the very small thickness was used was to keep the graphite electrode as close to the bottom of the packaging as possible, to maximize the sensitivity of the water leak detector. Drawings of the washer contact design are shown in Figure 24. To evaluate the washer design, the SCC test was done a second time to compare to the probe-tip based design, shown in Figure 25.

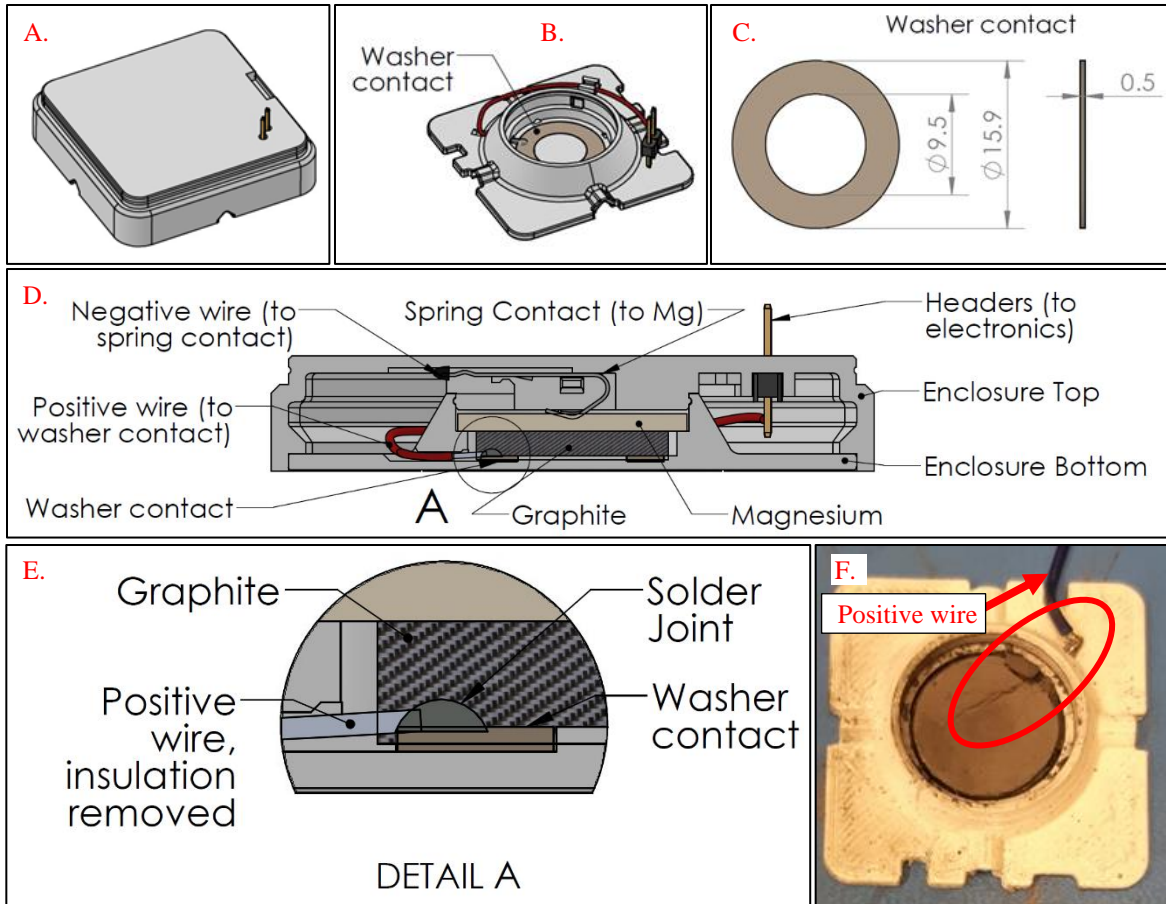


Figure 24: Copper nickel-plated washer contact in modified enclosure design. A) Complete enclosure, B) enclosure with some components hidden to show washer contact location, C) washer dimensions, washer manufactured by Switchcraft [66], D) cross section view with washer contact and sensor materials, E) detail view of solder joint location below graphite electrode, F) graphite electrode cracking above solder joint.

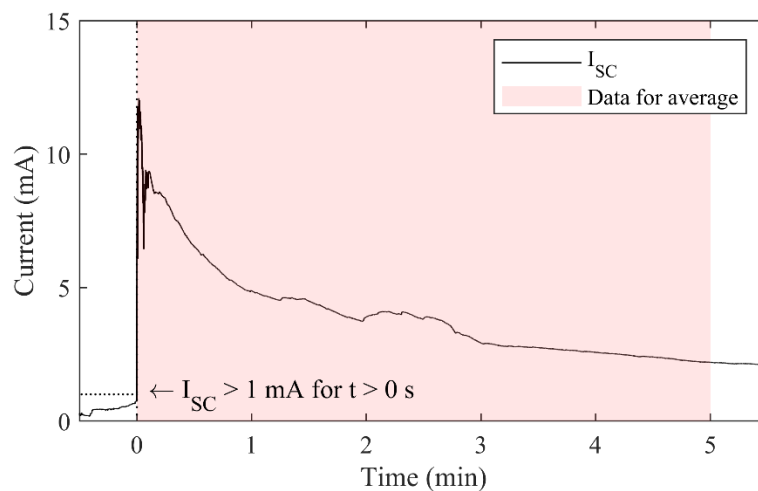


Figure 25: SCC test for washer contact design. Peak current was 12.1 mA, and the 5-minute average was 4.0 mA.

Comparing Figure 23 to Figure 25, the SCC was improved again, with a peak of 12.1 mA, which is almost twice that of the probe tip design with a peak of 6.53 mA. The average current was increased only slightly, up to 4.0 mA versus 3.5 mA previously. There were several drawbacks to the conductive washer however, despite the improved electrical performance, two of which are shown in Figure 24. First, it was difficult to solder a wire to the washer without creating an uneven thickness below the graphite electrode. The solder ball and the wire would create a sharp, raised feature below the graphite electrode, which would often cause it to crack on assembly. Second, the washer was difficult to keep fixed in place. Since it was round, and matched the size of the graphite electrode, the mounting options were limited to adhesives, which are difficult to select for bonding metal to a 3D printed enclosure in a moist environment, and press fits, which were hard to achieve with 3D print quality and a very thin washer. The latter was used, however the press fit often failed to retain the washer and it would pop out of position, displacing the graphite electrode. Lastly, the relative price of the washer was high since it is not a standard washer size or material. These issues are resolved by the next iteration of the contact design, while maintaining the performance.

#### **4.2.6. Solder Terminal Lug Contact**

The solder terminal lug is a thin metal component, easily soldered to, meant to join wires to a screw-down terminal. The solder terminal lug contact design shown in Figure 26 is quite similar in principle to the thin washer contact. The contact offers a large surface area to improve upon the probe tip design and can be mounted at the maximum distance from the magnesium surface. Where it differs compared to the conductive washer, is that it can be mounted in a way such that part of the contact is exposed, while the other portion, used for soldering a wire, is not beneath the graphite. This solves two problems from the washer design, the solder point causing cracking in the graphite, and the retention of the contact, since it can be inserted through a horizontal slot, seen in Figure 26.

Here, the results of the SCC test with the solder terminal lug contact are presented along with the SCC test results from the previous two sections in Figure 27. The solder terminal lug contact had the lowest peak current value, at only 5.16 mA, and showed a much slower response to water. The ring terminal and probe tip designs were radially symmetric; however, this contact's area is in a single quadrant of the graphite electrode's circular profile. If water must migrate from one portion of the electrode to the other due to non-uniform absorption, the current would not rise as rapidly.

Despite the low initial current, the average current was the highest yet, at 4.58 mA, which suggests this contact design is the most effective for a stable sensor output.

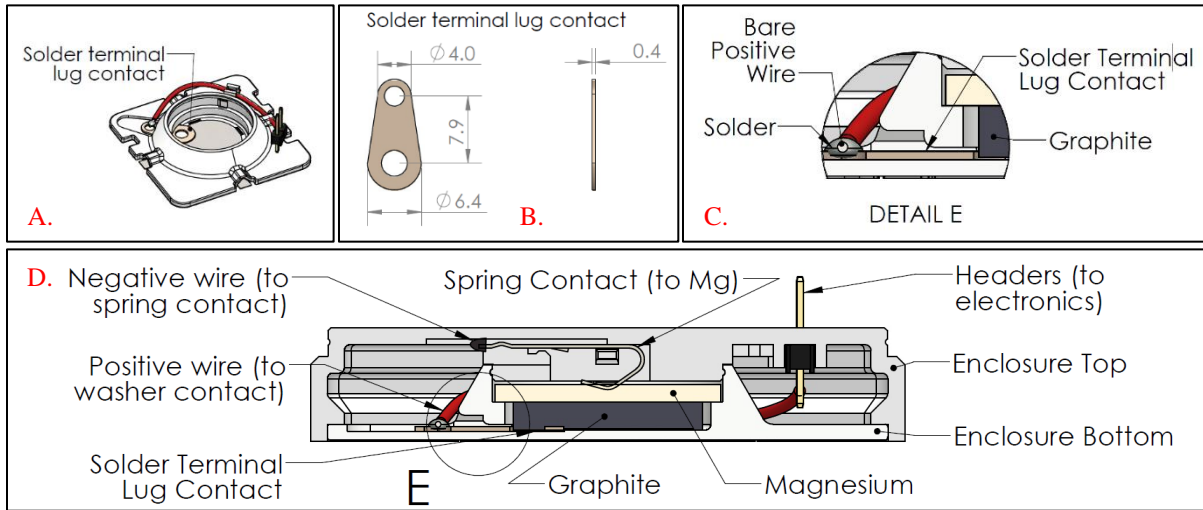


**Figure 26: Solder terminal lug contact design. A) Enclosure with some components hidden to show solder terminal lug contact location, B) Solder terminal lug contact dimensions, C) detail view of solder joint location, which is no longer below the graphite electrode, D) cross section view with washer contact and sensor materials.**

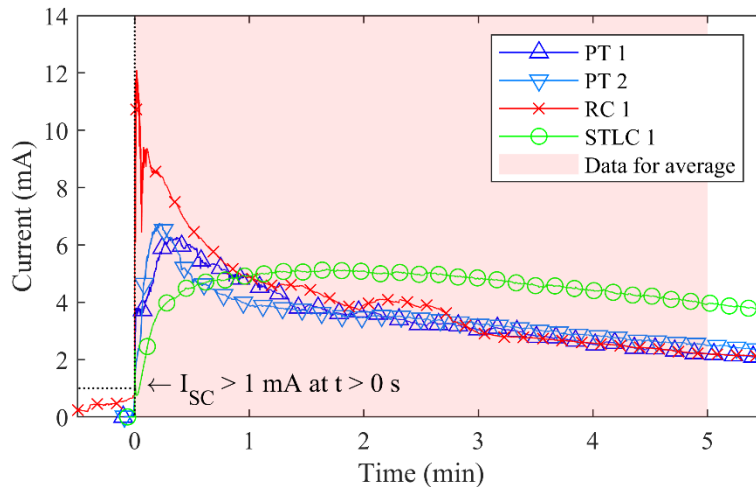


**Figure 27: SCC test for solder terminal lug contact design compared with other graphite contact methods. Peak current was 5.16 mA and average was 4.58 mA. PT = Probe tip design, RC = Ring contact design, STLC = Solder terminal lug contact design. The STLC design had the lowest peak but highest average current.**

### 4.2.7. Summary of Contact Performance Improvements

The comparison between all three contact methods and with the unpackaged sensor materials is given in Table 7. The ring terminal and solder terminal lug are the most effective for a high SCC. The solder terminal lug is selected for future use since it is the lowest cost, and as previously discussed, does not crack the graphite electrode upon assembly.

**Table 7: Comparison of graphite electrical contact methods by electrical performance testing**

Sensor Configuration			Test Name and Measurement	
Sensor Material (Carbon, Mg)	Contact Designs (Carbon, Mg)	Section or Reference	OCV $\overline{V}_{OC} / (V)$	SCC $\overline{I}_{SC} / (mA)$
CNF disc, Mg plate	Unpackaged Baseline	Reference [3]	Up to 2.65	1.0 to 2.0
CNF disc, Mg disc	C: Wire, Mg: Alligator	Section 4.2.1	2.0	-
CNF disc, Mg disc	C: Wire, Mg: Copper tape	Section 0	Unstable, 0.5 to 2.1	-
CNF disc, Mg disc	C: Wire, Mg: Spring contact	Section 4.2.3	1.9	0.2 to 0.25
Graphite disc, Mg plate	Unpackaged Baseline	Section 3.4	1.8	6.0
Graphite disc, Mg disc	C: Wire, Mg: Spring contact	Section 4.2.4	-	3.5
Graphite disc, Mg disc	C: Washer, Mg: Spring contact	Section 4.2.5	-	4.0
Graphite disc, Mg disc	C: Solder term. lug, Mg: Spring contact	Section 4.2.6	-	4.6

## 4.3. Water Absorption Methods

### 4.3.1. Water Channels

The graphite electrode must simultaneously be enclosed by the packaging to protect from damage, but also be exposed to the water from the water leak to be detected. For this reason, small openings, referred to as water channels, are designed into the packaging, which allow water to reach the graphite electrode. Several different variations of these water channels were tested by placing a graphite electrode in the packaging without magnesium, and with the lid removed. Then by adding the enclosure to water, the absorption could be observed. The observations are summarized in Table 8, and the hybrid design was selected. Images of the enclosure with the hybrid water channel design are given in Figure 28. For the hybrid design, water uptake occurred in under 5 seconds.

**Table 8: Design considerations for water channel layout. A design hybrid between side and bottom channels is optimal. See Figure 28 for concept images of designs.**

Design Type	Absorption Rate	Sensitivity	Barrier Design	Figure Reference
Side	Fast	Low	Difficult	Figure 28, A1
Bottom	Slow	Moderate	Easy	Figure 28, A2
Side-bottom	Moderate	High	Easy	Figure 28, A3

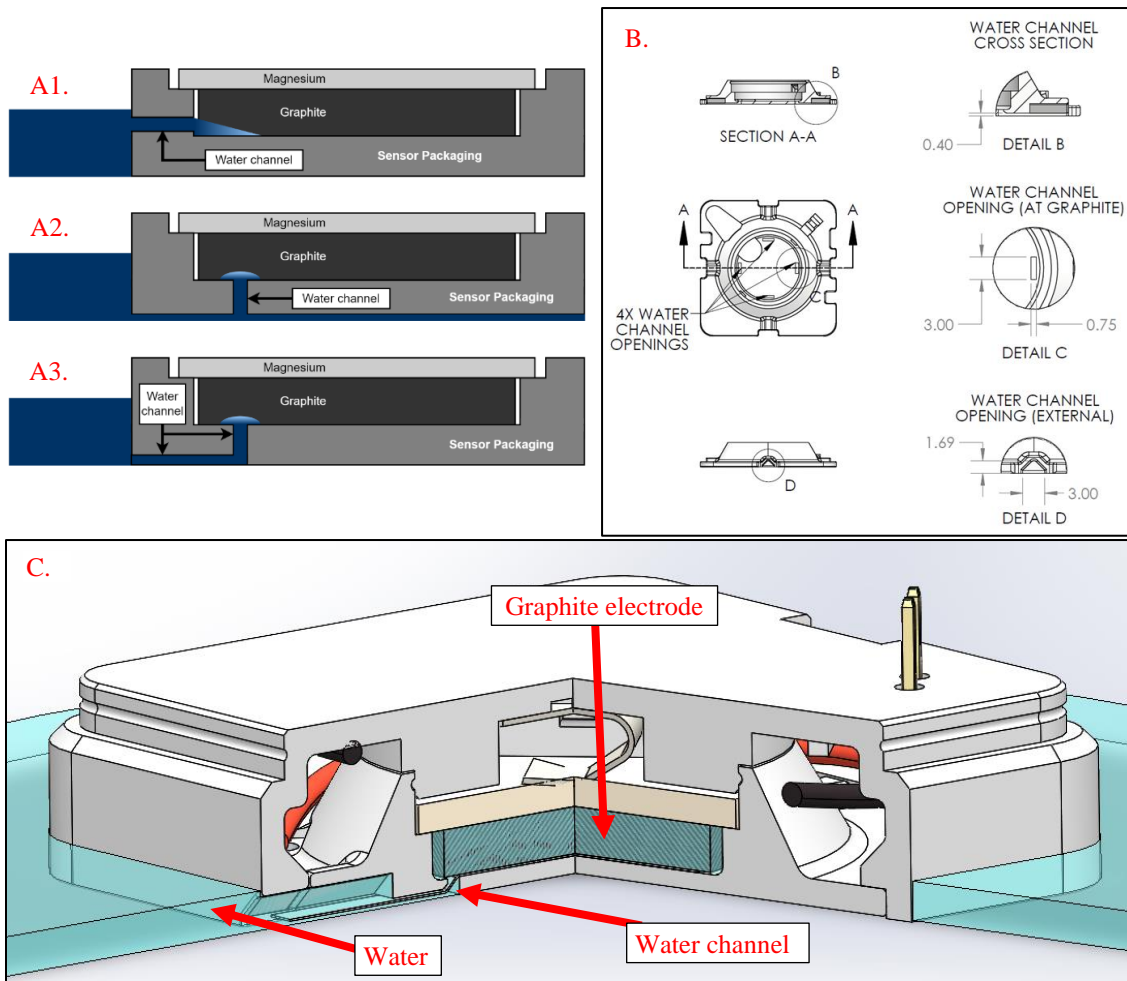


**Figure 28: Water channels for sensor materials packaging. A) Design variations, B) Drawing with dimensions in millimetres, C) CAD model with cut-out section view**

### 4.3.2. Wicking Tails

The water channels designed into the sensor packaging allow water to flow if there is a sufficient pressure gradient. In addition, for smaller water channels, the capillary effect can play a role, either aiding or resisting the flow of water, depending on if the packaging material is hydrophilic or hydrophobic. To respond to leaks faster and increase the device sensitivity, an additional design

element added was wicking tails. These thin paper pieces rely on the capillary effect to draw water towards the graphite electrode, allowing the sensor to become saturated more readily when water pools on a surface near the sensor [67].

An initial test was done using filter paper pieces cut from larger stock, as shown in Figure 29. Strips of this paper, 20 mm long and 3 mm wide were placed partially below the graphite electrode such that 10 mm remained exposed. The test was done in a petri dish, which is hydrophobic. Next, 0.5 mL of water is applied at the tip of the paper using a pipette. The graphite electrode is saturated almost instantly, and a response time could not be measured. The paper aided in this increased water uptake, but it is also important to note the hydrophobic nature of the surface material aids the test result. A hydrophilic surface would instead help the water to disperse, potentially away from the electrode material. Either way, the initial test demonstrates the design concept of adding these wicking tails to the sensor packaging.

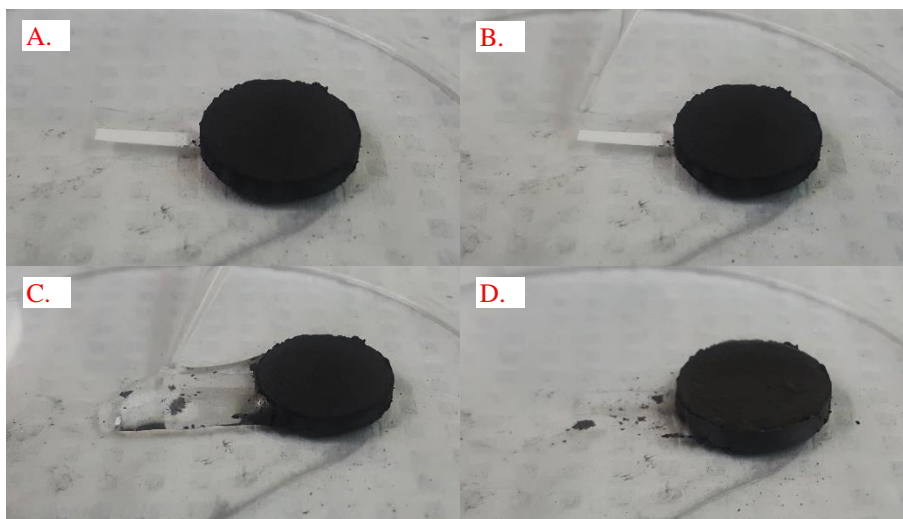


**Figure 29: Paper wicking tail test, paper tail extends 10 mm beyond edge of graphite electrode. A) test setup, graphite electrode on paper, B) pipette in frame, C) application of water with pipette at end of tail, water rapidly moves towards graphite electrode along paper tail, D) majority of water absorbed by graphite electrode.**

Next, a pattern was created for the wicking tails such that a single piece could be assembled into the sensor packaging when folded and rolled correctly. Figure 30 shows this first design, where the paper is first rolled along the diameter of the graphite enclosure, and the tails are then inserted through the water channels. The component was laser cut to the specified shape.



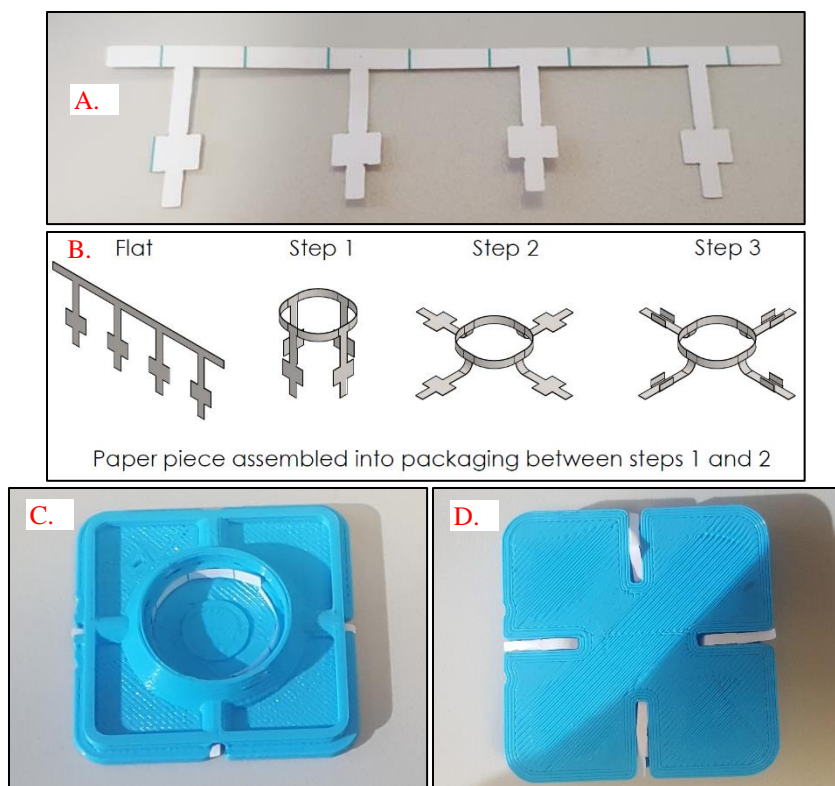


**Figure 30: Wicking tails first design for packaging, A) Wicking tails laser cut from printer paper to test fit, B) Folding pattern for assembly, C) Wicking tails assembled into packaging, top view D) bottom view**

Testing with this first design in Figure 30 failed to properly absorb water at depths below 2 mm. The paper design was improved by implementing the following changes, which can be seen in Figure 31. First, the shape was split into three pieces to make production easier, since the first laser cut pattern was very complex and tedious to cut by hand, and laser cutting was not readily available in the lab. It now consists of two long strips (the tails), and a central,  $\frac{3}{4}$ -circle shape, which is quicker to make for prototyping. The  $\frac{3}{4}$  circle is to not cover the solder terminal lug contact, as the filter paper is an electrical insulator. In future versions, alternate cutting methods can be used to produce the single-piece filter paper again. In addition, the graphite did not easily absorb the water from the ring piece at its circumference, which is the reason for using the  $\frac{3}{4}$ -circle piece. With the graphite electrode resting directly upon a much larger paper piece, the water is transferred more easily between the two materials.

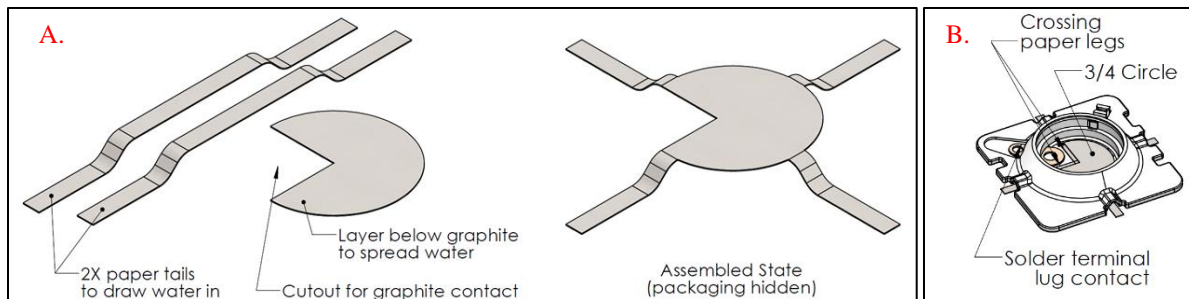


**Figure 31: Filter paper tails redesign. A) paper pieces used in second design, B) image of packaging with second design in place**

## 4.4. Complete Sensor Unit Design

After prototyping the compartment which houses the sensing materials, the remainder of the packaging design was very straightforward. The enclosure beyond the materials location must simply contain the PCBs needed for the water leak device and complete the electrical connections between the sensor materials and the PCBs. One important design decision to discuss first is that separate housings were designed for the sensor materials and PCBs. Since the sensor materials are limited use and low cost, whereas the PCBs are high cost and can be used indefinitely, the sensor enclosure is easily removable from the electronics enclosure. This way it can be replaced at the end of its lifespan. First, the subassemblies of the leak detector are presented: the sensor enclosure (section 4.4.1) and the electronics enclosure (section 4.4.2), then the full assembly (section 4.4.3).

### 4.4.1. Sensor Enclosure

First, the sensor enclosure is designed to house the sensor materials and deliver power to the electronics. It incorporates all the design elements developed in the previous sections of this chapter, including the graphite contact, graphite cavity size, magnesium contact, water channels, and filter paper pieces, shown in Figure 32. The packaging is changed to a square shape to match the PCB shapes, since the PCBs are stacked directly above the sensor materials in the complete unit design. Wires are soldered to the metal contacts used for the magnesium and graphite, and then soldered again to a header pin, part 4 Figure 32, which connects to the electronics. The annular snap between the top and bottom 3D printed parts, items 1 and 9 respectively, holds the enclosure shut. The filter paper pieces, number 8 in Figure 32 are fed through the water channel openings on the graphite side.

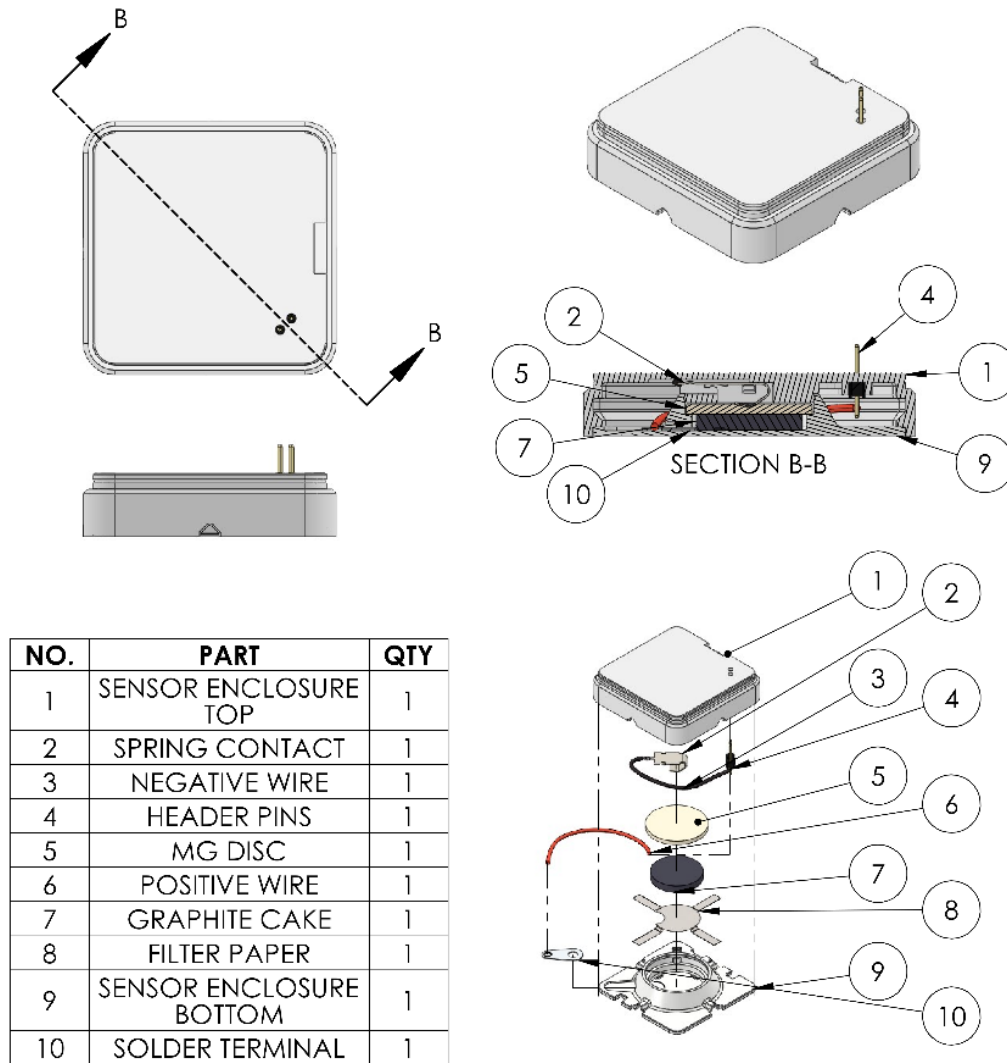


**Figure 32: Drawing of sensor materials enclosure design**

#### 4.4.2. Electronics Enclosure

The enclosure for the PCBs is straightforward, shown in Figure 33. The PCBs (parts 3 and 5) mate together with a set of headers, then a screw, round spacer, and hex nut (parts 2, 4 and 9) are used to mount both to a 3D printed platform (part 10). Another header (part 8) connects to the sensor enclosure header pins and is wired to the energy harvesting board.

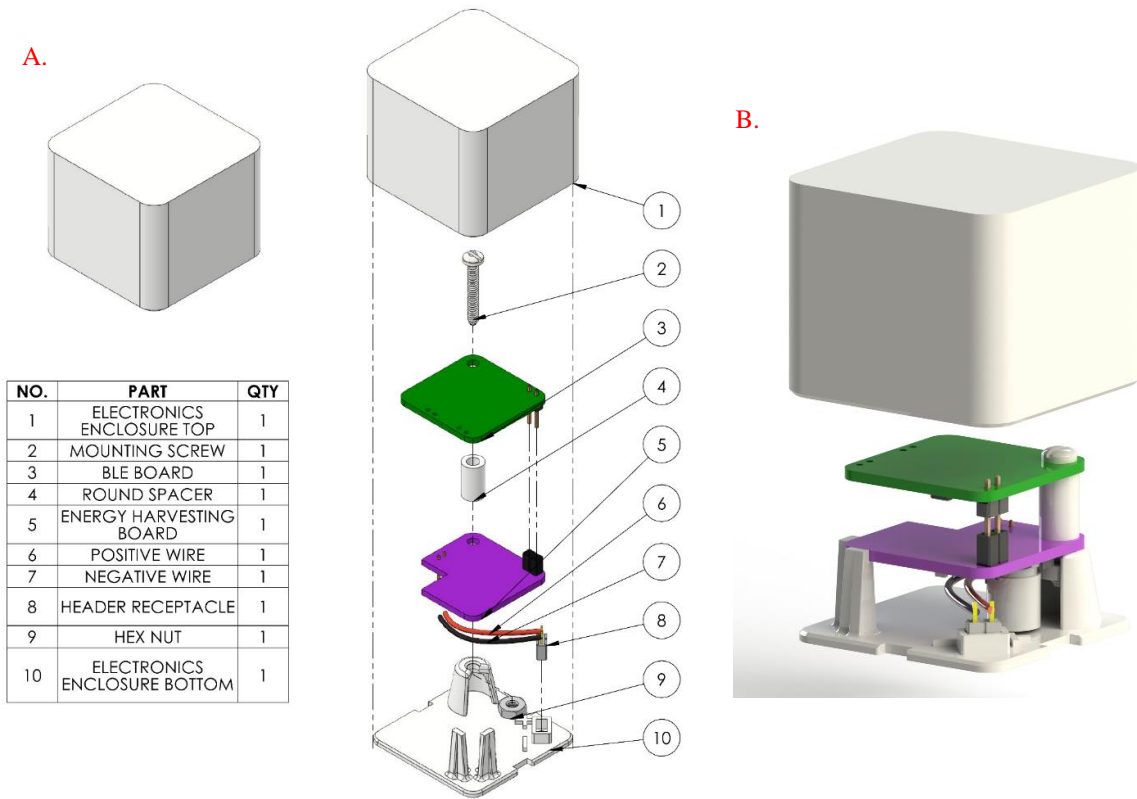


Figure 33: Electronics enclosure design. A) exploded view of electronics packaging, B) assembled with lid raised

#### 4.4.3. Complete Leak Detector

Some options were considered briefly for the entire system layout. The BLE and the EH PCBs (see Appendix B for more details), can either be assembled beside one another, or stacked vertically. In addition, the sensor materials can be placed below the PCBs, or to the side. Some possible design combinations are seen in Figure 34.

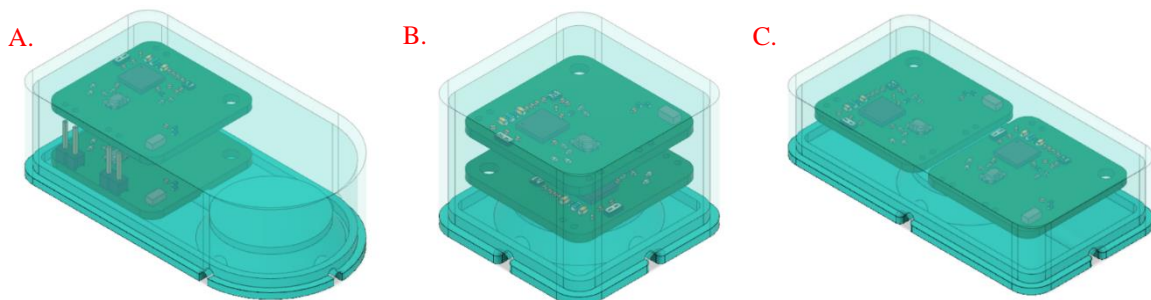
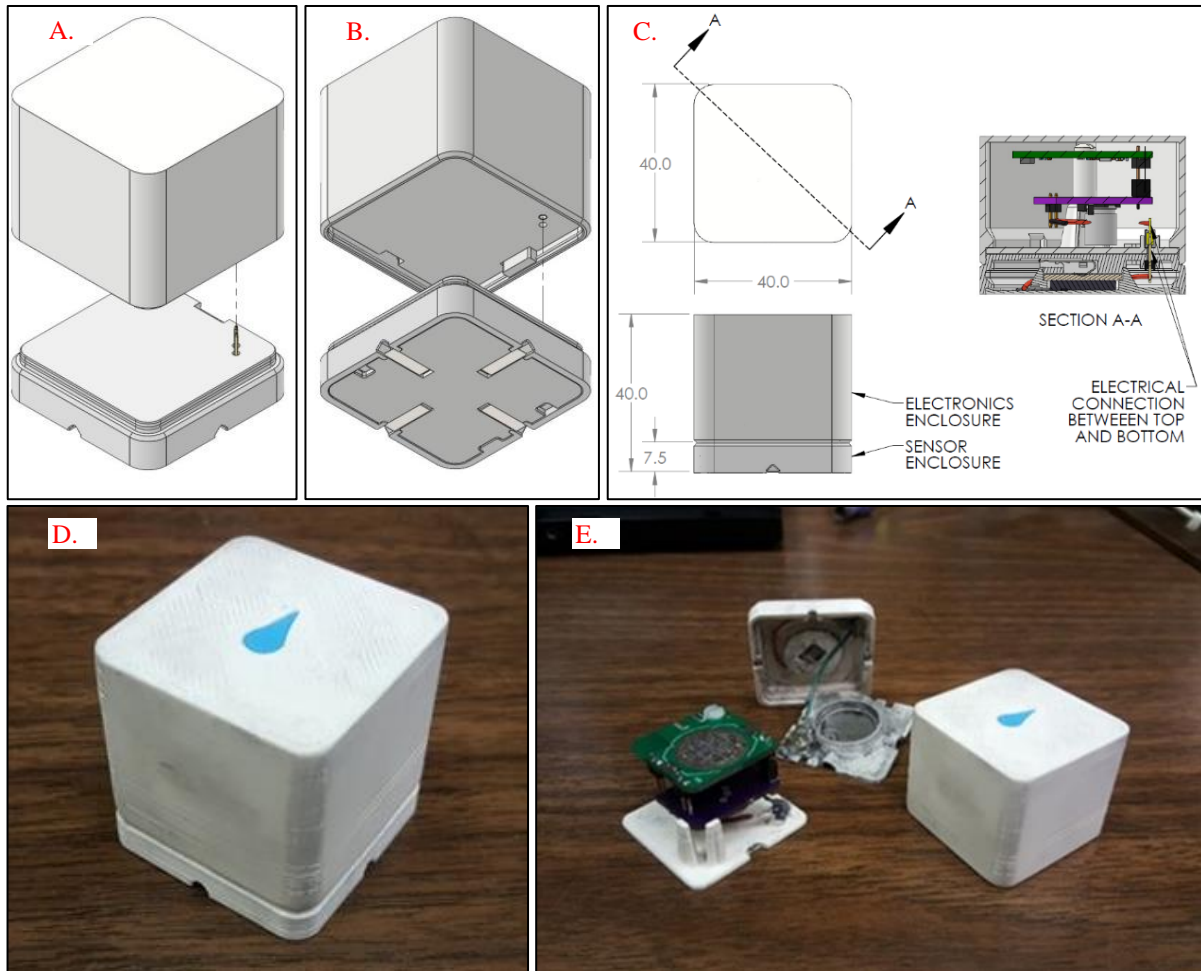


Figure 34: Design alternatives for the complete water leak detector design. A) PCBs stacked, sensor to the side, B) everything stacked, C) PCB's side by side, sensor below.

The fully stacked design (B) was selected for its horizontal compactness, and ease of mounting the two PCBs to one another. The first 3D printed water leak detector prototype is shown in Figure 35. The sensor enclosure and the electronics enclosure attach with an annular snap fit around the rectangular profile.



**Figure 35: Complete water leak packaging design for 3D printing. A) Top isometric view, showing pins on sensor packaging, B) Bottom isometric view, showing holes on electronics packaging, C) section view showing assembled leak detector unit interior. D) 3D printed assembly, E) lid removed to show electronics, and sensor enclosure opened to show graphite, Mg disc not shown**

## 4.5. 3D Printed Version Evaluation

The complete sensor unit design was outlined in the previous sections. In this section, the 3D printed design is evaluated in several ways.

### 4.5.1. First Complete System Test

Finally, after integrating all the sensor materials, electrical connectors, and PCBs into a single water leak detector unit, a test of the complete system can be done to evaluate the performance of the device. The beacon activation test is used, with the leak detector shown in Figure 36, since it evaluates the complete water leak detector in response to a simulated water leak event. Into the petri dish, 1 mL of water was added, and then the sensor was placed into this droplet. For future tests, the water depth is controlled as outlined in Chapter 3, however these trials were a quick verification that the integration of all the design elements and electronics was successful. In the first successful trial, the BLE beacon was activated in 30 seconds, and in the second, the activation time was 75 seconds. This is considered a successful result, simply because the water leak detector activated, regardless of the activation time. This confirms that the complete water leak detector system can generate the desired BLE output in the event of a water leak. The enclosure still requires further evaluation to determine the performance quality, as even the initial two tests gave significantly different activation times.

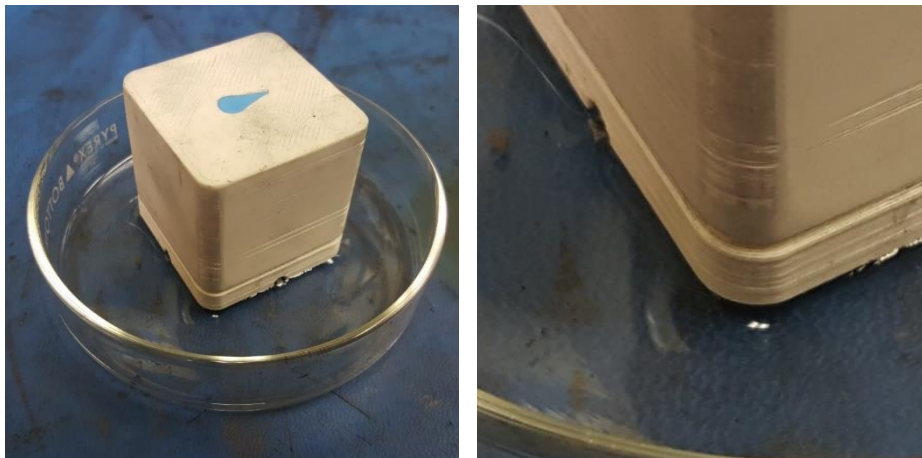


Figure 36: Simulated water leak in petri dish with first complete water leak detector prototype

### 4.5.2. Yield Rate and Multiple Use Testing

The next course of action following the first successful trials is to verify the reliability of the water leak detector units, so the yield rate for a larger sample size is the evident next step. Sensors were

prepared in 3 batches of 6 devices, but all subjected to the same test, as outlined in section 3.3.2. The sensors are added to a petri dish with water, and the outcome of “Pass” is achieved for an activation time under 5 minutes. Samples that passed the first time were left to dry for 24 h, and the test was repeated.

**Table 9: Yield rate and multiple use testing for first sensor prototype. After failure, test was not repeated, and is left blank intentionally. Yield rates are given relative to the first trial (18 samples) and relative to the number of samples that passed the previous trial.**

Batch Number	Sample Number	Outcome by trial number (PASS/FAIL)			
		1	2	3	4
1	1	PASS	PASS	PASS	FAIL
	2	PASS	PASS	PASS	FAIL
	3	PASS	PASS	PASS	FAIL
	4	FAIL			
	5	FAIL			
	6	FAIL			
2	7	PASS	PASS	PASS	FAIL
	8	PASS	PASS	PASS	FAIL
	9	FAIL			
	10	FAIL			
	11	FAIL			
	12	FAIL			
3	13	PASS	PASS	FAIL	
	14	PASS	PASS	FAIL	
	15	FAIL			
	16	FAIL			
	17	FAIL			
	18	FAIL			
<b>Yield rate, from trial 1</b>	<b>Fraction</b>	7/18	7/18	5/18	0/18
	<b>Percent</b>	38.9	38.9	27.8	0.0
<b>Yield rate, from prev. trial</b>	<b>Fraction</b>	7/18	7/7	5/7	0/5
	<b>Percent</b>	38.9	100.0	71.4	0.0

The yield rate at this point was quite low when the sensors were produced in volume. Of the 18 samples tested, only 7 were functional on the first trial, which is 39%. Evidently this is not an acceptable value for a water leak sensor, even at prototype stage. Ultimately, manufacturing

variations are the primary difference between samples. To alleviate low yield on the first trial, the manufacturing controls can be tightened to produce more similar parts each time, or the design can be adjusted to be less sensitive to manufacturing variations.

Additional analysis of the yield rate from trial-to-trial shows that of the sensors that passed trial 1, all passed trial 2, and 71% passed trial 3. This suggests a post-assembly step involving one simulated leak event could be used to verify the device was manufactured properly. However, after trial 3, the yield rate was 0% for trial 4. This suggests a decay in sensor performance dependant on to the exposure time to water, the number of water exposure events, or most likely, both.

#### **4.5.3. Filter Paper Barrier Modification**

After the low yield rate results were obtained for the sensor prototype, a significant improvement to the sensor structure was suggested by fellow students who developed the original sensor materials designs in [3] and [4]. The design up to this point had been a layered sensor with magnesium, then graphite, then filter paper. Instead, a new design was proposed and evaluated, where an additional paper barrier was inserted between the graphite electrode and the magnesium plate. This significantly improved the reliability of the sensor performance, as seen in the higher yield rates of subsequent tests. Going forward, this additional filter paper barrier is used for all assemblies. The suggested reasoning as to why this improved the yield rate is later discussed in more detail in section 4.6.2. In summary, the barrier prevents a short-circuit between electrodes when the graphite is only partially saturated. Another theoretical benefit is that the filter paper better distributes water across the magnesium surface, increasing the area of the reaction, but this was not confirmed through additional testing. An updated CAD model is shown in Figure 37, showing the addition of the circular filter paper barrier between the Mg disc and the graphite electrode. This paper barrier has a diameter of 21.5 mm, which is slightly larger than the 18.65 mm of the Mg, which results in the paper barrier wrapping up around the outside edge of the metal disc when compressed in the packaging. This is quite effective in preventing direct contact between the graphite and Mg electrodes.



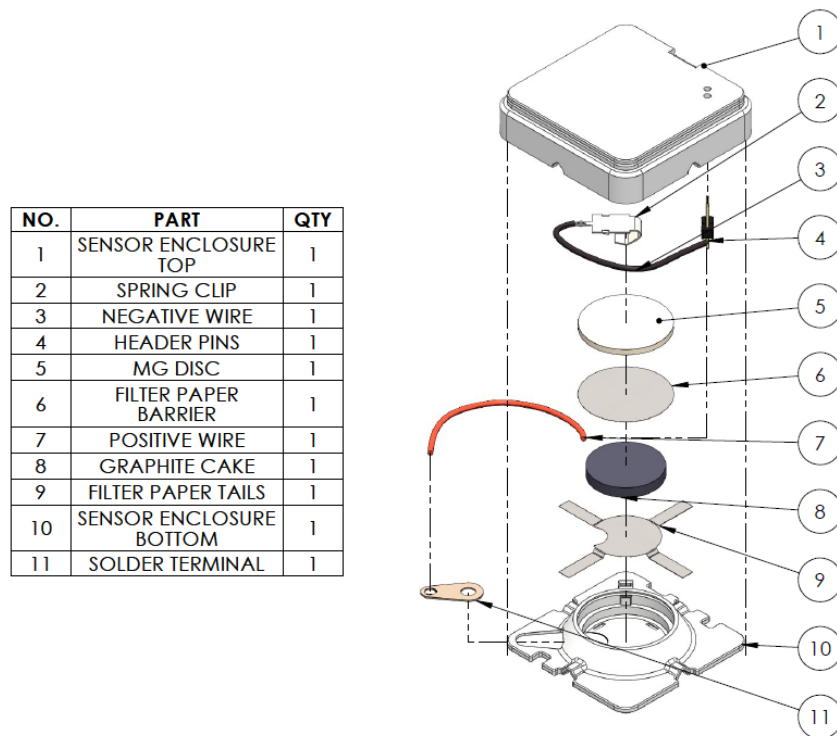


**Figure 37: Additional filter paper barrier component addition to sensor enclosure, part number 6.**

#### 4.5.4. Drop Testing

With the filter paper improvement to the sensor design, further evaluation of the sensor reliability was done by conducting a drop test. One source of concern for the sensor was possible damage to the graphite electrode during transport, for example, shipping and handling of the devices, or drops during installation. A preliminary test was done by releasing a single, closed sensor package from 50 cm. The package broke open, and the graphite electrode broke into multiple pieces, but remained in the 3D printed housing. When water was applied by a pipette, the electrode pieces were able to reshape into the typical graphite-water slurry that forms when unperturbed samples are used. This was promising enough to suggest a drop test from larger heights could be withstood.

The initial 3D printed packaging was very brittle and was not able to withstand drops from any significant height without damage or breaking open, however improved manufacturing quality, material selection and increasing the mating force between the packaging halves could solve these problems. These issues were later addressed, as detailed in section 5.2, however, for the meantime, a less stressful scenario was selected for the sensors. Instead of a direct drop condition, a drop test

with the sensors loaded in a shipping box to evaluate transport methods was done, outlined in Figure 38. A total of 10 samples were placed in a single shipping box, and the samples were tested for activation time after the drop test was done. Five placeholder samples were not tested, making a total of 15 physical sensor units. Two gateway boxes were included as well. In short, gateways are needed to relay BLE data from local environments to the cloud by using a cellular connection. More details on the wireless system are given in Appendix D. The shipment is meant to represent all components needed to use the water leak detection system.

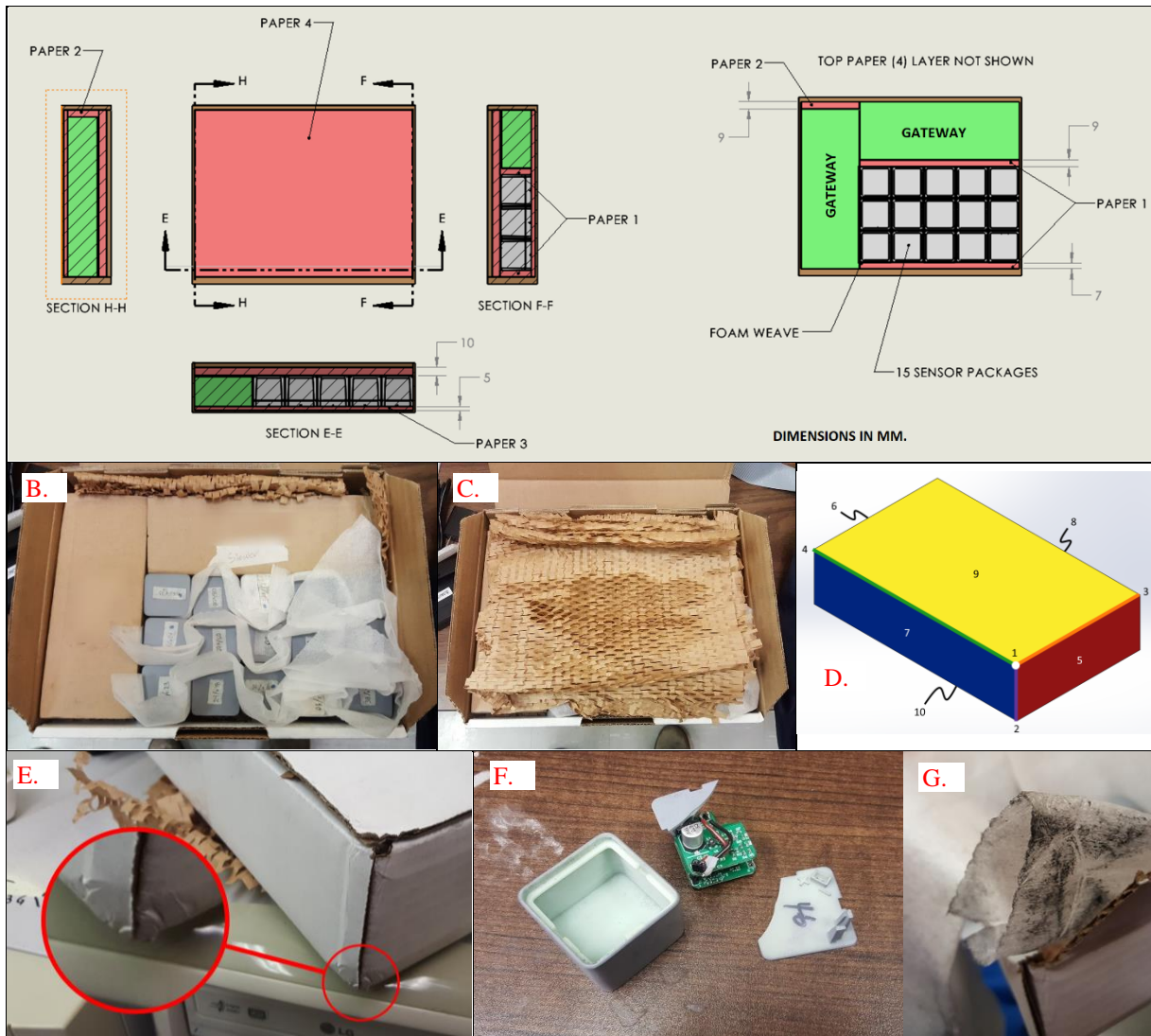


**Figure 38: Drop testing setup (A-D).** A) Packaging layout. The water leak sensors (Qty 15) are assembled into a shipping box along with wireless gateway box placeholders to represent a typical sensor system shipment. Foam is used to separate each sensor device, shown in B). Corrugated paper packaging is shown in red in A) and is clearly visible in C). D) Drop test steps reference image, showing target corner (1), edges (2-4) and faces (5-10). Post-drop inspection (E-G): E) Damage to corner of box, F) 3D printed electronics packaging with broken base, G) Some graphite material escaped from enclosure and is visible on foam layers.

The recommendations of [68] are used for the drop procedure, which refers to American Society for Testing and Materials’ “ASTM D5276 – 98 (2017)” standard, which is “applicable for containers weighing 110 lb (50 kg) or less”. A height of 1 m was used, which is above the 76 cm recommendation for packages below 9 kg, and the box was dropped onto the following list of targets (refer to Figure 38 D) [68]:

1. Drop on white corner.
2. Drop on purple edge.
3. Drop on orange edge.
4. Drop on green edge.
5. Drop on red face.
6. Drop on face opposite to red face.
7. Drop on blue face.
8. Drop on face opposite to blue face.
9. Drop on yellow face.
10. Drop on face opposite to yellow face.

The inspection of the package post-drop showed only one obvious device failure, where the base of the electronics enclosure broke, seen in Figure 38 F. Graphite was able to escape from the packaging, likely due to the sensor enclosure that opened slightly due to a poor snap fit, which was sample 5. The remaining 8 out of 10 sensors had no visible faults. All 10 samples were tested for activation time, but only to assess the performance of the sensor materials enclosure, and not the electronics. The broken electronics enclosure was replaced for this reason. Results of the sensor evaluation after the drop test are summarized in Table 10, and the relationship between OCV (measured post-activation time test) and the activation time is plotted in Figure 39.

**Table 10: Drop testing results for 10 samples from 1 m height in a shipping box**

Sample	Activation Time (s)	V <sub>oc</sub> / (V)	Notes
1	15	1.54	
2	17	1.59	
3	12	1.80	
4	20	1.66	
5	152*	1.50	*Snap fit issue
6	15	1.74	
7	21	1.53	
8	12	1.67	
9	18	1.74	
10	Not activated**	-	**Assembly error, Mg missing
<b>Average</b>	<b>16.3</b>	<b>1.64</b>	With sample 5. Without sample 10
<b>Average</b>	<b>31.3</b>	<b>1.66</b>	Without sample 5. Without sample 10

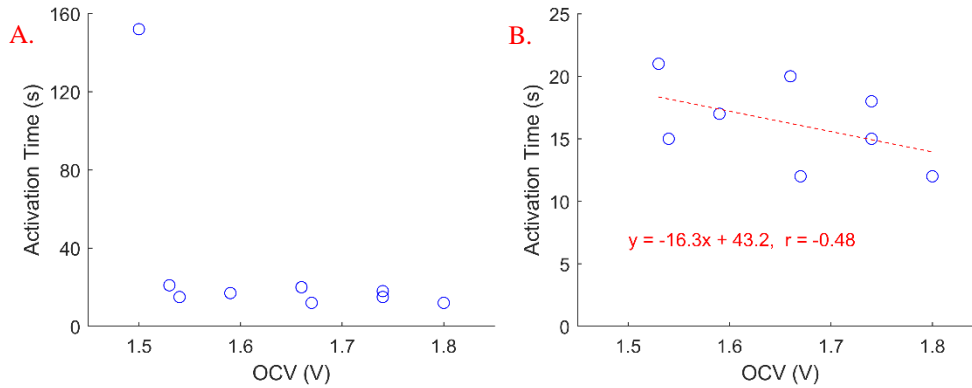


**Figure 39: Relationship between OCV and activation time after the drop test. Voltage measured after activation time test with load removed. A) All test data, excluding sensor without Mg piece. B) All activation times below 1 minute, sample with snap fit issue removed. Linear fit and correlation coefficient,  $r = -0.48$ .**

Sample 10 did not activate, and upon opening, it was found that the magnesium piece was not inserted at all. The average activation time post-drop was 16.3 s, disregarding the samples 5 and 10. The sample with the snap fit issue was partially opened after the drop, since the annular snap on the sensor enclosure did not hold during the drop, and if included, the average activation time is 31.3 s. The sample with an assembly error highlighted the need for quality checks in the assembly process, which is addressed in Chapter 5. The OCV was also measured after the activation time test, by removing the BLE and EH board load at the end of the test duration. Sample 5 showed the lowest OCV after testing, which suggests the voltage is a potential indicator of lower power output without loading the device. However, upon further inspection, the correlation coefficient between activation time and voltage is only  $-0.48$ , indicating some negative correlation between the two, but not a strong correlation. However, the lowest voltage measured was also the highest activation time, and was not used in the regression, so instead the effect may be more discrete, with performance degrading rapidly below a certain OCV threshold.

#### 4.5.5. Assembly Steps Evaluation

3D printing was selected as the fabrication method for the custom parts in the assembly. However, in addition to printing the enclosures, the off-the-shelf parts, wiring, and custom PCBs needed to be mounted into the enclosure and soldered together. This requires a significant amount of work to complete for each sensor unit. The steps are outlined in Table 11. For the sensor enclosure, 11 manual steps are needed after printing is completed, and for the electronics enclosure, 8 are

required. The steps involved are tedious in some cases, and this is highlighted by the Time Used column, in which 9 steps are high time consumption, requiring 1 min to 5 min each.

**Table 11: Assembly steps for 3D printed design**

	Step #	Step Description	Time Used
<b>Sensor Pkg.</b>	1	Cut and strip wires to prepare for soldering.	Moderate
	2	Prepare to solder wires and pins by adding small quantity of solder to each.	High
	3	Solder wires to graphite solder terminal lug and magnesium spring contact.	High
	4	Remove support material from 3D printed top part for spring clip feature.	High
	5	Feed wire and spring contact through mounting location.	High
	6	Press solder terminal lug contact into mounting location	Low
	7	Solder other ends of contact wires to header pins.	High
	8	Use hot-melt adhesive to attach pins and solder terminal lug into mounting location.	Moderate
	9	Add the filter paper pieces to the assembly using tweezers.	High
	10	Add the graphite electrode, and magnesium disc on top of the filter paper.	Low
	11	Close the assembly by pressing shut until snap fit is achieved.	Low
<b>Electronics Pkg.</b>	1	Cut and strip wires to prepare for soldering.	Moderate
	2	Prepare to solder wires and pins by adding small quantity of solder to each.	High
	3	Solder wires to EH board.	Moderate
	4	Solder other ends of wires to header receptacle.	High
	5	Remove support material from 3D printed base for hex nut feature.	Moderate
	6	Mate PCBs together, then screw onto base with the screw, spacer, and hex nut.	High
	7	Use polymer glue (hot glue) to attach header receptacle into mounting location.	Moderate
	8	Close the assembly by pressing the lid onto the base.	Low

#### 4.5.6. 3D Printing Quality

The overall appearance of the 3D printed design was acceptable. The prints outsourced to a manufacturer are shown in Figure 40. Some very small details, less than 1 mm in cases, such as the holes for the header pins, and the mounting locations for the sensor electrical contacts printed without issue. One type of detail however did not print well, and this was the annular snap fits. Annular snap fits were used to attach the top of the sensor enclosure to the bottom of the sensor enclosure, as well as the sensor enclosure to the electronics enclosure. The snap fit printed slightly differently in the outsourced, higher volume print than the prototype prints, which caused a misalignment between the two parts of the snap, making it impossible to snap the two halves together by hand in some cases. Consequently, the sensor enclosure was often not held together properly, and this sensor performance, for example, sample 5 in section 4.5.4: Drop Testing. The annular snap fit design was effective when the print quality was closely monitored during in-house printing, but each 3D printer varies. The dimensions in the 3D models did not represent the final

print when fabricating in-house, but instead had been tuned to compensate for predictable dimensional deviations observed for the printer in the lab, which was the LulzBot TAZ 6 [63]. When outsourced, the same mating force and performance was no longer achieved, since the compensations were tuned only to that printer.

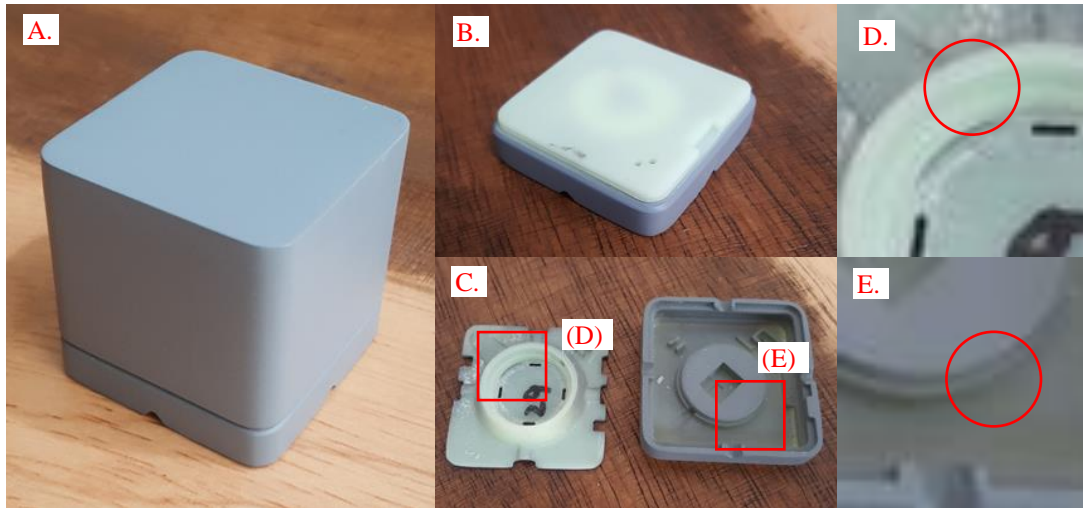


**Figure 40: 3D printed version of sensor packaging, outsourced. A) Full leak detector, B) sensor enclosure, closed, C) sensor enclosure, opened. D, E) Close-up of location where annular snap feature would be located if the print detail was high enough.**

The print quality was also assessed by measuring two critical dimensions on the sensor units, as shown in Figure 41. In Figure 41 and Table 12, the graphite cavity diameter and the graphite cavity height are the dimensions of the cylindrical chamber that houses the graphite electrode. Measurements were taken on five 3D printed samples from the set of 50 using digital calipers. The dimensions varied from the modeled value by only 0.07 mm in both cases. This is not significant enough to affect the sensor performance regarding the graphite cavity dimensions, however this is sufficient to alter the previously discussed annular snap performance. The failure of the annular snap is not due to low quality printing but rather a poor choice design for 3D printing.

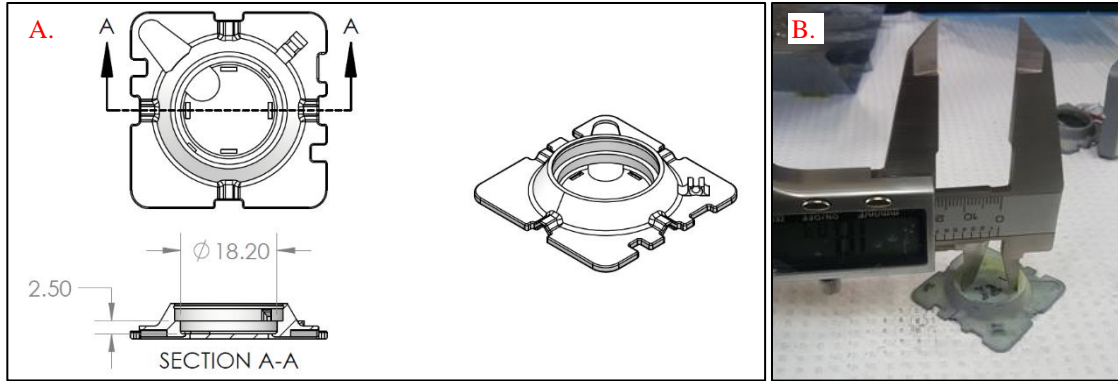


**Figure 41: A) Inspection dimensions for graphite cavity on 3D printed sensor enclosure, B) measuring graphite cavity diameter with digital calipers**

**Table 12: Actual 3D printed dimensions of graphite cavity versus specified dimension**

Feature	Specified value	Measurements by sample number					Calculation	
		1	2	3	4	5	Mean	$\sigma$
Graphite cavity diameter (mm)	18.20	18.18	18.09	18.15	18.14	18.14	18.13	0.0327
Graphite cavity height (mm)	2.50	2.58	2.48	2.54	2.49	2.53	2.57	0.0455

## 4.6. Discussion of Design and Manufacturing Flaws

### 4.6.1. Magnesium Spring Contact Deflection vs Package Closing Force

The typical application of the spring contact is for AAA batteries as previously discussed. However, the spring contacts are typically mounted in a pair, facing one-another, into a common rigid base material. This way, the distance between the contacts is constant. In the sensor packaging design though, the spring contact force opposes the mating force for the annular snap that holds the two halves of the packaging together. As previously mentioned, the annular snap print quality was low, and paired with this added force from the spring contact, the snap fit would often not hold. The electrical contact to the magnesium disc would then be unstable, and the sensor packaging would not properly shut. A more reliable method of mating the sensor enclosure pieces was selected in the future designs, rather than abandoning the spring contact.

### 4.6.2. Graphite Electrical Conductivity and Water Saturation Level

The graphite electrode is an excellent electrical conductor. If, however, the graphite electrode does not become fully saturated with water when activated, the dry portions will behave as loads on the

sensor, dissipating some of the power produced. This is shown in Figure 42, along with one of the potential solutions, which is adding a separator layer between the magnesium and the graphite-water mixture, which insulates the two. The concept is like a separator layer in a battery, which has a low resistance to ion movement, but a high electrical resistance [69].

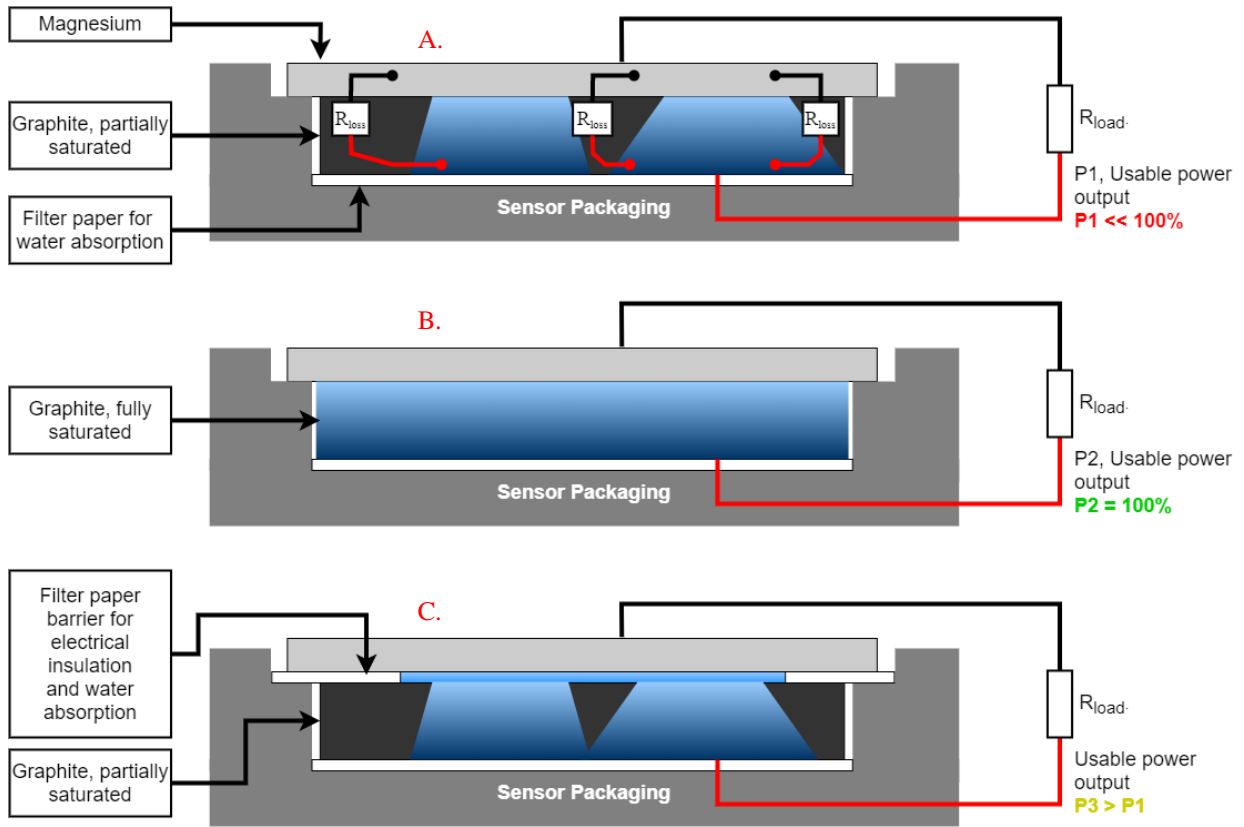


**Figure 42:** A) Self-discharging from water to magnesium via dry graphite B) No self-discharging since graphite is fully saturated (no dry areas) C) No self-discharging due to insulating barrier

### 4.6.3. Packaging Form and Assembly Ease

The outline of the assembly steps in section 4.5.5 demonstrated that the water leak detector preparation is a non-trivial task. The objective of the water leak detectors was to be lower cost than alternatives due to the simplicity of the electrical design. The problem is that the mechanical design and packaging requires many individual components to be assembled and is time consuming to the point of being unfeasible as a mass producible device for large scale water leak detection.



#### **4.6.4. Variable Beacon Activation Time and Low Yield Rates**

In some cases, the beacon activation time of the sensor was significantly longer than others. For example, in the complete system test (section 4.5.1), the first sample responded in 30 seconds, whereas the second took 75 s. In the drop test (section 4.5.3), one sensor had a beacon activation time of 152 s, whereas the average beacon activation time of the other eight samples was 16.3 s. While many of the factors surrounding the variation in activation times and yield rates have been either addressed or identified, the objective moving forward will be to control these defects by improving design and assembly steps.

#### **4.7. Summary of Chapter 4**

This chapter detailed the prototyping process for the water leak detector. This involved integrating the previously developed sensor materials and electrical designs into a single packaged water leak detector prototype. The critical design components are the materials housing size and shape, the electrical contacts, and the water absorption features. The sensor was tested for electrical performance and as a water leak detector. The device was functional in some tests but showed a low yield rate. The reliability of the sensor must be improved to be used as a proper water leak detector solution.

# Chapter 5. Water Leak Sensor Production Design

## 5.1. Introduction to Chapter 5

There were two objectives for Chapter 5. Firstly, address the flaws in the 3D printed prototype to improve yield rates. Secondly, create an enclosure that could be injection-moulded for higher production volumes. Injection moulding involves machining a mould tool for many uses, meaning design modifications are expensive. This design was made to be more robust and reliable, in exchange for slightly higher costs, to maximize chances of increasing yield rate without iteration.

## 5.2. Design and Manufacturing Changes from 3D Printed Version

### 5.2.1. Sensor Packaging Screws

As previously discussed, the annular snap used to hold the two halves of the sensor enclosure together was not sufficient due to the high force applied by the spring contact and limited quality of 3D printing. A straightforward solution was to add threaded heat set inserts, which provide a metal thread for a screw in plastic parts. This design change is shown in Figure 43.

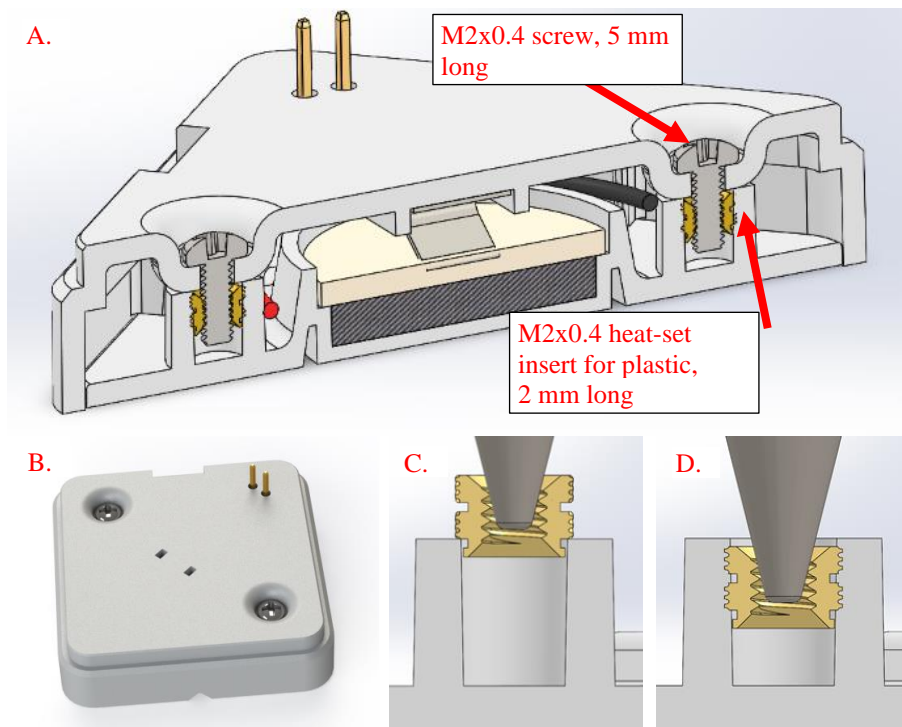


**Figure 43: Modified design, screws replace annular snap. A) Cross section view B) enclosure assembled, C) & D) cross section, before and after pressing insert into place with soldering iron tip**

### 5.2.2. Design for Injection Molding

While 3D printing is relatively low cost for a small batch of prototype parts, the costs do not scale well, as the operation time and resources required increases relatively linearly with quantity of parts produced. Injection molding on the other hand requires a high upfront investment for tooling, but offers incredibly low per-part manufacturing rates, making it an ideal option for higher quantities. The changes categorized as “design for injection moulding” are the ones made only to accommodate the moulding process. Other changes are listed separately in this section.

To summarize, there are several design guidelines and requirements to follow when injection molding parts, including appropriate draft angle selection, consideration for overhangs or undercuts, uniform wall thicknesses and radii, and uneven cross sections. A list of the major changes made to enable injection moulding is given in Appendix C. The overall part functionality and appearance was relatively unchanged from the changes in that list.

### 5.2.3. Filter Paper Shape Modification

Filter paper component preparation was originally outsourced to a laser cutting shop, but later was done with the Cricut Explore Air 2 [70], which was available in the lab for sample preparation. The piece below the graphite electrode was merged into a single component to remove the need for assembling the 3 pieces individually. A patterned layout consisting of the papers with tails and the barrier pieces was used to produce filter paper components in equal quantities while minimizing wasted sheet area.

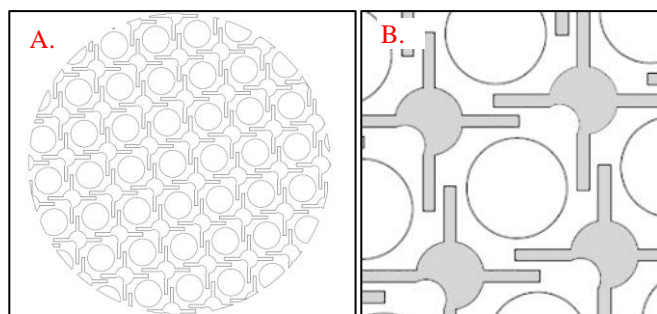


**Figure 44: New filter paper patterning. A) Pattern cut from 24 cm diameter filter paper sheets. B) Close-up of pattern, pieces with tails shaded**

#### **5.2.4. Graphite and Magnesium Chamber Diameter**

The size of the chamber in which the graphite and magnesium components sit was reduced in this design. First, the graphite chamber was reduced from 18.2 mm diameter to 17.2 mm diameter. The graphite disc is 16.7 mm in diameter, but based on testing by colleagues for ideal size of the graphite cavity, the clearance of 1.5 mm was much more than needed to allow graphite disc expansion, so this clearance was reduced to 0.5 mm. The chamber for the magnesium was also reduced to match a standard blanking tool used to fabricate the Mg discs in higher volumes. Previously a 3/4" (19.05 mm) punch was used but moving forward a 47/64" (18.65 mm) blanking punch and die set was selected to produce flatter discs. The graphite disc itself did not change in size, and so the active surface area of the device also remained constant. This means the output power should theoretically be unaffected by these modifications.

#### **5.2.5. Magnesium Disc Thickness Check**

When punched, the magnesium discs used for the sensor enclosure have a thickness of around (1.5 to 1.6) mm. This thickness decreases after sanding and polishing the disc and can decrease significantly if the disc is re-used from test to test, with polishing and sanding done in between. In some cases, the Mg disc became so thin that the contact between the spring contact and Mg disc was compromised, since the distance between the two affects the contact force. Therefore, an additional measurement step when re-using the discs was added, by measuring the thickness with a caliper. The acceptable thickness is 1.4 mm to 1.6 mm, anything thinner should not be used in the current design. This helps to improve the yield rate of assembled sensors.

#### **5.2.6. Resistance Check**

One potential error during the packaging assembly was the barrier layer between magnesium and graphite did not fully block the graphite electrode from contacting the magnesium electrode, which could result in a short-circuit if the amount of water absorbed is low. This could occur if the graphite cake cracks slightly and some material lands around the magnesium discs' location. Also, some sensor packages, after being used a single time, are cleaned, and re-used in further tests by replacing the graphite and magnesium electrodes. In this case, the graphite, if not properly removed, could remain on the sides of the sensor enclosure. While both these scenarios could be caught by visual inspection, they can also easily go unnoticed. A more reliable post-assembly check is measuring the resistance of the sensor packaging across the two output pins. With a basic

handheld multimeter, the resistance without a short-circuit should be  $> 10 \text{ M}\Omega$ , or readout an overload since it exceeds the multimeter's measurement range. However, if the graphite is in contact with the magnesium, a lower resistance will be measured, indicating an assembly failure.

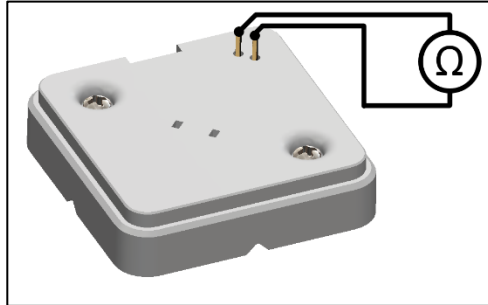


**Figure 45: Post-assembly resistance check across sensor terminals. A handheld DMM can be used to quickly measure the resistance.**

### 5.3. Leak Sensor Packing Evaluation

#### 5.3.1. Visual and Dimensional Inspection

The sensor packaging was fabricated without any visible defects on the features, unlike with 3D printing. Careful evaluation and modification of the design prior to injection moulding made this possible. The changes to the sensor packaging are visible in Figure 46.

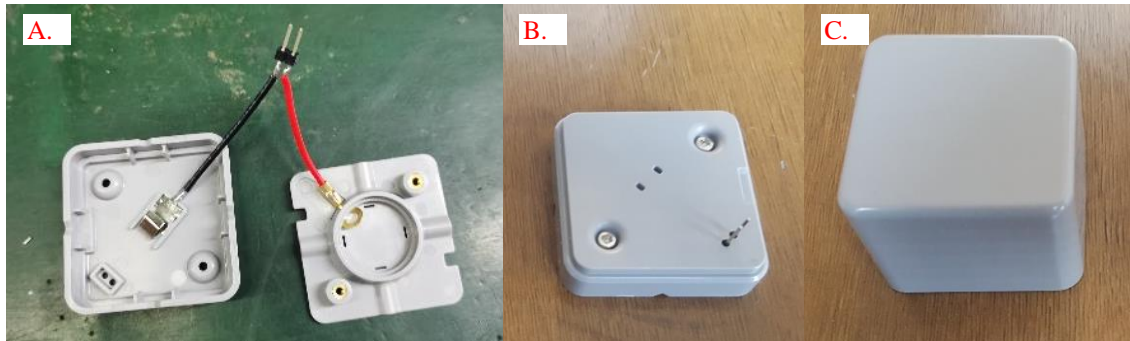


**Figure 46: Injection moulded sensor packaging design. A) Opened sensor enclosure showing wiring partway through assembly. Magnesium, graphite, and filter paper not present, and the header pins are not yet mounted into the holes through the lid of the sensor enclosure. B) Completed sensor enclosure, and C) electronics enclosure.**

As was done with the 3D printed design, the injection moulded sensor packages were measured to assess the dimensional accuracy. Measurements of the graphite cavity diameter and height are given in Table 13. For images refer to Figure 41, in section 4.5.6.

**Table 13: Actual injection moulded dimensions of graphite cavity versus specified dimension**

Feature	Specified value	Measurements by sample number					Calculation	
		1	2	3	4	5	Mean	$\sigma$
Graphite cavity diameter (mm)	17.20	17.01	17.02	17.05	17.05	16.99	17.02	0.0261
Graphite cavity height (mm)	2.50	2.45	2.43	2.48	2.49	2.48	2.47	0.0251

The standard deviation between samples was about half that when 3D printing, which is expected, as the injection moulding process is more precise. While the mean cavity height was very close to the specification, the diameter was much less accurate. The specified tolerance on the diameter was  $17.2 \text{ mm} \pm 0.13 \text{ mm}$ , meaning  $17.07 \text{ mm}$  to  $17.33 \text{ mm}$ . The additional error may have been a miscommunication in drawing specifications. The graphite cavity was dimensioned as  $17.2 \text{ mm}$  at the base of the feature, whereas the manufacturer may have set the top of the feature to be  $17.2 \text{ mm}$  and drafted inwards from there, resulting in a smaller diameter at the base, which would be approximately  $0.08 \text{ mm}$  to  $0.16 \text{ mm}$  for a  $1^\circ$  to  $2^\circ$  draft angle. An inner radius on the lower corner would decrease measured diameter as well.

### 5.3.2. Electrical Testing

Next, electrical testing was done to assess the quality of the new injection moulded design. Three samples each were used in the OCV and SCC tests as per sections 3.2.2 and 3.2.3. Results are presented in Table 14 and Table 15 respectively. Ten samples were used for the load test, following section 3.2.4. Of these 10, five samples were done with constant current of  $50 \mu\text{A}$ , like with the unpackaged materials, and five were done with constant voltage of  $400 \text{ mV}$ , which matches the operating point in the water leak detection application, see Appendix B.2. Results for the load test are presented in Table 16. Plots of all test results are given in Figure 47.

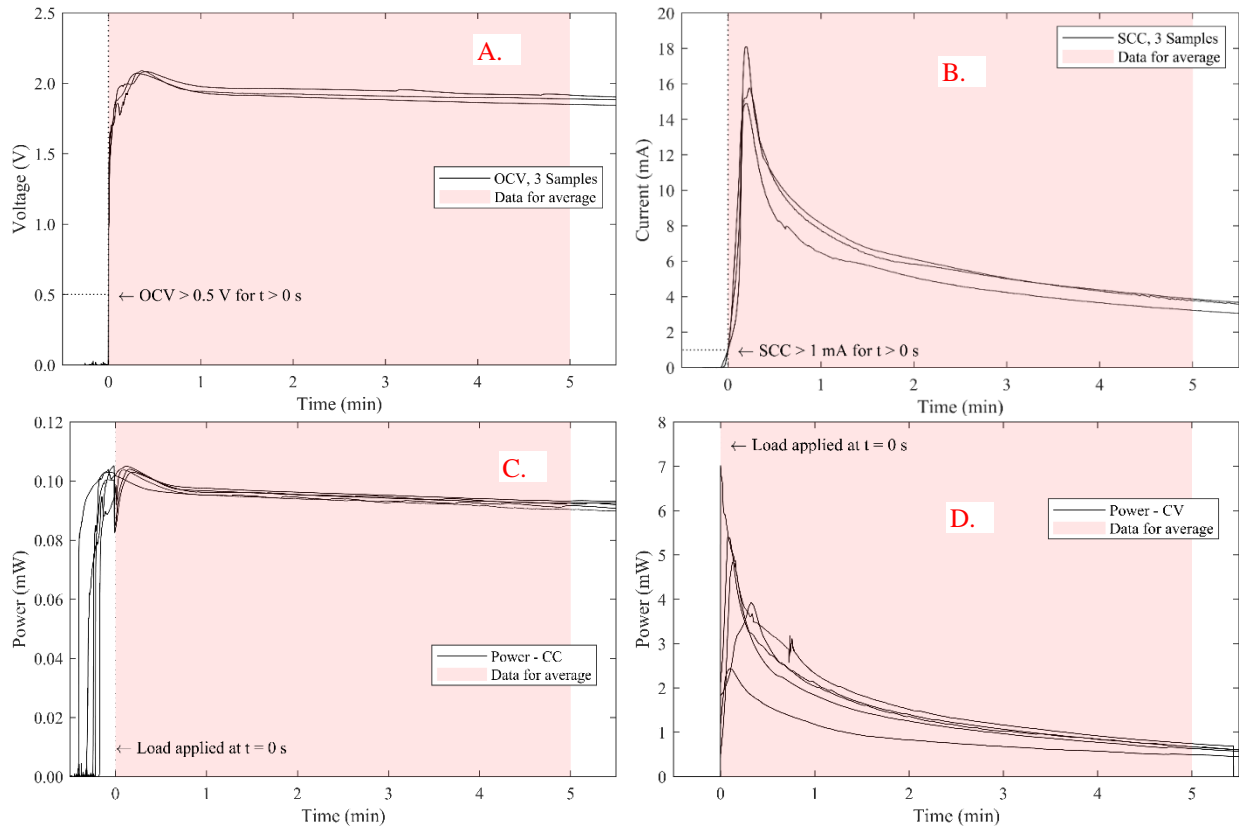


**Figure 47: Sensor electrical test results for injection moulded enclosure. A) OCV test condition, B) SCC test condition, C) Load test condition output power when  $I_{source} = 50 \mu A$ , D) Load test condition output power when  $V_{source} = 400 mV$**

**Table 14: OCV test results for injection moulded design of sensor enclosure**

Measurement	Baseline	Injection Moulded			
	Unpackaged Sensor	Sample 1	Sample 2	Sample 3	Average
$\overline{V_{OC}} / (V)$	1.80	1.92	1.90	1.95	1.92
$V_{OC,MAX} / (V)$	1.87	2.09	2.07	2.08	2.08

**Table 15: SCC test results for injection moulded design of sensor enclosure**

Measurement	Baseline	Injection Moulded			
	Unpackaged Sensor	Sample 1	Sample 2	Sample 3	Average
$\overline{I_{SC}} / (mA)$	6.0	6.3	6.1	5.3	5.9
$I_{SC,MAX} / (mA)$	16.4	18.1	15.8	14.9	16.3

Relative to the baseline, the OCV of the injection moulded design averaged 0.12 V higher over the first 5 minutes after water application. The peak voltage was also 0.2 V higher compared with unpackaged sensor materials. The SCC averaged 0.1 mA lower and peaked at 0.1 mA less than the baseline, which is a very small difference. However, compared to the average current of 4.5 mA with the 3D printed design, this marks a significant improvement.

**Table 16: Load test results for injection moulded design of sensor enclosure**

Measurement	Baseline	Injection Moulded					
	Unpackaged Sensor	Sample 1	Sample 2	Sample 3	Sample 4	Sample 5	Average
$\overline{P}_{CC} / (\text{mW}),$ ( $I_{CC} = 50 \mu\text{A}$ )	0.077	0.094	0.096	0.095	0.095	0.094	0.095
$\overline{P}_{CV} / (\text{mW}),$ ( $V_{CV} = 0.4 \text{ V}$ )	N/A	0.903	1.362	1.723	1.451	1.530	1.394

The load test at 50  $\mu\text{A}$  gave slightly higher output power, 0.095 mW versus 0.077 mW. This is expected when considering the OCV was slightly higher as well, since the 50  $\mu\text{A}$  load test is a very small load, and the test condition is therefore close to the OCV condition. The output power when the voltage was fixed to 0.4 V was 1.394 mW, which was not tested with bare sensor materials. However, this is significantly higher than the 40 uW needed for the BLE transmission [71], which indicates electrical performance should be more than sufficient.

### 5.3.3. Beacon Activation Time and Yield Rate Testing

As explained in section 3.3.1, the activation time test measures the time from water exposure to Bluetooth beacon activation. This is important to assure the timely reporting of water leaks when a leak event occurs. The sensor activation time can vary from sample to sample, and the purpose of the testing is to understand the distribution of activation times. The percentage of sensors that fall under a given activation time can then be estimated. Figure 48 shows a typical sensor response when water is applied. The capacitor voltage begins to rise once the sensor voltage increases at around 6 seconds. When the sensor voltage begins to alternate between high (1.5 V to 2 V) and low (less than 1 V) values at around 20.5 s, the load has been enabled. The BLE chip has a start-up time around 1 s, and the BLE transmissions start around 22 s. The capacitor reaches a maximum voltage of 3.6 V once the BLE chip is enabled.



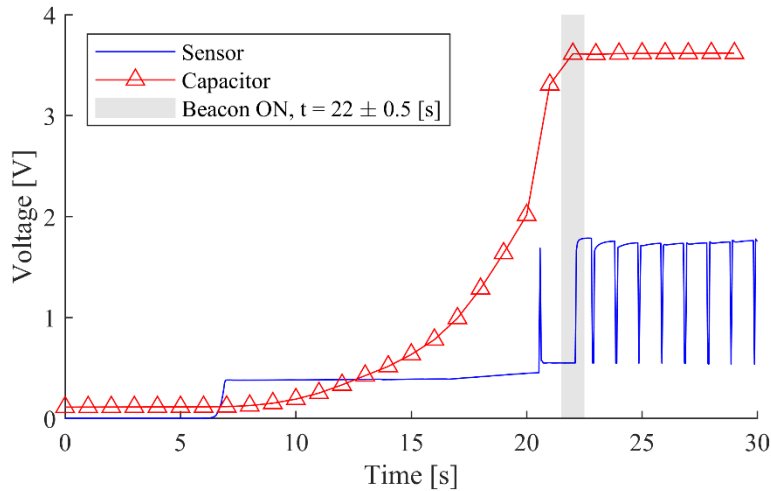


**Figure 48: Beacon activation test for injection moulded packaging, with sensor output voltage and storage capacitor voltage measured.**

For the activation time test, 25 samples were tested. The activation time is recorded for 24 of these samples in Figure 49 A. One sample was not properly tested, as the capacitor on the energy harvesting board was not discharged after being used in a separate test, and therefore the very short 13 s activation time was rejected.

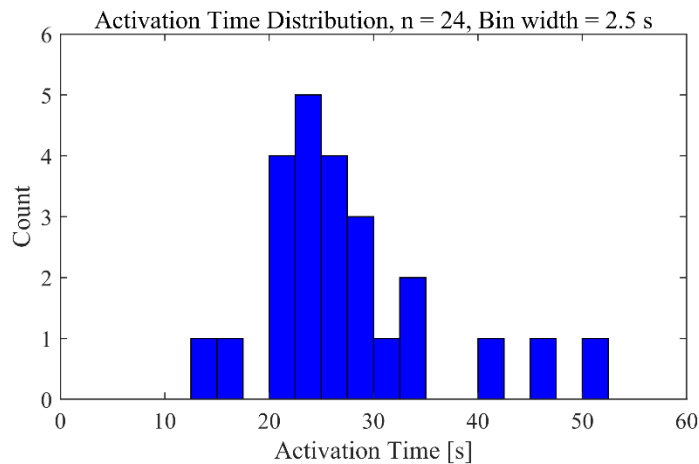


**Figure 49: Results of beacon activation testing, n = 24 samples, bin width = 2.5 s.**

The mean activation time was 27.6 s, and the maximum time was 50 s, well below the 1-minute objective. All 24 samples were activated, which is a 100% yield rate for a sample size of 24. This indicates the sensor enclosure design is quite reliably producing adequate output power to give a timely response to water contact. Summary of activation time measurements are given in Table 17.

**Table 17: Summary of activation time results**

<b>Samples Tested</b>	24
<b>Samples Passed</b>	24
<b>Yield rate</b>	100%
<b>Mean Activation Time(s)</b>	27.6
<b>Sample std. dev. of activation time (s)</b>	8.39

## **5.4. Summary of Chapter 5**

Chapter 5 presented refinement on the prototype design presented in Chapter 4. Failure modes were identified and solved through design and manufacturing changes. The new design was fabricated with injection molding and the sensor enclosure electrical performance was tested a second time. The electrical performance was equivalent to or better than the baseline sensor materials in all cases. An activation time test was done as well to quantify the expected activation time for a sample of sensor devices and determine a yield rate for the devices. The yield rate was significantly improved when compared with the previous 3D printed design, and the mean activation time was far below the desired 1-minute objective.

# Chapter 6. Conclusions

## 6.1. Conclusions

1. A functional water leak detection device that operates without an external power source has been completed in this project. The work here described the integration of the sensor materials and electronics into a single mechanical housing, demonstrating that materials science research in water-based energy harvesters and generators can be used in an applied sensor design. To the best of the author's knowledge, this is the first complete water leak detection device prototype that sources power from the water itself, rather than a battery or AC power outlet.
2. The design of the packaging for the sensor materials involved testing and assessment of the sensor materials in a variety of packaging iterations to determine the critical parameters to the design. The key factors in the sensor enclosure design were the diameter and height of the graphite electrode cavity, the water channel geometry and paper wicking tail design, and the packaging assembly force. Additional key factors unrelated to the design of the enclosure include material selection, with graphite being preferred to CNFs, inclusion of a separator layer between the carbon and Mg electrodes, and carbon electrode fabrication controls.
3. The packaged sensor performance was more than sufficient in pure electrical testing scenarios. The packaged device met or exceeded the baseline performance standard in the OCV, SCC, and load tests. The power output in the fixed voltage load test was over 1.3 mW, which is more than an order of magnitude greater than the power requirements for the BLE device used in the electronics design. This demonstrated that the packaging design was more than adequate for the leak detection application.
4. The device performance as a water leak detector was very reasonable in the final design iteration. The activation time was under 1 minute for all samples from the injection molded design iteration, with a 100% yield rate. This is a promising result for the device as a water leak detector, as reliability is a critical metric for such applications. Further investigation would be needed to determine if the sensors could be used multiple times for a water leak detection event.

## 6.2. Recommendations and Future Work

Some recommendations are given below, which would improve the understanding of the water leak detector.

1. Some of the design considerations for the sensor enclosure were not quantified. For example, the effect of applied force on the graphite electrode is reported to decrease the voltage output, but the relationship with regards to the magnitude of force relative to the magnitude of voltage change was not studied. Instead, applied force to the graphite electrode was avoided entirely. It would be beneficial, time permitting, to design an experiment where force is varied and voltage fluctuations are measured, to understand what levels of force are acceptable. There will always be some application of forces in the packaging, especially if the device is to be made more compact going forward. Other effects like this include the probe tip insertion depth, which is known to alter current and voltage but to an unknown degree, and likely the most difficult to study, the effect of cracking in the graphite electrode on electrical performance.
2. The selection of contacts for the graphite and Mg electrodes was done mainly to facilitate prototype development with readily available tools in the lab environment, and therefore more complex methods of electrical contacts such as crimps, welds, or custom contact designs were not used. The contacts selected however are bulky, with the Mg contact having a thickness of 2.65 mm in the enclosure, more than the magnesium disc itself. The sensor design could be condensed considerably with improvements upon the contact design. This would be of interest for applications where a small form factor is required, for example, when placing a sensor below an appliance.
3. The reason for sensor failures is incredibly difficult to assess. In rare occasions, the sensor is missing a component, such as the magnesium plate. For the most part, however, when a test is complete, upon opening several sensor enclosures, one finds that the sensor devices that failed have generally comparable appearance to those that did not. The contact between the graphite and Mg electrodes is good, the graphite electrode is sufficiently saturated with water, and the contacts to each electrode measure low resistance. This makes improving yield rates very difficult, since rather than assess the failed sample, instead, one must assess the potential sources of variability during the fabrication of a sample. Therefore, the recommendation to further improve predictability of device performance would be that

additional studies on manufacturing process parameters be conducted. For example, intentionally modifying the paper wicking tails with an occasional defect and observing the severity of the flaw. Currently, it is not well understood what the main sources of performance variation are, and this may help identify them.

4. The design of the water channels and paper tails was done mostly by experimental procedure. It could be beneficial to attempt to simulate the fluid behaviour at the inlets to the enclosure, the absorption and capillary action with the paper tails, and the absorption through the graphite electrode. This could help to improve or simplify the geometry of the enclosure design. In addition, a better design for the channels, either by changing form or materials, could eliminate the filter paper pieces completely while maintaining sensitivity and response time. The filter paper tails were tedious to assemble and quite fragile, and so this would be very beneficial to achieve.

There are a significant number of directions for future work with the sensor device that could be explored, such as furthering assessing the water leak detector's performance, or reapplying the design process to areas beyond water leak detection.

1. There is a long list of untested conditions for the water leak detector that would be required before deploying the sensor as a commercially viable device. These tests would put the sensor through more strenuous environments and could help improve the enclosure design by identifying flaws. Some of these tests include waterproofness, effect of drying time on sample reusability, drop testing the sensor units directly, effects of long-term sensor storage, temperature and humidity, dust and debris exposure, water sensitivity, and effects of the surface type below the sensor.
2. There are also opportunities for improving the water leak detector's manufacturability, cost, and form factor. The main issues with manufacturability lie in the manual assembly steps involved in adding the paper wicking tails and soldering numerous wired components together. Redesign of the enclosure to eliminate components or replace them with easily assembled alternatives would be recommended if another design iteration was done. For cost, there is opportunity of developing a sensor enclosure that integrates many Mg-graphite layers in series, which would greatly simplify electronics design, and therefore cost. In addition, manufacturability improvements lower the devices cost as well. Lastly, as previously mentioned, contacts for graphite and Mg could be improved, and if the

electronics are simplified in parallel, the device could be designed to an estimated size of 5 cm x 3 cm x 1 cm, or better, giving it a very thin vertical profile. The current size is approximately a 4 cm cube.

3. Another very promising application of the self-powered water leak sensor is in the medical field. Notably, in remote patient monitoring and smart wearables, there is increasing demand for smart devices, some of which could leverage the water-based power generation used here [43, 47]. The first application to explore would be smart diapers, devices that could gather biomarker data and help better track patient health, particularly in the elderly, easing workloads and improving efficiency for nursing home staff. Second, smart bandages can offer automated insights into wound healing processes, bettering healthcare in the hospital setting, but more importantly, after a patient has been sent home. Devices that can help physicians track a released patient's health following a hospital visit are of high interest as they have potential to improve healthcare and reduce costs [72]. In both cases, the moisture sensing device could be adapted to a wearable form factor.

## References

- [1] Zurich Insurance Company Ltd., "A cure for water damage in offices and habitational buildings," Canada, 2014.
- [2] K. Faloon, "The High Cost of Water Leaks," *Plumbing & Mechanical*, vol. 22, no. 9, p. 42, 2004.
- [3] J. Feng et al., "High-Performance Magnesium–Carbon Nanofiber Hygroelectric Generator Based on Interface-Mediation-Enhanced Capacitive Discharging Effect," *ACS Appl. Mater. Interfaces*, vol. 12, no. 21, pp. 24289-24297, 2020.
- [4] J. Teo, "Carbon and TiO<sub>2</sub> based electrodes with metal alloy electrode for self-powered detection of water," MAsc. thesis, MME, Univ. of Waterloo, Waterloo, 2021.
- [5] Z. Liu and Y. Kleiner, "State-of-the-Art Review of Technologies for Pipe Structural Health Monitoring," *IEEE Sensors Journal*, vol. 12, no. 6, pp. 1987-1992, 2012.
- [6] S. Hamilton and B. Charalambous, *Leak Detection: Technology and Implementation*, London: IWA Publishing, 2013.
- [7] R. K. Parida, V. Thyagarajan and S. Menon, "A thermal imaging based wireless sensor network for automatic water leakage detection in distribution pipes," in *IEEE International Conference on Electronics, Computing and Communication Technologies*, Bangalore, India, 2013.
- [8] Alert Labs, "Flowie Water Flow Sensors," 2021. [Online]. Available: <https://alertlabs.com/products/flowie-water-sensor>.
- [9] Moen, "Flo Smart Water Monitor and Shutoff," 2021. [Online]. Available: Flo Smart Water Monitor and Shutoff.
- [10] D. M. Raymond, "Aqueous chemical leak detection cable". United States Patent US8256269B2, 4 September 2012.
- [11] Alert Labs, "Floodie Flood Sensor," 2021. [Online]. Available: <https://alertlabs.com/products/floodie>.
- [12] Nowa, "Flood / Freeze Sensor Technical Datasheet," 2020. [Online]. Available: <https://nowa360.com/wp-content/uploads/2020/11/Technical-Data-Sheet-NOWDSF360.pdf>.
- [13] Moen, "Moen Smart Leak Detector, 1 Pack," 2021. [Online]. Available: <https://www.moen.com/products/920-004>.

- [14] Honeywell, "Resideo One Time Use Water Leak Sensing Alarm, RWD14 - 4 Pack," 2021. [Online]. Available: <https://www.honeywellstore.com/store/products/water-alarm-single-use-4-pack-rwd14.htm>.
- [15] The Basement Watchdog, "Watchdog Water Alarm," 2021. [Online]. Available: <https://www.basementwatchdog.com/watchdog-water-alarm/>.
- [16] Govee, "Govee Wi-Fi Water Sensors Alarm," 2021. [Online]. Available: <https://us.govee.com/collections/all-products/products/wireless-water-leak-detector>.
- [17] Wasserstein, "AC Powered Smart Wi-Fi Water Sensor," 2021. [Online]. Available: <https://wasserstein-home.com/collections/smart-water-detector/products/ac-powered-smart-wi-fi-water-sensor-flood-and-leak-detector-with-6ft-1-8m-cable-alarm>.
- [18] Wasserstein, "Wasserstein WiFi Water Leak Sensor, Smart Flood Detector," 2021. [Online]. Available: <https://wasserstein-home.com/collections/smart-water-detector/products/wasserstein-water-leak-detector>.
- [19] Phyn, "Phyn Smart Water Sensor," 2021. [Online]. Available: <https://www.phyn.com/smart-water-sensor/>.
- [20] Phyn, "Phyn Plus Smart water assistant + shutoff (2nd Gen)," 2021. [Online]. Available: <https://www.phyn.com/plus-smart-water-assistant/>.
- [21] IoT Analytics, "State of IoT - Summer 2021," 2021. [Online]. Available: <https://iot-analytics.com/number-connected-iot-devices/>.
- [22] J. Gubbi, R. Buyya, S. Marusic and M. Palaniswami, "Internet of Things (IoT): A vision, architectural elements, and future directions," *Future Generation Computer Systems*, vol. 29, no. 7, pp. 1645-1660, 2013.
- [23] L. Atzori, A. Iera and G. Morabito, "The Internet of Things: A survey," *Computer Networks*, vol. 54, no. 15, pp. 2787-2805, 2010.
- [24] J. Hester and J. Sorber, "The Future of Sensing is Batteryless, Intermittent, and Awesome," in *15th ACM Conference on embedded network sensor systems*, Delft, The Netherlands, 2017.
- [25] D. Miorandi, S. Sicari, F. De Pellegrini and I. Chlamtac, "Internet of things: Vision, applications and research challenges," *Ad Hoc Networks*, vol. 10, no. 7, pp. 1497-1516, 2012.
- [26] N. Jackson, J. Adkins and P. Dutta, "Reconsidering Batteries in Energy Harvesting Sensing," in *6th International Workshop on energy harvesting & energy-neutral sensing systems*, Shenzhen, China, 2018.



- [27] M. E. Kiziroglou and E. M. Yeatman, "17 - Materials and techniques for energy harvesting," in *Functional Materials for Sustainable Energy Applications*, J. A. Kilner, S. J. Skinner, S. J. Irvine and P. P. Edwards, Eds., Woodhead Publishing, 2012, pp. 541-572.
- [28] A. Kansal, J. Hsu, S. Zahedi and M. B. Srivastava, "Power management in energy harvesting sensor networks," *ACM Transactions on Embedded Computing Systems*, vol. 6, no. 4, p. 32, 2007.
- [29] L. Tran, H. Cha and W. Park, "RF power harvesting: a review on designing methodologies and applications," *Micro and Nano Systems Letters*, vol. 5, no. 1, pp. 1-16, 2017.
- [30] S. H. Kim et al., "Harvesting electrical energy from carbon nanotube yarn twist," *Science*, vol. 357, no. 6353, pp. 773-778, 2017.
- [31] S. Xu, Y. Qin, C. Xu, Y. Wei, R. Yang and Z. Wang, "Self-powered nanowire devices," *Nature Nanotechnology*, vol. 5, no. 5, pp. 366-373, 2010.
- [32] J. Granstrom, J. Feenstra, H. Sodano and K. Farinholt, "Energy harvesting from a backpack instrumented with piezoelectric shoulder straps," *Smart Materials and Structures*, vol. 16, no. 5, pp. 1810-1820, 2007.
- [33] C. He, M. E. Kiziroglou, D. C. Yates and E. M. Yeatman, "MEMS energy harvester for wireless biosensors," in *2010 IEEE 23rd International Conference on Micro Electro Mechanical Systems (MEMS)*, Hong Kong, China, 2010.
- [34] C.-C. Wu et. al., "A pliable and batteryless real-time ECG monitoring system-in-a-patch," in *VLSI Design, Automation and Test (VLSI-DAT)*, Hsinchu, Taiwan, 2015.
- [35] Y. Zhang et al., "A Batteryless 19  $\mu$ W MICS/ISM-Band Energy Harvesting Body Sensor Node SoC for ExG Applications," *IEEE Journal of Solid-State Circuits*, vol. 48, no. 1, pp. 199-213, 2013.
- [36] F. Fan, L. Lin, G. Zhu, W. Wu, R. Zhang and Z. Wang, "Transparent Triboelectric Nanogenerators and Self-Powered Pressure Sensors Based on Micropatterned Plastic Films," *Nano Letters*, vol. 12, no. 6, pp. 3109-3114, 2012.
- [37] G. Zhu, J. Chen, T. Zhang, Q. Jing and Z. Wang, "Radial-arrayed rotary electrification for high performance triboelectric generator," *Nature Communications*, vol. 5, no. 1, 2014.
- [38] ONiO, "ONiO.zero: A miniaturised green power plant," 2021. [Online]. Available: <https://www.onio.com/products/onio-zero.html>.
- [39] everactive, "Overcoming the Battery Obstacle: End-to-End IoT Strategies and the Two-Pronged Solution," 2021. [Online]. Available: <https://everactive.com/whitepapers/overcoming-the-battery-obstacle-part-iii/>.
- [40] A. Lazaro, R. Villarino and D. Girbau, "A Survey of NFC Sensors Based on Energy Harvesting for IoT Applications," *Sensors*, vol. 18, no. 11, p. 3746, 2018.

- [41] M. Boada, A. Lazaro, R. Villarino and D. Girbau, "Battery-Less Soil Moisture Measurement System Based on a NFC Device With Energy Harvesting Capability," *IEEE Sensors Journal*, vol. 18, no. 13, pp. 5541-5549, 2018.
- [42] J. M. Azzarelli, K. A. Mirica, J. B. Ravnsbæk and T. M. Swager, "Wireless gas detection with a smartphone via rf communication," *Proceedings of the National Academy of Sciences*, vol. 111, no. 51, pp. 18162-18166, 2014.
- [43] P. Sen, S. Kantareddy, R. Bhattacharyya, S. Sarma and J. Siegel, "Low-Cost Diaper Wetness Detection Using Hydrogel-Based RFID Tags," *IEEE Sensors Journal*, vol. 20, no. 6, pp. 3293-3302, 2020.
- [44] S. He et al., "Chemical-to-Electricity Carbon: Water Device," *Advanced Materials*, vol. 30, no. 18, p. 1707635, 2018.
- [45] P. Xie, M. Rong and M. Zhang, "Moisture Battery Formed by Direct Contact of Magnesium with Foamed Polyaniline," *Angewandte Chemie*, vol. 128, no. 5, pp. 1837-1841, 2015.
- [46] X. Chen et al., "Scaling Up Nanoscale Water-Driven Energy Conversion into Evaporation-Driven Engines and Generators," *Nature Communications*, vol. 6, no. 1, p. 7346, 2015.
- [47] D. Shen, M. Xiao, G. Zou, L. Liu, W. Duley and Y. Zhou, "Wearable Electronics: Self-Powered Wearable Electronics Based on Moisture Enabled Electricity Generation," *Advanced Materials*, vol. 30, no. 18, 2018.
- [48] H. He et al., "A water-evaporation-induced self-charging hybrid power unit for application in the Internet of Things," *Science Bulletin*, vol. 64, no. 19, pp. 1409-1417, 2019.
- [49] J. Li, K. Liu, T. Ding, P. Yang, J. Duan and J. Zhou, "Surface functional modification boosts the output of an evaporation-driven water flow nanogenerator," *Nano Energy*, vol. 58, pp. 797-802, 2019.
- [50] G. Xue et al., "Water-evaporation-induced electricity with nanostructured carbon materials," *Nature Nanotechnology*, vol. 12, no. 4, pp. 317-321, 2017.
- [51] X. Zhou et al., "Harvesting Electricity from Water Evaporation through Microchannels of Natural Wood," *ACS Applied Materials & Interfaces*, vol. 12, no. 9, pp. 11232-11239, 2020.
- [52] Y. Qin et al., "Constant Electricity Generation in Nanostructured Silicon by Evaporation-Driven Water Flow," *Angewandte Chemie*, vol. 132, no. 26, pp. 10706-10712, 2020.
- [53] R. Liu, C. Liu and S. Fan, "Hydrocapacitor for Harvesting and Storing Energy from Water Movement," *ACS Applied Materials & Interfaces*, vol. 10, no. 41, pp. 35273-35280, 2018.

- [54] X. Zhao et al., "A Simple High Power, Fast Response Streaming Potential/Current-Based Electric Nanogenerator Using a Layer of Al<sub>2</sub>O<sub>3</sub> Nanoparticles," *ACS Applied Materials & Interfaces*, vol. 13, no. 23, pp. 27169-27178, 2021.
- [55] W. Guo et al., "Bio-Inspired Two-Dimensional Nanofluidic Generators Based on a Layered Graphene Hydrogel Membrane," *Advanced Materials*, vol. 25, no. 42, pp. 6064-6068, 2013.
- [56] F. Zhao, H. Cheng, Z. Zhang, L. Jiang and L. Qu, "Direct power generation from a graphene oxide film under moisture," *Advanced Materials*, vol. 27, no. 29, pp. 4351-4357, 2015.
- [57] H. Cheng et al., "Moisture-Activated Torsional Graphene-Fiber Motor," *Advanced Materials*, vol. 26, no. 18, pp. 2909-2913, 2014.
- [58] M. Ma, L. Guo, D. Anderson and R. Langer, "Bio-Inspired Polymer Composite Actuator and Generator Driven by Water Gradients," *Science*, vol. 339, no. 6116, pp. 186-189, 2013.
- [59] J. Yin, X. Li, J. Yu, Z. Zhang, J. Zhou and W. Guo, "Generating electricity by moving a droplet of ionic liquid along graphene," *Nature Nanotechnology*, vol. 9, no. 5, pp. 378-383, 2014.
- [60] Keysight Technologies, "34410A and 34411A Multimeters Data Sheet," 2015. [Online]. Available: <https://www.keysight.com/ca/en/product/34411A/digital-multimeter-6-digit.htm>.
- [61] Keysight Technologies, "B2900A Series Precision Source/Measure Unit Data Sheet," 2020. [Online]. Available: <https://www.keysight.com/ca/en/assets/7018-02794/data-sheets/5990-7009.pdf>.
- [62] Keysight Technologies, "BenchVue Installation Wizard Software Details," 2021. [Online]. Available: <https://www.keysight.com/ca/en/lib/software-detail/computer-software/benchvue-installation-wizard-2417463.html>.
- [63] LulzBot, "LulzBot TAZ 6 Desktop 3D Printer Specifications," 2016. [Online]. Available: [https://www.lulzbot.com/sites/default/files/TAZ6\\_SpecSheet\\_FINAL.pdf](https://www.lulzbot.com/sites/default/files/TAZ6_SpecSheet_FINAL.pdf).
- [64] colorFabb, "nGen Technical datasheet," 2020. [Online]. Available: [https://colorfabb.com/media/datasheets/tds/colorfabb/TDS\\_E\\_ColorFabb\\_nGen.pdf](https://colorfabb.com/media/datasheets/tds/colorfabb/TDS_E_ColorFabb_nGen.pdf).
- [65] G. Allanwood, "The hot-end of a Mendel90 RepRap 3D printer in action," <https://unsplash.com/photos/Q1NS-nISNIw>. [Online]. Available: <https://unsplash.com/photos/Q1NS-nISNIw>.
- [66] Switchcraft, "Jacks and Plugs Mounting Hardware Drawings," 2021. [Online]. Available: [https://www.switchcraft.com/Drawings/Jack\\_Mounting\\_Hardware.pdf](https://www.switchcraft.com/Drawings/Jack_Mounting_Hardware.pdf).

- [67] T. Gillespie, "The capillary rise of a liquid in a vertical strip of filter paper," *Journal of Colloid Science*, vol. 14, no. 2, pp. 123-130, 1959.
- [68] M. Burkhart, "5 Steps to The Carton Drop Test," Intouch Quality, 2018. [Online]. Available: <https://www.intouch-quality.com/blog/5-steps-to-the-carton-drop-test>.
- [69] Q. Liu, Z. Pan, E. Wang, L. An and G. Sun, "Aqueous metal-air batteries: Fundamentals and applications," *Energy Storage Materials*, vol. 27, pp. 478-505, 2020.
- [70] Cricut, "Cricut Explore Air™ 2," 2021. [Online]. Available: [https://cricut.com/en\\_us/machines/cricut-explore-machines/cricut-explore-air-2/cricut-explore-air-2-mint-1.html#product\\_detail](https://cricut.com/en_us/machines/cricut-explore-machines/cricut-explore-air-2/cricut-explore-air-2-mint-1.html#product_detail).
- [71] Nordic Semiconductor, "Online Power Profiler for Bluetooth LE," 2021. [Online]. Available: <https://devzone.nordicsemi.com/power/w/opp/2/online-power-profiler-for-bluetooth-le>.
- [72] W. Gordon et al., "Remote Patient Monitoring Program for Hospital Discharged COVID-19 Patients," *Applied Clinical Informatics*, vol. 11, no. 05, pp. 792-801, 2020.
- [73] Instron, "Microelectronics Testing Solutions: Ultra High Precision Testing Systems," 2006. [Online]. Available: <https://www.instron.com/-/media/literature-library/applications/2006/03/microelectronics-testing-solutions.pdf>.
- [74] Nordic Semiconductor, "nRF52832 Product Specification v1.8," 2021. [Online]. Available: [https://infocenter.nordicsemi.com/pdf/nRF52832\\_PS\\_v1.8.pdf](https://infocenter.nordicsemi.com/pdf/nRF52832_PS_v1.8.pdf).
- [75] Unified Abrasives Manufacturers' Association, "Abrasives 101," 2018. [Online]. Available: <https://uama.org/abrasives-101/>.
- [76] J. Feng, Y. Zhou, G. Shaker, W. Duley and N. Johnston, "MOISTURE, GAS AND FLUID-ENABLED SENSORS". Canada Patent PCT/CA2020/051527, 12 November 2020.
- [77] A. Sadeghioon, N. Metje, D. Chapman and C. Anthony, "SmartPipes: Smart Wireless Sensor Networks for Leak Detection in water pipelines," *Journal of Sensor and Actuator Networks*, vol. 3, no. 1, pp. 64-78, 2014.
- [78] M. Casillas and L. Garza-Castañón V. Puig, "Optimal Sensor Placement for Leak Location in Water Distribution Networks using Evolutionary Algorithms," *Water*, vol. 7, no. 11, pp. 6496-6515, 2015.
- [79] N. Saeed and A. Urbonavicius, "IoT Leak Detection System for Building Hydronic Pipes," *International Journal of Engineering and Manufacturing*, vol. 9, no. 5, pp. 1-21, 2019.
- [80] World-Health-Organization, UNICEF, "Global Water Supply and Sanitation Assessment 2000 Report: Accounting for Water Loss," World Health Organization, New York, 2000.

- [81] B. Bakhtawar and T. Zayed, "Review of Water Leak Detection and Localization Methods through Hydrophone Technology," *Journal of Pipeline Systems Engineering and Practice*, vol. 12, no. 4, p. 03121002, 2021.
- [82] D. Christin, A. Reinhardt, P. S. Mogre and R. Steinmetz, "Wireless Sensor Networks and the Internet of Things : Selected Challenges," in *8th GI/ITG KuVS Fachgespräch Drahtlose Sensornetze*, Hamburg, Germany, 2009.
- [83] S. Ghosh, A. Sood and N. Kumar, "Carbon Nanotube Flow Sensors," *ChemInform*, vol. 34, no. 21, pp. 1042-1044, 2003.
- [84] S. Ahopelto and R. Vahala, "Cost–Benefit Analysis of Leakage Reduction Methods in Water Supply Networks," *Water*, vol. 12, no. 1, p. 195, 2020.

# Appendices

## Appendix A. Sensor Material Preparation

### A.1. Carbon Electrode

#### A.1.1. CNF and Graphite Electrode Pressing Mould

The carbon pieces used in the sensors are fabricated by pressing CNFs or graphite powder in a mould tool, as shown in Figure 50, to produce a round disc to be used as an electrode. This tool alone can only control the diameter of the carbon electrode reliably. The density and thickness of the electrode as well as levelness of the top face relative to the bottom are difficult to control if the press is hand-actuated, so a pressing machine can be used to actuate the mould. The mass of a single carbon electrode affects the thickness, so the quantity of CNF or graphite loaded into the mould before pressing is controlled with a scale. For CNF electrodes, 50 mg was used per sample, to produce electrodes with diameter of 16.7 mm and thickness of around 1.5 mm. For the graphite electrodes, the mass is kept in the range of 300-310 mg when producing electrodes with diameter of 16.7 mm and thickness of 2 mm. The appropriate masses of CNF or graphite powder to use in the mould when making electrodes were determined in prior studies by colleagues [4].

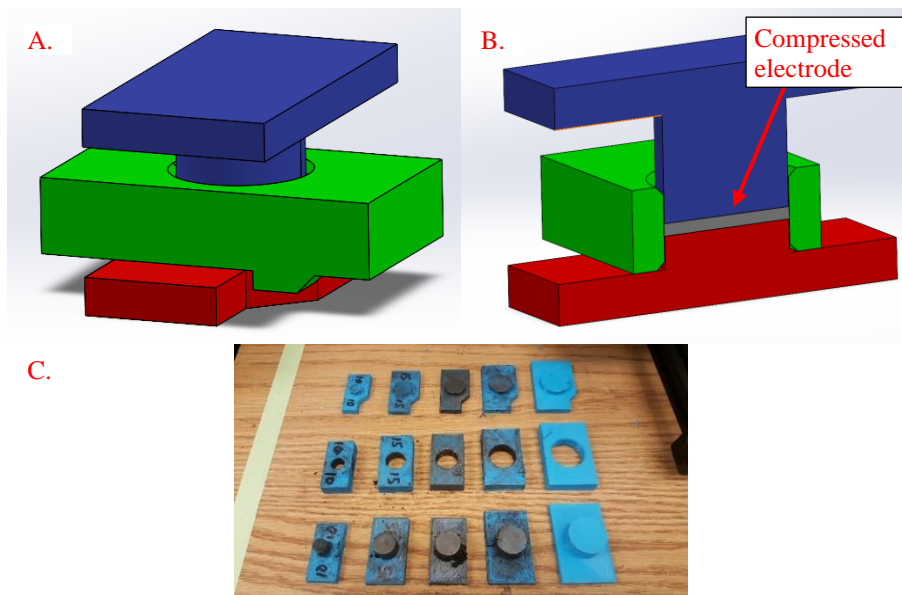


**Figure 50: A) Mould CAD model. B) cross section showing compressed carbon electrode, C) moulds to produce electrodes with different diameters.**

### A.1.2. Mirco Tester as Compression Machine

The pressing mould can be used by hand, and this was done for the initial sensor prototypes using the CNF electrodes. However, to control the variation between electrodes, a more controlled approach to compression was used. By using the Micro Tester 5548 by Instron [73] shown in Figure 51, the compression rate and maximum force are controlled. Pressing moulds from the previous section were be modified to produce 3 electrodes in parallel.

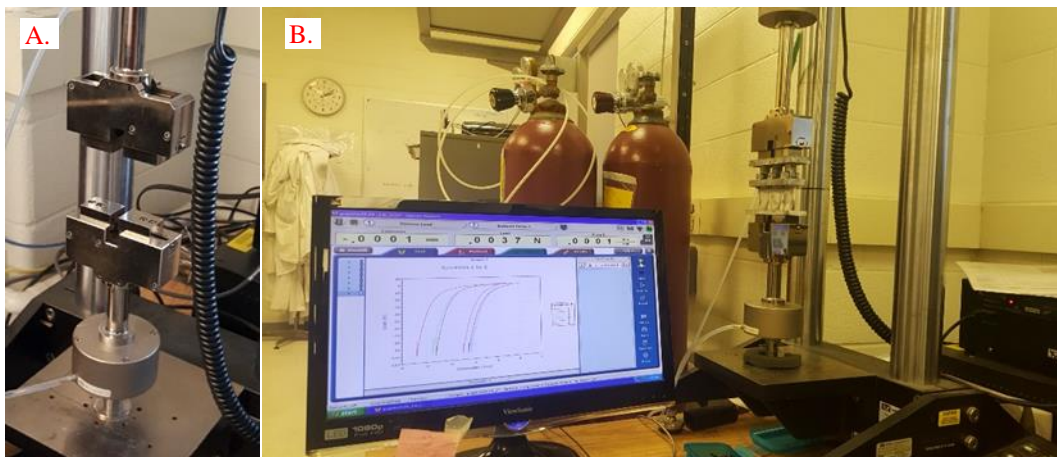


Figure 51: A) Instron Micro Tester 5548 sample holding grips, B) desktop controls with pressing mould in background, 3 samples in parallel

The compression rate controls how quickly the powder is pressed into a disc. The maximum force affects the final density and thickness of the disc and is used as the stop condition for the press. It was found that pressing slowly gives a more uniform density, and limiting the pressing force is a reliable way to control thickness. The selected parameters (from previous work by colleagues [4]) are 10 mm/min pressing rate and a maximum compression force of 100 N when using the pressing mould for 3 electrodes in parallel, with 300-310 mg of graphite powder per mould cavity. These pressing conditions are used for all the graphite electrodes fabricated.

## A.2. Magnesium Electrode

The magnesium electrode is fabricated from magnesium alloy AZ31B. Starting with sheet stock, the magnesium is cut and punched to various sizes before sanding, as described in the following sections.

### A.2.1. Magnesium Plate Preparation

When testing the sensor materials with no packaging, larger rectangular magnesium pieces are used, as seen in Figure 52. These can easily be held in place with a clamp, weight, or magnet. The

long dimension of the plate is such that there is sufficient room for alligator clip attachment, making electrical connection to the samples easy. The surface area is more than sufficient to place a carbon electrode on top. A sheet with 1.6 mm thickness is sheared into 100 mm by 25 mm plates. The plates are wet sanded in two stages, first with 240 grit sandpaper, followed by 400 grit sandpaper.

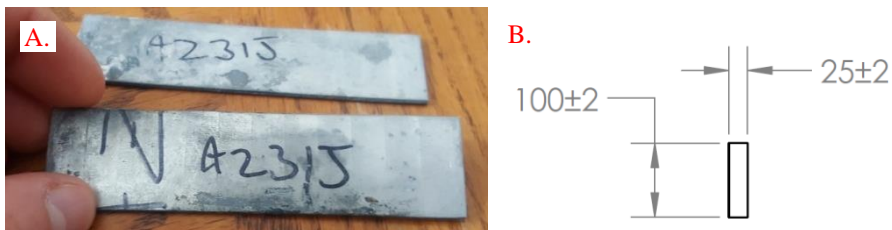


**Figure 52: A) Magnesium plate, not sanded B) drawing with dimensions in millimetres. Thickness is 1.6 mm.**

### **A.2.2. Magnesium Disc Preparation**

The rectangular magnesium pieces are significantly larger than the carbon electrode. To reduce the size of the water leak device as much as possible, magnesium discs are fabricated instead, which are only slightly larger than the carbon electrodes. The magnesium discs were fabricated as blanks using a punch and die set with a diameter of 18.65 mm (46/64") for the die, and 18.26 mm (47/64") for the punch. The clearance between the punch and die was sufficiently small, and the punch head was flattened so that flat discs were produced without additional flattening steps required. The discs are then wet sanded like the plates, first with CAMI 240 grit sandpaper, followed by CAMI 400 grit sandpaper. Since the discs were so thin, they were very difficult to hold for sanding. A 3D printed tool was created with handles on top and a mounting location for the discs on the bottom. Images from the process are presented in Figure 53.



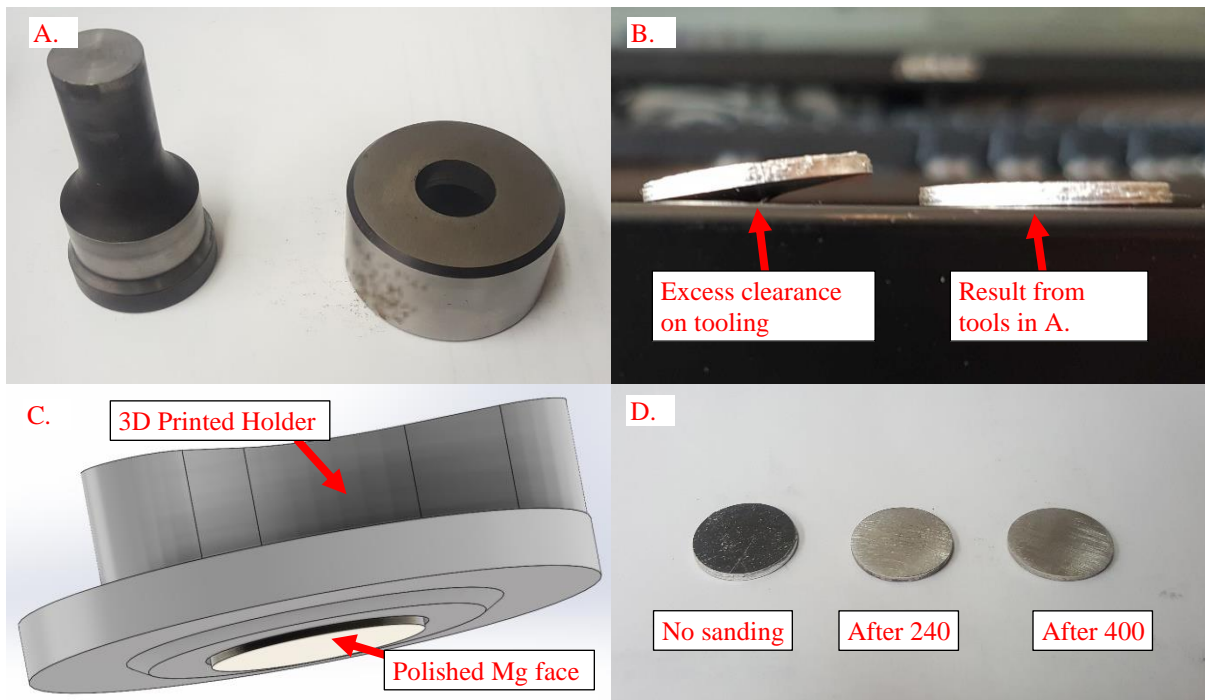


Figure 53: Magnesium disc preparation. A) Punch and die set, B) Mg discs punching, trial and error, C) 3D printed part, holds Mg disc for sanding, D) sanding process, before and after

### A.2.3. Sensor Assembly and Usage

With the carbon and magnesium electrodes fabricated, the sensor device is assembled by placing the carbon electrode in contact with the magnesium electrode. Typically, the carbon electrode is placed directly on top of the magnesium electrode when testing just the materials, however this is reversed in the packaging design, for reasons explained later. After assembly, the device will produce usable power upon the application of water.

## Appendix B. Electrical Details

The sections in Appendix B give additional information on the electronics portion of the water leak detector. The PCBs were designed, tested, and implemented by fellow students; however, a brief explanation of their functionality is provided here to justify the selected test conditions for the sensor in the body of the thesis.

### B.1. System Overview

The two components of the mechanical packaging are the sensor packaging and electronics packaging, or sensor enclosure and electronics enclosure. Inside the sensor portion are the sensor materials, carbon, and magnesium, along with wiring and metal contacts. The electronics are divided into two separate PCB designs, although the same functionality could be accomplished on a single board. The first PCB is the Energy Harvesting (EH) board, and the second is the Bluetooth Low Energy (BLE) board. The connection between each component is shown in Figure 54.

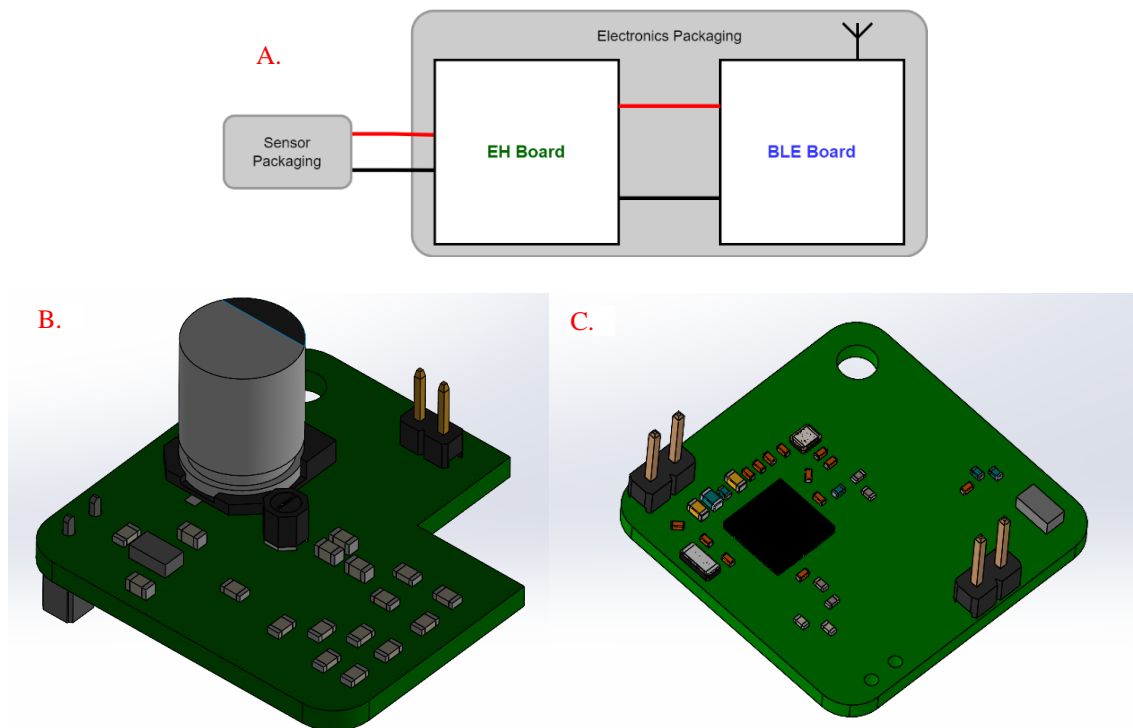


**Figure 54:** Overview of electrical system components. A) Block diagram schematic, B, C) CAD model of the two PCBs: B) EH and C), BLE, each with a 27 mm square footprint.

These three distinct portions of the electrical system are described by their roles, listed below:

1. **Sensor Materials:** Power source for the water leak detector
2. **EH Board:** Interface between sensor and BLE board. Stores the sensor's energy output, and regulates the consumption of this energy by the BLE board.
3. **BLE Board:** Transmits information wirelessly when a water leak occurs

Each of the components are described in more details in the following subsections.

## B.2. Sensor Materials: Basic Electrical Model

A very simple model of the sensor is an ideal voltage source with a series resistance. The model is shown in Figure 55.

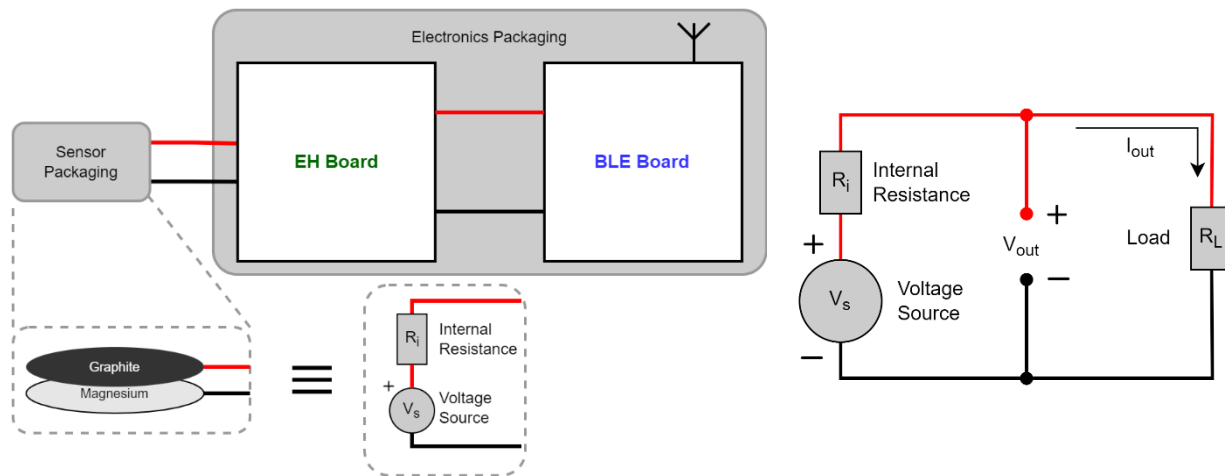


**Figure 55: A) Sensor equivalent electrical model with voltage source and series resistance, B) simplified electrical model of sensor supplying power to a pure resistance load**

If using this model, the voltage supplied by the ideal source,  $V_s$ , and internal resistance,  $R_i$ , are not constant, but rather a function of other factors, for example, the quantity of water applied, temperature and humidity, time elapsed since water application, and the carbon and magnesium electrode properties. Nevertheless, we can assume the values are constant to explain the OCV, SCC, and load tests. The internal resistance  $R_i$  and load resistance  $R_L$  are in series, forming a voltage divider configuration. The output voltage  $V_{out}$  of the sensor can be calculated with eq. 1.

$$V_{out} = \frac{R_L}{(R_i + R_L)} V_s \quad (1)$$

In the OCV test,  $R_i \ll R_L$ , and so  $V_{out} \approx V_s$ . This means the OCV is the same as  $V_s$ , or  $V_{OC} = V_s$ . Using Ohm's law in eq. 2 at the load resistance, and substituting into eq. 1, we can express the output current  $I_{out}$  in terms of  $V_{OC}$  in eq. 3.

$$V_{out} = I_{out}R_L \quad (2)$$

$$I_{out} = \frac{1}{(R_i + R_L)} V_{OC} \quad (3)$$

In the SCC test,  $R_i \gg R_L$ , so, from eq. 3,  $I_{SC} \approx (1/R_i)V_{OC}$ . Hence, the internal resistance of the sensor is a function of the OCV and SCC, which is given in eq. 4.

$$R_i = \frac{V_{OC}}{I_{SC}} \quad (4)$$

The output voltage and current,  $V_{out}$  and  $I_{out}$  are not independent. Using Ohm's law to eliminate the internal resistance voltage drop, we can obtain  $V_{out}$  as a function of  $I_{out}$ , in eq. 5.

$$V_{out} = V_s - I_{out}R_i \quad (5)$$

But, as we previously saw,  $V_s = V_{OC}$ , and  $R_i = V_{OC}/I_{SC}$ , and substitution gives eqs. 6 and 7.

$$I_{out} = I_{SC} - \frac{I_{SC}}{V_{OC}} V_{out} \quad (6)$$

$$V_{out} = V_{OC} - \frac{V_{OC}}{I_{SC}} I_{out} \quad (7)$$

Assuming  $R_i$  is constant, we can predict output power  $P_{out}$ . To obtain  $P_{out} = f(V_{out})$ , multiply the right hand side of eq. 6 by  $V_{out}$ , and for  $P_{out} = f(I_{out})$ , the right hand side of eq. 6 by  $I_{out}$ .

$$P_{out}(I_{out}) = V_{OC}(I_{out}) - \frac{V_{OC}}{I_{SC}} (I_{out})^2 \quad (8)$$

$$P_{out}(V_{out}) = I_{SC}(V_{out}) - \frac{I_{SC}}{V_{OC}} (V_{out})^2 \quad (9)$$

Equations 8 and 9 are quadratic, meaning that the sensor has a theoretical maximum power output at  $\{V_{out}, I_{out}, P_{out}\} = \{(1/2)V_{OC}, (1/2)I_{SC}, (1/4)V_{OC}I_{SC}\}$ , which matches Jacobi's Maximum Power Transfer Theorem for the voltage source with internal resistance model. For the sake of demonstration, we can choose values for a theoretical carbon-magnesium sensor device, say  $V_{OC} = 2$  V, and that  $I_{SC} = 5$  mA. From eq. 4, the internal resistance would be 400  $\Omega$ . Then, using

eqs. 7, 8, and 9, the output voltage and power can be written as eqs. 10 to 12, with  $V_{out}$ ,  $I_{out}$ , and  $P_{out}$  in units of V, mA, and mW respectively.

$$V_{out} = 2 - \frac{2}{5}I_{out} \quad (10)$$

$$P_{out} = f(I_{out}) = 2(I_{out}) - \frac{2}{5}(I_{out})^2 \quad (11)$$

$$P_{out} = f(V_{out}) = 5(V_{out}) - \frac{5}{2}(V_{out})^2 \quad (12)$$

These relationships are plotted in Figure 56. There are two main states in which the water leak device will operate. First, when water activates the device, a storage capacitor must be charged. The energy harvesting electronics charge the capacitor with an input voltage around 400 mV and consume whatever power the sensor supplies at this voltage. Second, after the capacitor is charged, the BLE device enters an ON state and the BLE device begins transmitting (BLE TX). The average power consumption at the second operating point is in the range of (40 to 100)  $\mu$ A. These two operating points (capacitor charge and BLE TX) are shown as well in Figure 56.

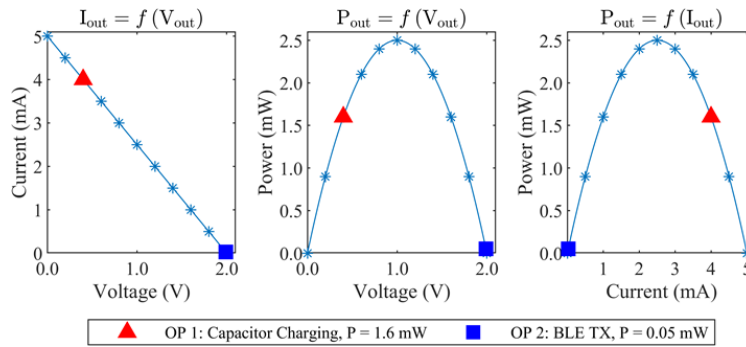


**Figure 56: Relationship between  $V_{out}$ ,  $P_{out}$  and  $I_{out}$  for the sensor component, assuming constant  $R_i = 400 \Omega$ . The approximate operating points when used in the water leak detector are shown. Maximum theoretical power output is 2.5 mW.**

These operating points are selected for the load test configurations to measure the sensor performance in the two main states of water leak detection operation. The two conditions used for the load test are a constant current test at 50  $\mu$ A and a constant voltage test at 400 mV. Note that the maximum sensor output power is not one of the operating states. This would require a design change to the EH and BLE devices and is not a focus of the thesis.

### B.3. EH Board

The energy harvesting board can be further broken down into 3 major components: a DC/DC boost converter, an electrolytic bulk storage capacitor, and a LDO regulator, seen in Figure 57.

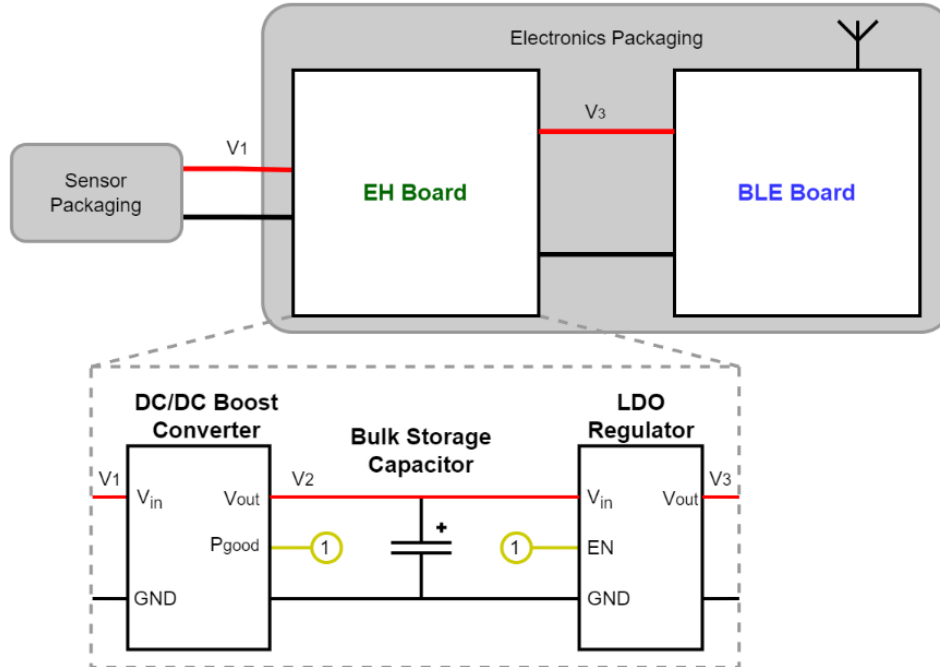


Figure 57: EH board block diagram

The boost converter raises the input voltage  $V_1$  up to a maximum of 3.6 V, which rises as the capacitor is charged. When the capacitor voltage is greater than 2.2 V, the output signal  $P_{good}$  will be set to a digital high, which in turn enables the LDO regulator via its enable (EN) pin. The LDO regulates the capacitor voltage down to a stable 1.8 V, dissipating excess energy to keep the output  $V_3$  stable, as the BLE board requires a steady input voltage to operate properly.

### B.4. BLE Board

The BLE board can be summarized by the BLE chipset selected for the application. The nRF52832 by Nordic Semiconductor, as described on the product webpage, is a “Versatile Bluetooth 5.2 SoC supporting Bluetooth Low Energy, Bluetooth mesh and NFC” [74]. The device can operate on an input voltage of (1.7 to 3.6) V, as per the manufacturer’s recommendation [74]. The wireless radio consumes current in very short (3 to 4) ms bursts when BLE transmissions are done, in the range of (5 to 10) mA. Since the BLE transmissions are relatively short with a configured frequency of 1 transmission per second, the average current consumption is quite low, around (20 to 30)  $\mu$ A [71]. For an input voltage of 1.8 V, this gives a power consumption of (36 to 54)  $\mu$ W, which is far

lower than the sensor's capabilities. However, it is advisable to have the sensor output a much higher power than required for a couple reasons: (1) the EH board is not 100% efficient, so some power is lost, (2) more power gives a faster time to the first BLE transmission since the capacitor must charge, and (3) the device is more tolerant to variations in sensor performance.

## **Appendix C. Injection Moulding Design Changes**

### **C.1. Overview of Design Guidelines and Requirements**

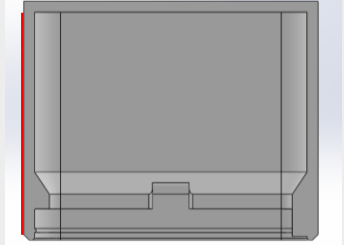
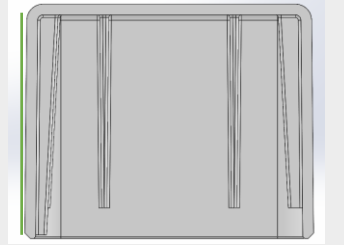
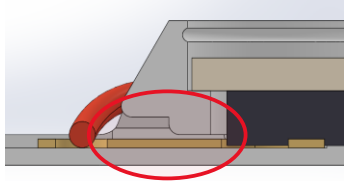
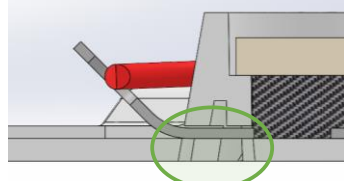
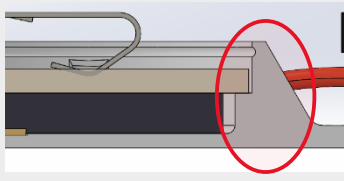
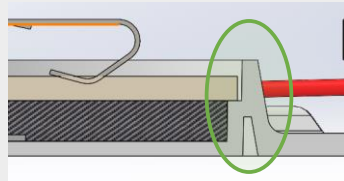
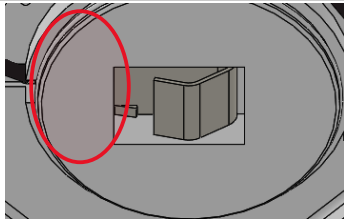
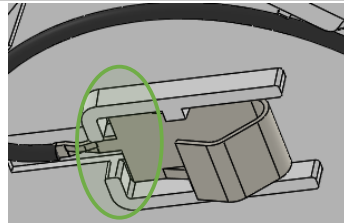
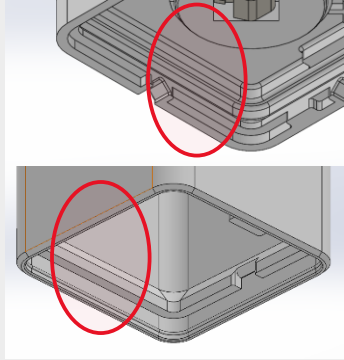
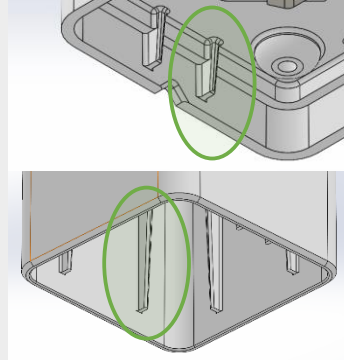
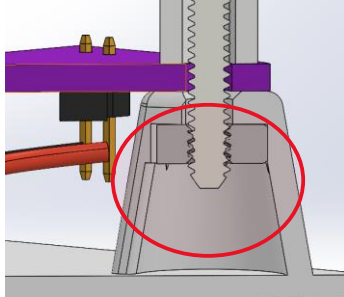
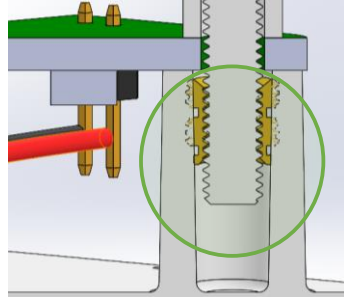
The list of design requirements for injection molding is readily available and industry standard knowledge. Some of the main considerations are using uniform wall thicknesses throughout the design, meaning abnormally thick sections should be avoided. Rounded, uniform thickness corners are preferred over sharp corners. Most importantly, the process involves pulling the metal tooling away from the plastic piece, and so all faces are drafted to some degree to facilitate the release process. Furthermore, overhangs and holes perpendicular to the pull direction require more complex tooling and should be avoided if possible. A brief overview of these changes from the 3D printed version are given in the following section.

### **C.2. List of Injection Molding Changes**

The list of changes from the 3D printed version are given in Table 18. Other design changes that are not specifically for injection moulding are not included in this table.



**Table 18: List of changes for injection moulding manufacturability**

Part	Description of Change	3D Printed Design	Injection Moulded Design
<b>All parts</b>	Draft added on all walls parallel to the pull direction, minimum 0.5 deg of draft was used. Difficult to see in images, so a reference line (vertical) is provided. The moulded part is slightly narrower at the top.		
<b>Sensor Enclosure Bottom</b>	The graphite contact mounting location had a long, undercut section. The base was opened to allow access for the lower mould tool.		
<b>Sensor Enclosure Bottom</b>	The graphite and Mg chamber wall thickness was highly variable versus height and therefore prone to sinking. It was hollowed out to avoid issues.		
<b>Sensor Enclosure Top</b>	The Mg spring contact holder used an undercut and a thick section boss. This was reduced to a smaller set of thin walls.		
<b>Sensor Enclosure Top and Electronics Enclosure Top</b>	A large lip/flange was used as a stopper for the mating piece but was overhanging. This was replaced with thin rib features, which also add strength to the part.		
<b>Electronics Enclosure Bottom</b>	Previously, an overhanging cut-out supported a hex nut for screwing into the part. This overhand was replaced with a boss feature into which a threaded insert was mounted.		

## Appendix D. Wireless Leak Detection System Architecture

The wireless systems and cloud component used to support the water leak detector are described in this section. These parts of the system were a collaborative effort between fellow students. The overall system is briefly described for reference here.

### D.1. Overview of System Architecture

An overview of the system architecture is given in Figure 58. The water leak sensor uses the Nordic Semiconductor nRF52832 BLE chipset, which, when powered by the Energy Harvesting Board, produces a BLE advertisement packet, which includes that water leak sensor's specific ID. This is marked as a Bluetooth signal in the diagram below. The local gateway device actively scans for Bluetooth data and receives any of these advertisement packets sent by water leak sensors. The gateway device can then send this information to a cloud platform by using a cellular data connection, which requires an active on-board SIM card. The cloud implementation is done with Azure, which stores the data, as well as generates alerts for the user via email and SMS connections. It also can cross-reference the sensor's ID with a database of known sensor locations, so that a specific sensor location is provided to the user in an alert.

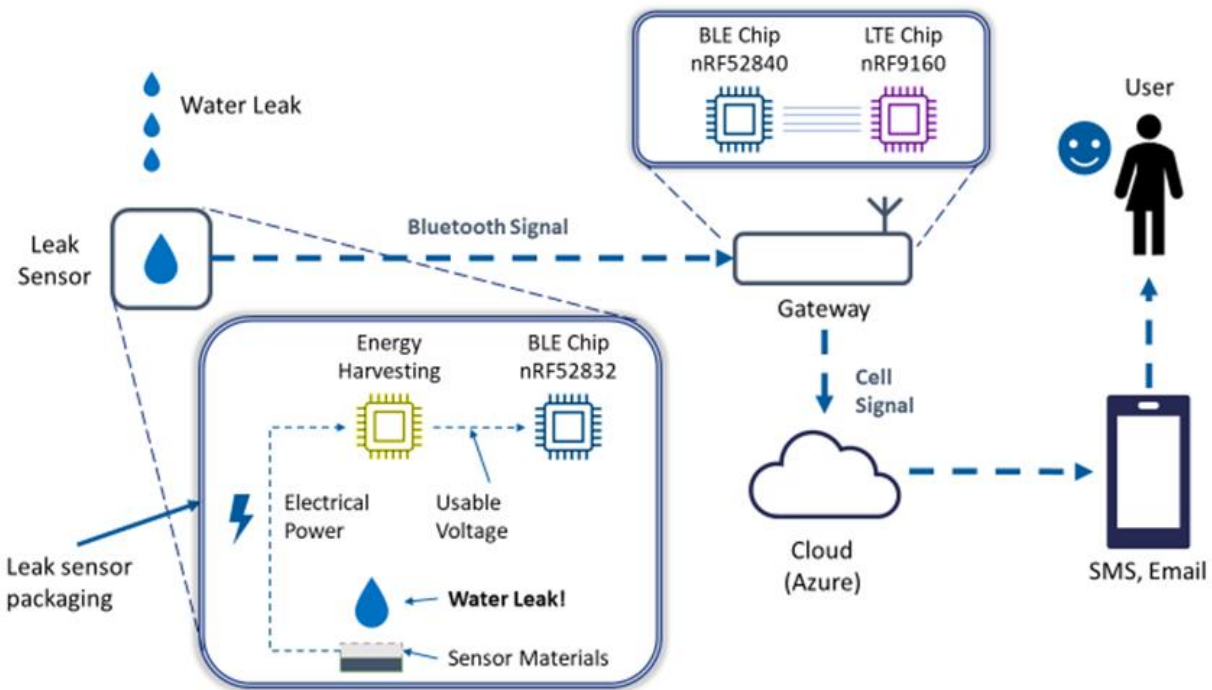


Figure 58: System architecture, showing data transmission starting at the water leak sensor, on to a gateway device, to the cloud, and then to a user.